Influence of Sn Promoter on Pd and Pt Catalysts for the Conversion of Heptanoic Acid and Propane

A Dissertation

Presented to

the faculty of the School of Engineering and Applied Science

University of Virginia

In Partial Fulfillment

of the requirement for the Degree

Doctor of Philosophy in Chemical Engineering

By

Nicholas Kaylor

July 2018

Abstract

Silica-supported Pd catalysts can be used to selectively remove oxygen from biomass-derived carboxylic acids through decarbonylation. This work aims to improve Pd catalyst stability and selectivity towards desirable products by varying metal particle size as well as by introducing Sn to the catalyst. Catalysts were prepared by ion exchange or incipient wetness impregnation of metal precursors on Davisil 636 silica gel supports, followed by calcination in air and reduction in dihydrogen. Monometallic Pd and Sn catalysts, in addition to chemically-mixed and physically-mixed PdSn catalysts, were tested for activity in heptanoic acid conversion. Two-stage reactor beds were used to probe the effect of Sn proximity on Pd. X-Ray diffraction, hydrogen chemisorption, transmission electron microscopy, and X-ray absorption near edge structure-temperature-programmed reduction were used to characterize the catalysts.

The stability of the monometallic Pd catalyst during decarbonylation of heptanoic acid was influenced by the metal particle size, with smaller particles deactivating slower than larger particles. Whereas catalyst deactivation was reduced by adding Sn to Pd by impregnation, improved stability was also observed when Sn/SiO_2 was physically mixed with Pd/SiO_2. The physically mixed PdSn initially produced products characteristic of monometallic Pd, however, the two bimetallic catalysts showed similar product selectivities after 10 h on stream. The PdSn catalysts also expanded the reaction network to include hydrogenation and decarboxylative ketonization, with the primary product shifting from hexene to heptanal. Scanning transmission electron microscopy-energy dispersive spectroscopy of physically-mixed PdSn catalyst indicated that Sn migrated to the silica support particles containing Pd. In situ XANES analysis during butyric acid deoxygenation indicated that SnO_x is the primary Sn phase associated with Pd in both the physically-mixed and chemically-mixed catalysts.

The promotional effect of Sn on Pt catalysts for propane dehydrogenation was also explored. The high temperatures and reducing conditions of the alkane dehydrogenation reaction are substantially different from the carboxylic acid reactions and likely result in a more reduced state of the Sn promoter. Bimetallic PtSn catalysts showed improved stability compared to monometallic Pt catalysts, which deactivated rapidly with time on stream. X-ray diffraction indicated the presence of Pt_xSn_y alloys in the bimetallic catalysts, suggesting that alloy phases play a critical role in improving catalyst stability. The PtSn particles could be regenerated by an oxidative treatment when supported on alumina but not on silica. Both Sn and trace amounts of carbon on Pt decreased propane hydrogenolysis activity in the presence of co-fed dihydrogen.

Acknowledgements

First and foremost, I'd like to thank my advisor, Dr. Robert J. Davis. Under his guidance, I have vastly expanded my knowledge of the physical sciences, and I have refined my ability to communicate scientific data (or so I hope!). His generosity has allowed me to travel the world to places like South Korea and the Netherlands, all to advance my knowledge of heterogeneous catalysis. I would also like to thank my thesis committee members Dr. William Epling, Dr. Geoffrey Geise, Dr. Matthew Lazzara, and Dr. Sen Zhang for guiding me through the completion of my PhD. Financial support was provided by the National Science Foundation under award number EEC-0813570. The XANES studies were supported by the Korea Institute of Energy Technology Evaluation and Planning (KETEP-20154030200830).

I'd like to acknowledge and thank Richard White, Dr. Helge Heinrich, and Cathy Dukes for their training on analytical equipment and their guidance in data analysis. The chemical engineer department staff including Jennifer Davis, Teresa Morris, Vickie Falconer, Jennifer Lamb, Ryan Thompson, and Rich Buchanan have been invaluable throughout my time here at UVA.

Shout out to all of the past and present members of the Davis lab. Thank you, Dr. Juan Lopez-Ruiz, for taking the time to train me during your last few weeks on grounds. I'd like to thank Dr. Derek Falcone and Dr. Zachary Young for their insightful discussions that were invaluable throughout my PhD. Davis lab class of 2018, James Kammert and Dr. Jiahan Xie, you will be missed. I look forward to following your careers. Thank you Dr. Sabra Hanspal, Dr. Benjamin Huang, and Dr. Kehua Yin for your support and guidance. Best of luck to the future graduates of the Davis lab: Gordon Brezicki, Tyler Prillaman, Naomi Miyake, and Lu Yang. Continue to cultivate the welcoming environment that has attracted so many great minds to our research group.

I could not have completed this degree without the love and support of my family. Thank you for providing me an outlet to vent and encouragement to continue moving forward into the unknown. Mary Elizabeth Shank, thank you for having my back through the good times and the bad.

Table of contents

List of figures

List of tables

List of schemes

1. Introduction

1.1. New carbon feedstocks

The chemical industry has long relied on fossil carbon feedstock sources. A renewed focus on climate change and recent trends in oil prices have made alternative feedstocks, such as biomass[1–3] and natural gas[4–6], attractive source of carbons for fuels and fine chemicals. Biomass offers a renewable carbon source with the potential to limit the environmental impact of chemical production.[2,7] Several methods are being explored to convert biomass to chemicals, many of which rely on different feedstock sources that will influence the production route.[8] The cost and viability of petrochemical-scale production of biomass-derived chemicals can vary significantly depending on the maturity of the technology. Thus, fundamental research is critical to continue laying the groundwork to allow for biomass-derived feedstocks to gain a significant market share in the chemical industry.

One such organization working on fundamental research in the area of biomass valorization is the Center for Biorenewable Chemicals (CBiRC), a US National Science Foundation Engineering Research Center headquartered at Iowa State University. The scientists at CBiRC are divided into three thrusts. Thrust 1 focuses on developing new enzymatic biocatalysts for converting sugars to desired building block molecules. Thrust 2 focuses on designing microbes, such as bacteria and yeast, which can house the new biocatalysts while resisting deterioration due to the produced molecules. Thrust 3 focuses on catalytically upgrading the biomass-derived feedstock molecules to value-added chemicals. Several biomass-derived platform molecules for valorization have been identified and are shown in Figure 1.1. The platform molecules, such as carboxylic acids, furans, and pyrones, contain higher carbon-to-oxygen ratios compared to those found in fossil carbon-derived molecules. Thus, a critical focus of the research in thrust 3, particularly in the carboxylic acid testbed, is the deoxygenation of biomass-derived molecules.[9] Several deoxygenation paths can occur during the conversion of carboxylic acids including decarboxylative ketonization , hydrogenation, decarboxylation, and decarbonylation. The reaction path depends on factors such as the reaction temperature, catalyst, and the presence of H_2.

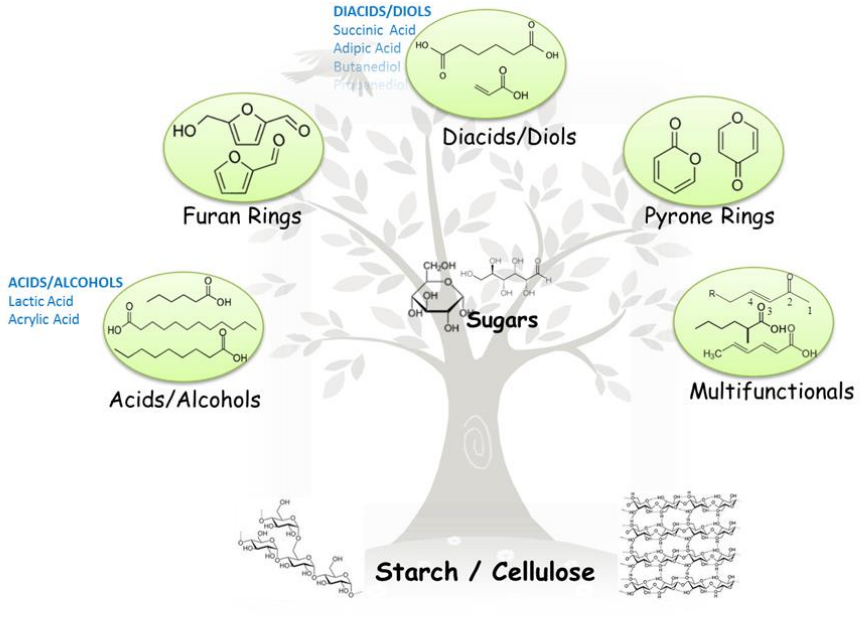

Figure 1.1: Biomass-derived platform molecules identified and targeted by CBiRC. https://www.cbirc.iastate.edu/overview/mission/

A significant portion of the published studies investigating the deoxygenation of biomass-derived carboxylic acids has utilized co-fed dihydrogen that improved catalyst stability but resulted in fully saturated hydrocarbon products.[10–15] These saturated products are acceptable if the goal is the production of biomass-derived diesel-like molecules such as n-heptadecane. However, previous work in CBiRC targeted α-olefin products, which are valuable commodity chemicals, through decarbonylation in the absence of co-fed dihydrogen.[16,17] Several monometallic catalysts included Pt, Pd, and Rh were found to be active for the decarbonylation of carboxylic acids, as well as the decarboxylation or organic acids, but suffered from poor stability and selectivity to higher value α-olefin products.[18] It was found that Pd/SiO_2 was particularly active for the gas-phase deoxygenation of propanoic acid but suffered from rapid deactivation in the absence of co-fed dihydrogen.[18]

In contrast to biomass-derived molecules, natural gas provides immediate drop-in capability as a feedstock source of light hydrocarbons. Light alkenes are key building block molecules in the chemical industry with a variety of applications including the production of plastics and chemical intermediates. Production of light olefins, including ethene, propene, and butenes, traditionally relies on steam cracking and fluid catalytic cracking of naphtha and other light oil products. [4,19] The traditional production route makes it difficult to scale production to meet the growing demand of light olefins such as propene. Figure 1.2 shows the current and forecasted production of natural gas in the US. Recent advances in fracking technologies have led to a substantial increase in the supply of light hydrocarbons, including propane, allowing for chemical companies to more easily scale production of light olefins to meet growing demands through new on-purpose dehydrogenation facilities.

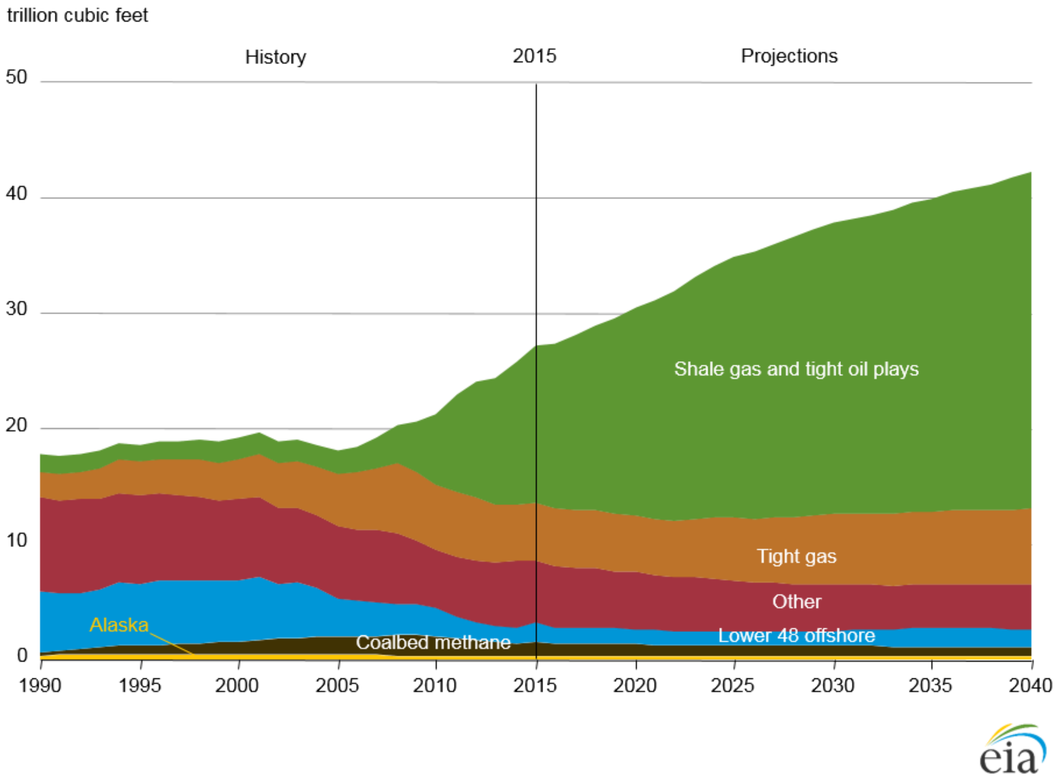

Figure 1.2: US dry natural gas production, in trillion cubic feet, by source courtesy of the EIA, found at https://www.eia.gov/energyexplained/index.cfm?page=natural_gas_where

The cost of crude oil is a rising concern as conventional petroleum sources become scarcer. Historical data suggests that there was a long-run relationship between oil and natural gas in which the price of natural gas tracked that of crude oil.[20–22] US natural gas prices have ceased to track oil costs beginning around 2007 (Figure 3), corresponding with the rapid increase in shale gas exploitation.[22,23] Long term trends suggest that natural gas costs will continue to deviate from crude oil prices as long as shale gas remains a viable light alkane source.[24] Thus, natural gas offers a long term and low cost source of propane and other light alkanes that are capable of meeting future depends for key building block molecules.

Figure 1.3: Crude oil and natural gas prices.[22] Reprinted from Energy Policy, 110, Stephen P.A. Brown, Natural gas vs. oil in U.S. transportation: Will prices confer an advantage to natural gas?, Copyright 2017, with permission from Elsevier.

Indeed, US propane production from natural gas increased from 12.4 billion gallons to 19.6 billion gallons between 2005-2014.[25] Of this increase, 7.7 billion gallons in 2005 and 14.8 billion gallons came from shale gas processing.[25] Propane dehydrogenation (PDH) capacity in the US as of 2016 was approximately 0.6 million tons per year, with an estimated increase of 4.2 million tons per year due to current planned and proposed on-purpose PDH plants.[25] Figure 1.4 shows an overview of the operational and planned on-purpose propane dehydrogenation industrial sites around the world. The two most widely adopted processes are the Catofin process and Oleflex process. The Catofin process utilizes a chromium-based catalyst which creates environmental concerns due to the toxicity of chromium compounds. The Oleflex process, which is the most widely adopted process for on-purpose PDH, utilizes a Sn-promoted Pt/Al_2O_3 catalyst.

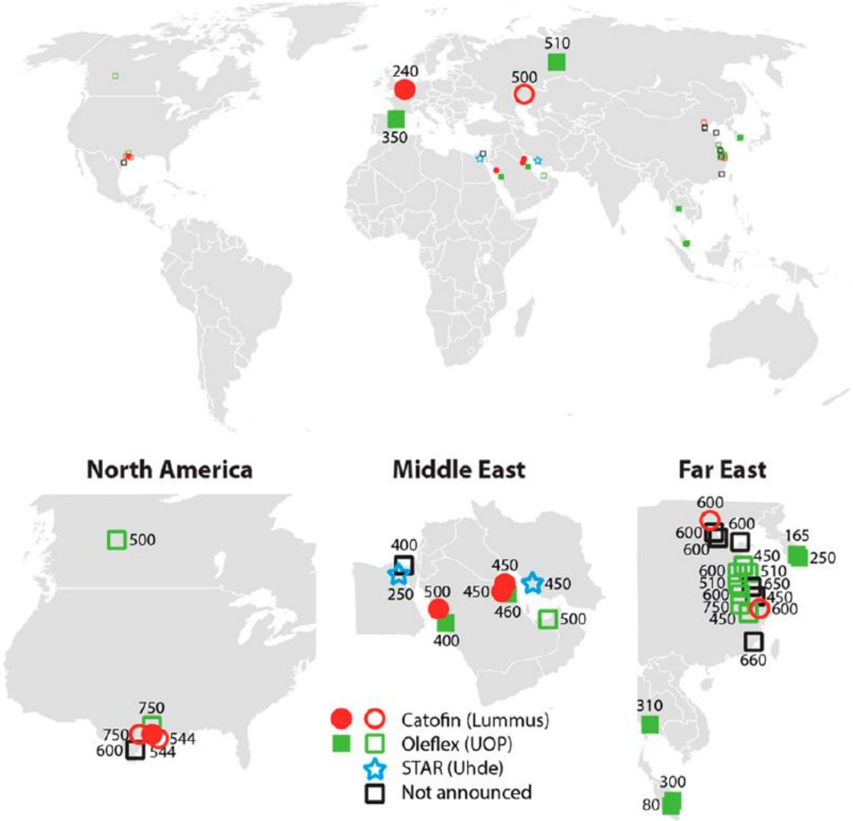

Figure 1.4: World map showing an overview of propane dehydrogenation installations currently in operation (filled shapes) and installations that have been announced and are expected to start up before 2018 (unfilled shapes). The numbers represent the maximum production of each plant (x1000 tons per year). The locations of the facilities are approximations. For some of the newly announced PDH installations, the industrial process to be used remains to be announced. Reprinted with permission from Sattler, J. J. H. B., Ruiz-Martinez, J., Santillan-Jimenez, E. & Weckhuysen, B. M. Catalytic Dehydrogenation of Light Alkanes on Metals and Metal Oxides. *Chem. Rev.* **114,** 10613–10653 (2014). Copyright 2014, American Chemical Society.[4]

1.2. Tin as a promoter

The use of a secondary metal as a promoter in industrial bimetallic catalysts dates back to 1968 when Exxon researchers added Re to a Pt/Al_2O_3 reforming catalyst.[26] The addition of Re promoter improved the Pt catalyst stability and improved the yield of valuable aromatic products. Tin promoter was explored in 1969 because Sn was inert under reforming conditions while Re readily catalyzed hydrogenolysis reactions.[26,27] The Sn promoter reduced the rate of Pt reforming catalyst deactivation by blocking the sites responsible for coke formation, disrupting the Pt ensembles required for hydrogenolysis, and improving the ability to regenerate the active sites.[26–29] Similar benefits of Pt promoted by Sn have been observed during the dehydrogenation of light alkanes. Tin on its own is not particularly active for dehydrogenation reactions. Instead, promotion of Pt with Sn is known to improve selectivity to light alkenes while reducing coke formation through ensemble dilution, in addition to aiding in the oxidative regeneration of Pt catalysts.[4,30–36]

The promotion of Pt group metals with Sn has been explored for a variety of biomass-upgrading reactions.[37–47] The oxophilic Sn species appear to improve the activation of C-O bonds, facilitating the deoxygenation reactions that are critical to producing drop-in biomass-derived fuels.[46,48–50] Indeed, bifunctional catalysts containing an oxophilic metal, such as Sn or Re, and a reduced metal exhibit desirable deoxygenation behavior due to the activation of C-O bonds on the oxides and hydrogen activation on the reduced metal, particularly in the reduction of acids to aldehydes via the reverse Mars and Van Krevelen mechanism (Figure 1.5).[39,51,52] In the reverse Mars and Van Krevelen Mechanism, oxygen vacancies in a partially reduced metal oxide activate the C-O bond of a carboxylic acid which are then cleaved in the presence of hydrogen to form an aldehyde. A metal promoter capable of hydrogen activation is critical for the hydrogenation of the acid and subsequent regeneration of oxygen vacancies.

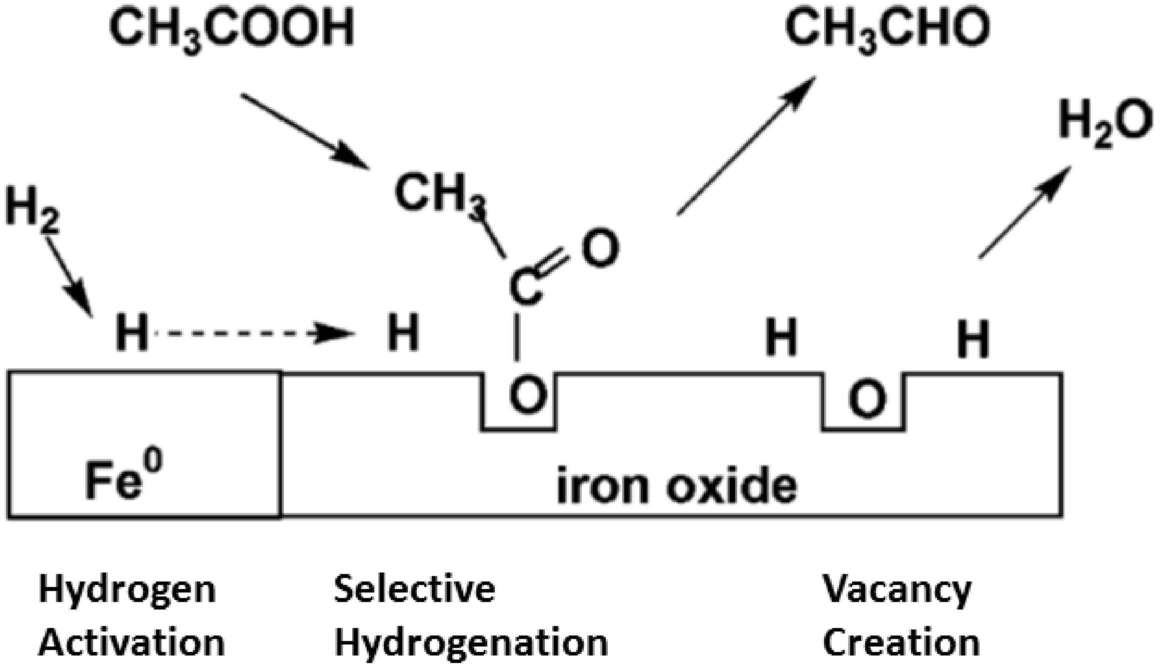

Figure 1.5: Proposed reverse Mars and Van Krevelen mechanism for the hydrogenation of acetic acid over partially reduced iron oxide.[39] Reprinted from Applied Catalysis A: General, 221, T. Yokoyama, N. Yamagata, Hydrogenation of carboxylic acids to the corresponding aldehydes, Copyright 2001, with permission from Elsevier.

1.3. Catalyst Synthesis

The catalyst synthesis method plays an important role in developing the final structure and reactivity of catalysts, particularly when multiple metals are involved. Catalysts can be purchased pre-made, or more frequently prepared in-house through a variety of synthesis techniques. The most basic and widely utilized synthesis technique is the incipient wetness impregnation (IWI) technique. The IWI synthesis method is simply the addition of a metal precursor solutions (i.e. chloroplatinic acid hexahydrate) to a catalyst support where the volume of precursor solution equal to the pore volume of the support material. High surface area porous support materials, such as silica, are preferable for producing well dispersed nanoparticles as they aid in the distribution of the precursor. The solvent for the precursor is typically water, but can also include ethanol, methanol, acetone, and others. Incipient wetness impregnation can used to synthesize monometallic, bimetallic, or even trimetallic catalysts. As the number of metals increases, the order in which they are added can play a significant role in the structure and reactivity of the catalyst. For example, Pt-Sn catalysts were synthesized through a sequential impregnation by the addition of Sn precursor prior to Pt precursor, and through co-impregnation on a silica support.[35] Temperature-programmed reduction and chemisorption indicated that co-impregnation improved the interaction between Pt and Sn resulting in improved catalyst stability for the dehydrogenation of isobutane.

One method used to improve the nanoparticle dispersion is the ion exchange synthesis technique. In this synthesis method, catalyst supports are dispersed in a solution in which the pH has been adjusted to be well above the support material's point of zero charge. Metal complexes are electrostatically adsorbed on the catalyst support resulting in well-dispersed nanoparticles following a mild treatment in H_2. For example, well-dispersed Pd/SiO_2 can be synthesized by adding $PdCl_2$, which has been dissolved in a basic solution, to a slurry of acid-washed silica.[53,54] Under basic conditions, the Pd^{2+} ions can adsorb onto the deprotonated surface hydroxyl groups found on the silica. Acid washing of the silica is critical to ensuring that the density of hydroxyl groups is sufficient for all of the metal to adsorb. Metal clusters synthesized by ion exchange on high surface area supports, such as silica gel, are typically around 1 nm in size and result in nearly all of the metal atoms to be exposed.[53–55]

The ion exchange technique can be used to produce well-dispersed catalysts with bimetallic clusters in the 1 nm range.[54] However, some elements such as Sn can precipitate under the basic conditions required to produce a properly exchanged catalyst on a silica support. In these situations, a colloidal synthesis technique, such as the polyol method, can be employed to control particle size and to ensure intimate contact between the two metals. The polyol synthesis method utilizes a polyol, such as ethylene glycol, as the solvent for dissolving common metal precursor salts (i.e. platinum chloride and tin chloride). The polyol solvents have relatively high boiling points, allowing for the use of elevated temperatures that are required for synthesizing catalysts that do not easily reduce at low temperatures. At these elevated temperatures, the polyols are able to reduce metal precursors into nanoparticles while simultaneously acting as protective capping agents that prevent agglomeration of the metals, thus controlling the size of the nanoparticles.[56] Bimetallic catalysts with controlled compositions, such as Pt_7Sn_3,[57] and controlled size distributions can be obtained through colloidal synthesis technique.[56–58]

1.4. Chemisorption

Chemisorption is the formation of an irreversibly adsorbed monolayer of a reactant molecule on a substrate, such as a catalyst surface.[59] This physical phenomenon is exploited as a method for measuring the available surface sites on a catalyst. Typical probe molecules for measuring the exposed surface sites of metal nanoparticles include dihydrogen and carbon monoxide. The stoichiometry between these probe molecules and the catalyst surface will vary depending on the molecule, the metal on the catalyst, and the nanoparticle size.[60] For example, dihydrogen will dissociatively adsorb on Pd surfaces resulting in a 1:1 H:Pd stoichiometry. In contrast, CO can bridge-bond on Pd surfaces, meaning that more than one Pd atom can interact with one CO molecule.[61]

In a typical chemisorption measurement, the probe gas is dosed in at specific pressures and allowed to come to equilibrium. The amount of gas adsorbed at each pressure is recorded by the analysis equipment.[59] Figure 1.6 displays the characteristic hydrogen chemisorption isotherms for a commercial 5 wt% Pt/Al_2O_3 purchased from Sigma-Aldrich. The “Initial” isotherm shows the total mmol of H_2 adsorbed per gram of catalyst. The reported chemisorption uptake is calculated by extrapolating the linear portion of the isotherm to zero pressure in order to estimate the monolayer coverage. After the “Initial” data collection, the system is pumped down under vacuum, typically for at least one hour, and the analysis is run a second time. The “Repeat” isotherm shows the uptake on weakly adsorbing sites, or the sites which the hydrogen was physisorbed and thus removed when the catalyst sample was subjected to a vacuum. All chemisorption values reported in this dissertation are reported as the total uptake, or the "Initial" collection of data.

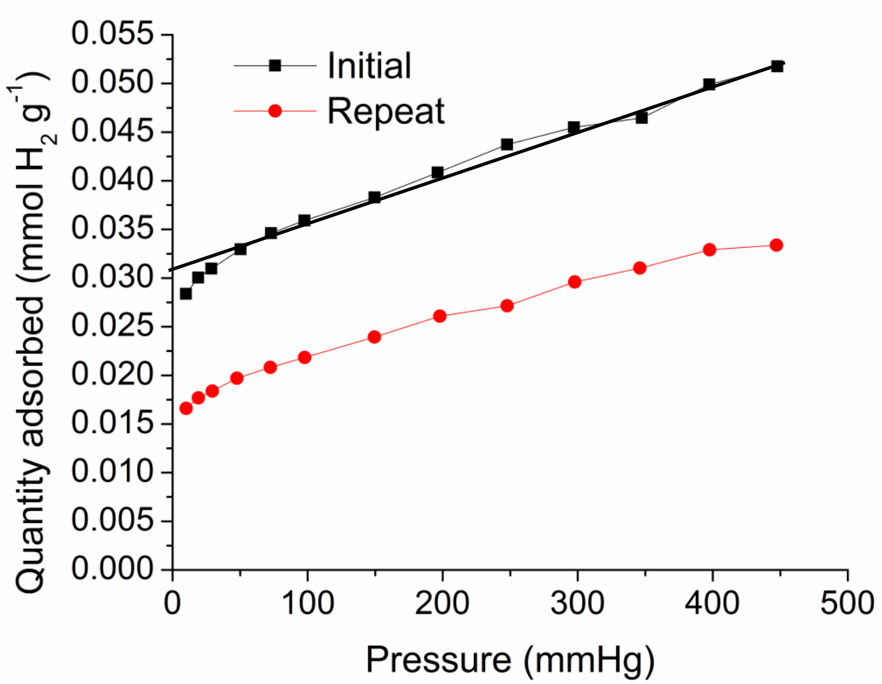

Figure 1.6: Hydrogen chemisorption isotherm for a 5 wt% Pt/Al_2O_3 catalyst purchased from Sigma-Aldrich.

It should also be noted that the temperature of the chemisorption analysis will impact the results.[16,59,60] Hydrogen and carbon monoxide chemisorption analysis on metals such at Pt are typically done at 308 K. However, a bulk Pd-H beta phase will form at 308 K which will ad to the hydrogen uptake on Pd surface atoms. For this reason, hydrogen chemisorption analysis on Pd is often carried out at elevated temperatures. The analyses reported in this dissertation utilized 373 K for hydrogen chemisorption on Pd, which is above the decomposition temperature of the Pd-H beta phase.[16,17,55]

1.5. X-Ray diffraction

Powder X-ray diffraction (XRD) is a characterization tool that can reveal valuable information about a catalyst's crystal structure and particle size. Characteristic XRD patterns are produced as the inner shell electrons of the powder sample reach a sufficient energy that result in intense peaks of reflected radiation.[62] The scattering of the waves within the crystal lattice are governed by Bragg's law, shown in equation 1:

$$n\lambda = 2dsin\theta \qquad \text{Eq. 1}$$

where n is a positive integer, λ is the wavelength of the incident wave, and d is the lattice spacing.

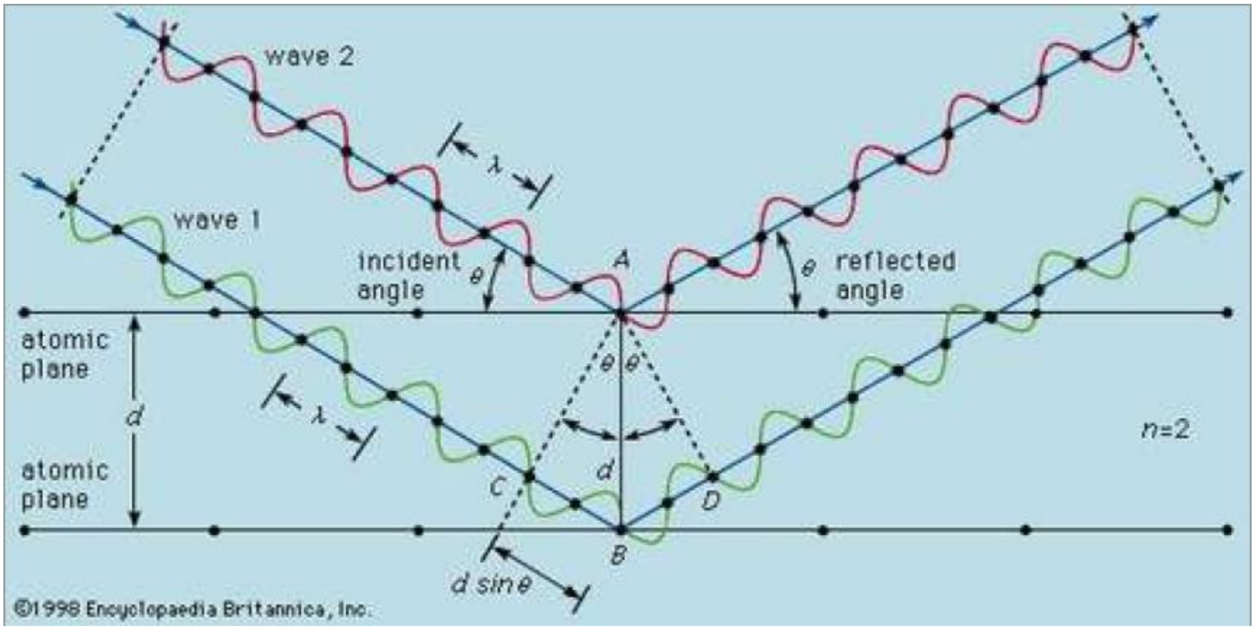

Figure 1.7: Illustration of Bragg diffraction. Image sourced from https://www.britannica.com/science/Bragg-law.[63]

An illustration of Bragg diffraction is shown in Figure 1.7. The d spacing identified in an XRD pattern and the peak location can be used to identify the bulk lattice structures present in a catalyst. In this dissertation, XRD was frequently used to identify alloy phases that were present in bimetallic catalysts. Substitution of a different size atom into a metal lattice will shift the diffraction peak position due to differences in the lattice spacing. For example, substitution of Sn into Pt to form a Pt_3Sn alloy causes the Pt (111) peak at 39.8° (JCPDS 00-004-0802) to shift to 38.9° (JCPDS 00-035-136) due to the increase in the d spacing from 2.27 Å for Pt (111) to 2.31 Å for Pt_3Sn (111). Furthermore, XRD patterns can be used to estimate the particle size of a catalyst through the Scherrer equation[64] shown in equation 2:

$$\tau = \frac{K\lambda}{\beta \cos\theta} \qquad \text{Eq. 2}$$

where τ is the average size of the nanoparticles, K is a dimensionless shape factor, λ is the X-ray wavelength, θ is the Bragg angle, and β is the full width half max of the diffraction peak. However, the accuracy of the Scherrer equation is questionable due to the relative contribution of large particles compared to smaller particles to XRD patterns due to more scattering events occurring within the larger particles. Therefore, particle sizes of supported nanoparticles derived from the Scherrer equation should be validated against chemisorption and microscopy results.

1.6. Electron microscopy

Transmission electron microscopy (TEM) and scanning transmission electron microscopy (STEM) are analytical tools that reveal atomic-level insights into catalyst structure and composition. These microscopy techniques utilize a beam of electrons that is transmitted through a sample to form an image. High resolution TEM images can reveal details such as particle size distributions and crystal grains within a nanoparticle sample. Dark-field STEM images can be used to accurately image atomically dispersed atoms on various catalyst supports. Together, these techniques allow for a relatively accurate measurement of bimetallic nanoparticle size distributions that are not accurately measured using techniques such as chemisorption and XRD. Chemisorption can only measure exposed metals that interact with the probe molecules. In this dissertation, Sn is not active for the chemisorption of hydrogen or carbon monoxide. Thus, chemisorption cannot be used to estimate PdSn or PtSn nanoparticle sizes. X-Ray diffraction is more sensitive towards large particles which makes it ineffective at measuring the size of very small (~1 nm) particles that may be present in a sample. Microscopy is therefore the most suited technique for analyzing particle size distributions in bimetallic catalysts when a wide range of particle sizes are present and when only one metal is active for chemisorption.

Additionally, elemental mapping using energy dispersive X-ray spectroscopy (EDS) is possible while in STEM mode. Elemental analysis is accomplished by focusing a beam of electrons into a sample. Electrons from an inner shell are excited and ejected leaving a hole behind. An electron from a higher-energy shell will fill the hole, releasing an X-ray with equivalent energy to the energy difference of the two shells.[65] The ejected X-rays are measured by an energy-dispersive spectrometer.

The EDS analysis of a catalyst can be used to analyze the composition a single point or to create a map of several elements and their relative positions.[66] Figure 1.8 shows a sample selection of EDS maps illustrating the location of Pt and Bi with respect to each other on a Pt-Bi bimetallic catalyst.[67] In Fig 1.8, EDS mapping is used to compare the location of Pt and Bi on the as-prepared catalyst (Figure 1.8 a-d), the catalyst subjected to a pre-treatment condition at 328 K under He in 0.1 M hexanediol (Figure 1.8 e-h), and the catalyst after being used to oxidize 0.1 M hexanediol in an O_2 environment at 328 K (Figure 1.8 i-l). The EDS mapping on a state-of-the-art microscope, like the one used to collect the images in Figure 1.8, can be utilized to map nanoparticles 5 nm and below in diameter. Valuable information about catalyst restructuring under reaction conditions can be obtained utilized EDS analysis.

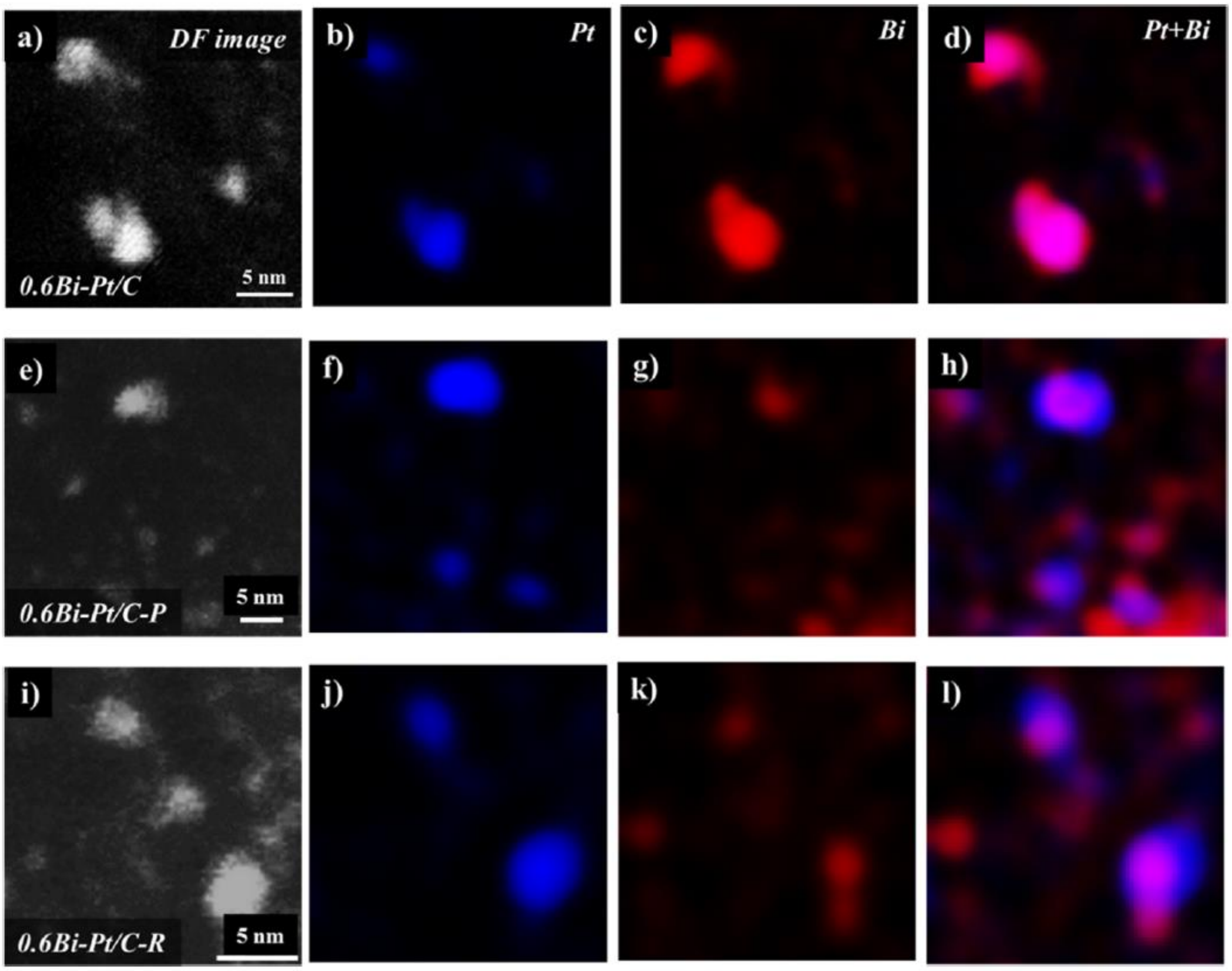

Figure 1.8: STEM-EDS maps of 0.6 Bi-Pt/C (a-d),)0.6 Bi-Pt/C-P (e-h), and 0.6 Bi-Pt/C-R (i-l) including dark-field STEM images (a,e,i), EDS maps of Pt (b,f,j), EDS maps of Bi (c,g,k) and the overlaid maps of Pt and Bi (d,h,l). Pt and Bi are shown in blue and red, respectively.Reprinted with permission from Xie, J. *et al.* Influence of Dioxygen on the Promotional Effect of Bi during Pt- Catalyzed Oxidation of 1 , 6-Hexanediol. *ACS Catal.* **6,** 4206–4217 (2016). Copyright 2016 American Chemical Society[67]

1.7. Diffuse reflectance infrared Fourier transform spectroscopy

Diffuse reflectance infrared Fourier transform spectroscopy (DRIFTS) is a fast and non-destructive spectroscopic technique that can provide both chemical and structural information about a solid surface.[68] An illustration of diffuse reflectance is shown in Figure 1.9. The DRIFTS spectra are often reported using Kubelka-Munk units which relate the sample concentration to the scattered radiation intensity.[69,70] The Kubelka-Munk equation is shown in equation 3:

$$f(R_\infty) = \frac{(1-R_\infty)^2}{2R_\infty} = \frac{k}{s} \qquad \text{Eq. 3}$$

where R_∞ is the absolute reflectance of the layer, s is a scattering coefficient, and k is the molar absorption coefficient.[70] Various probe molecules can be used with the DRIFTS technique including CO, which can reveal information about exposed metal facets and alloying[71], pyridine to probe for acid sites[72,73], and CO_2 to probe for base sites[73].

The position of CO bands during IR studies will be influenced by dipole-dipole coupling of adsorbed CO as well as any electronic promotion effects from alloying. Dipole-dipole coupling can result in an upward shift of at least 30 cm^{-1} with respect to the singleton frequency.[74] Dilution of surface ensembles through alloying increases the distance between CO molecules resulting in a decrease in CO-CO dipole coupling and a subsequent shift to lower wave numbers. This can be considered a geometric promotion effect. Electronic, or ligand, effects arise from the donation of electronic charge due to an added promoter. For example, Pt alloyed with Cu increases the back donation of Pt d-band electrons into antibonding 2π-orbitals of CO resulting in a weakened Pt-CO bond and a shift to lower absorption frequencies.[74] It is difficult to differentiate between the influence of ensemble dilution (geometric promotion) and ligand effects (electronic promotion) without using techniques such as the isotopic dilution method that uses mixtures of ^{12}CO and ^{13}CO to remove the effect of CO-CO dipole coupling on the position of CO-Pt absorption bands. However, significant shifts in the CO absorption bands on Pt-$metal_{inert}$ nanoparticles can still be used to identify the presence surface interactions between the two metals.

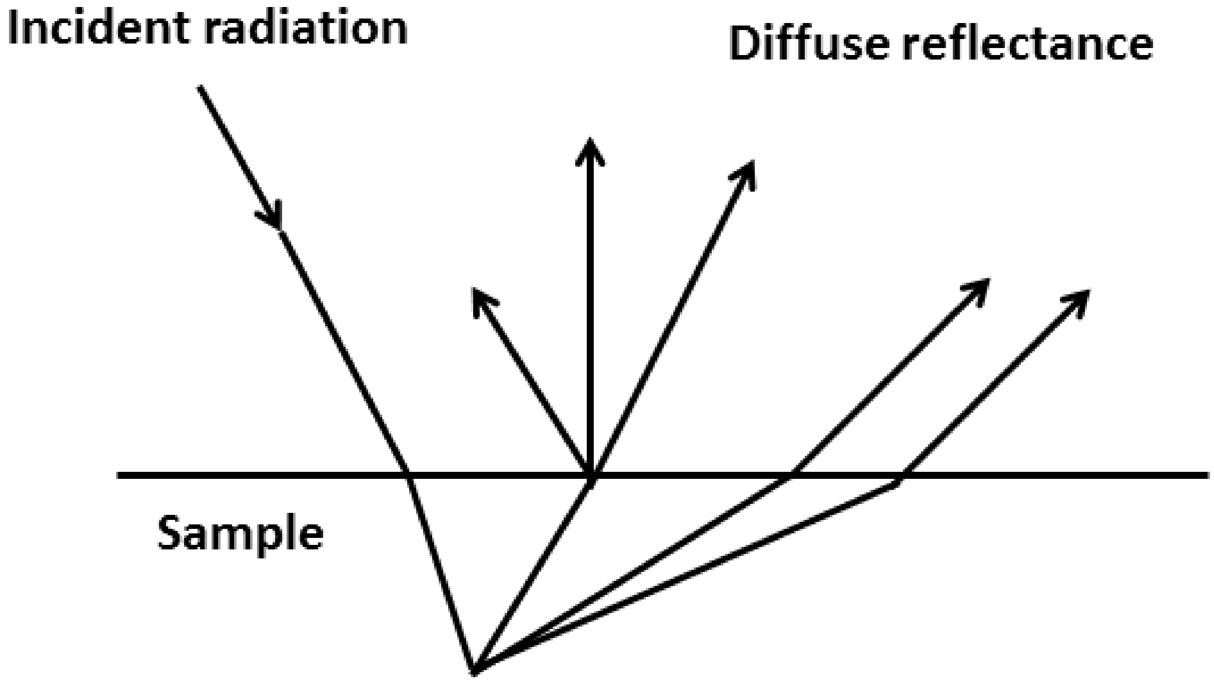

Figure 1.9: Illustration of diffuse reflectance.

1.8. X-Ray absorption spectroscopy

X-Ray absorption spectroscopy (XAS) is a valuable characterization technique that can be used to determine the oxidation state and local geometry of supported nanoparticles. The collection of XAS data is generally conducted using synchrotron radiation sources. Each element has a specific energy required to excite a core electron. For example, the element Sn possesses a K-edge energy of 29.2 KeV. At this edge energy, a 1s electron in the atom's core shell will transition to an unoccupied bound state or to a continuum state at higher energies.

The absorption process of photoelectrons and XAS features are illustrated in Figure 1.10. Two primary regions exist in XAS data: the near edge and the fine structure. X-ray absorption near-edge structure (XANES) includes the region very close to the absorption edge. The XANES region is sensitive to chemical bonding and multiple scattering effects.[75] The edge energy location, pre-edge features, and white line intensity (maximum intensity of the edge rise) found in the XANES region can be compared to standard compounds to determine information such as the oxidation state.

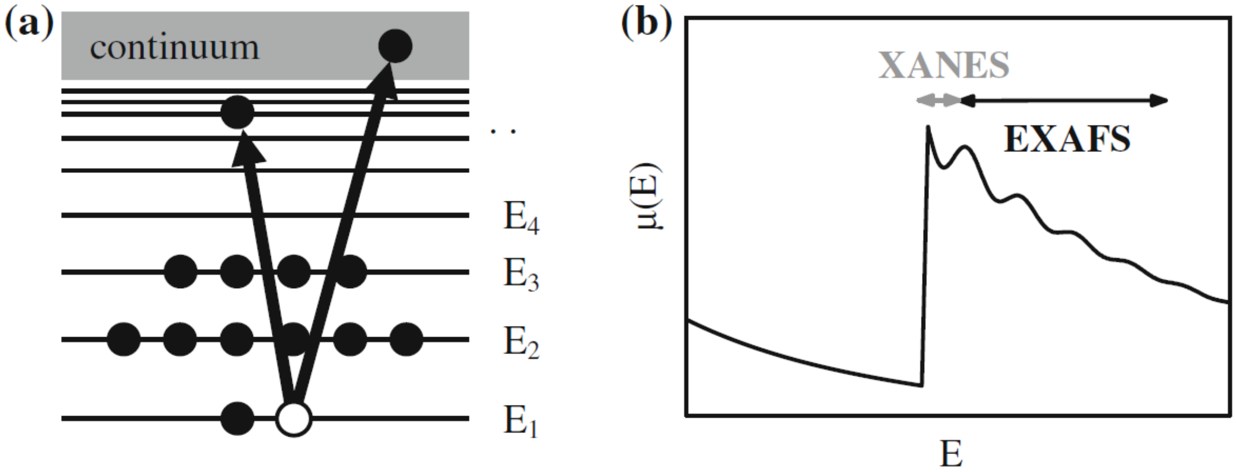

Figure 1.10: Schematic of the (a) absorption process and (b) absorption coefficient μ(E) versus photon energy E including the fine structure above the edge divided into the XANES and EXAFS regions.[75]

The fine structure region, known as the extended X-ray absorption fine structure (EXAFS) is found at photon energies higher than ~30 eV above the edge when the photoelectron is in a free or continuum state.[75] In this higher energy region, the EXAFS depends primarily on the atomic arrangement around the absorber. The coordination numbers, nearest neighbors, and interatomic distances can be derived from the EXAFS region.

1.9. X-Ray photoelectron spectroscopy

X-Ray photoelectron spectroscopy (XPS) is a technique used to measure the oxidation states and chemical composition of the outer layers of a material. Samples are irradiated using monoenergetic soft x-rays. Photoelectrons interact with atoms at depths of tens of angstroms causing electrons to be emitted by the photoelectric effect, illustrated in Figure 1.11, with kinetic energies given by equation 4:

$$KE = h\nu - BE - \phi_s \qquad \text{Eq. 4}$$

where $h\nu$ is the energy of the photon, BE is the binding energy of the atomic orbital from which the electron originates, and ϕ_s is the work function of the spectrometer.[76] The BE is the difference in energy between the initial and final states after the photoelectron is ejected. These binding energies for a given element are unique, thus providing a fingerprint for identifying the presence of elements and their relative concentrations. In the context of bimetallic catalysts, XPS can reveal information regarding the surface composition versus bulk composition through a comparison with ICP-OES, as well as the extent of reduction of oxophilic promoters near the surface of the particles. Shifts in the binding energies arise due to differences in chemical potential and polarization,[76] which can be caused by the influence of a promoter through alloy formation or electron donation.

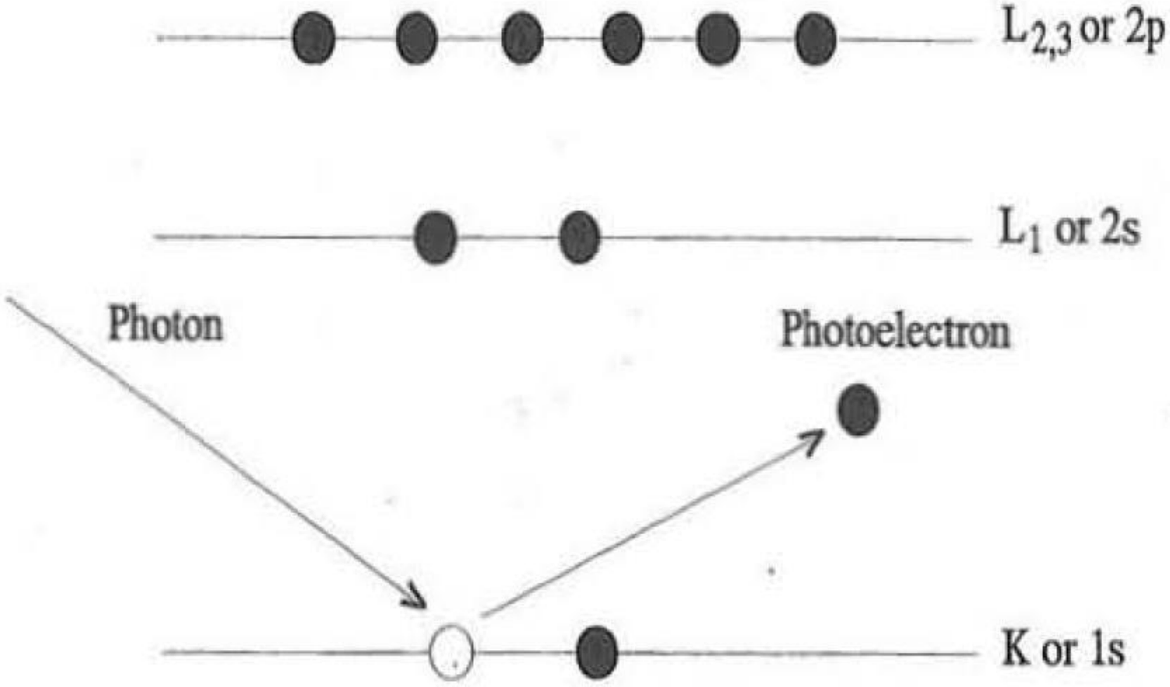

Figure 1.11: The XPS emission process for a model atom. Image sourced from *Handbook of X-ray Photoelectron Spectroscopy*. (Perkin-Elmer Corporation, 1992).[76]

1.10. Focus of this work

In this dissertation, the influence of Sn promoter was explored using two different probe reactions. The first was the conversion of heptanoic acid. The reaction of heptanoic acid over Pd and PdSn catalysts allowed for the influence of Sn promotor in the presence of oxygenated species to be explored. The second probe reaction was the conversion of propane which was operated under high temperature reducing conditions devoid of oxygenated species. The goals of this dissertation are as follows:

1. Understand the influence of Pd particle size on the conversion of heptanoic acid.
2. Elucidate the influence of Sn proximity to Pd catalysts in the presence of oxygenated species.
3. Evaluate the effect of Sn proximity to Pd on its oxidation state.
4. Probe the influence of Sn content and support material on Pt catalysts under reducing conditions.
5. Investigate the influence of synthesis method on the behavior of Pt-Sn catalysts.
6. Evaluate the influence of co-fed H_2 during the dehydrogenation of propane over Pt and Pt-Sn catalysts.

1.11. References for Chapter 1

1. Lipinsky, E. S. Chemicals from biomass: petrochemical substitution options. *Science* **212,** 1465–71 (1981).

2. Keim, W. Petrochemicals: Raw material change from fossil to biomass? *Pet. Chem.* **50,** 298–304 (2010).

3. De Clercq, R., Dusselier, M. & Sels, B. F. Heterogeneous catalysis for bio-based polyester monomers from cellulosic biomass: advances, challenges and prospects. *Green Chem.* 5012–5040 (2017). doi:10.1039/C7GC02040F

4. Sattler, J. J. H. B., Ruiz-Martinez, J., Santillan-Jimenez, E. & Weckhuysen, B. M. Catalytic Dehydrogenation of Light Alkanes on Metals and Metal Oxides. *Chem. Rev.* **114,** 10613–10653 (2014).

5. Fu, J., Lu, X. & Savage, P. E. Fuels of the future. *Energy Environ. Sci.* **3,** 253 (2010).

6. Alper, J. *The Changing Landscape of Hydrocarbon Feedstocks for Chemical Prodction: Implications for Catalysis: Proceedings of a Workshop*. (The National Academies Press, 2016). doi:10.17226/23555

7. Swinnen, J. & Tollens, E. Bulk chemicals from biomass in the EC: feasibility and potential outlets. *Bioresour. Technol.* **36,** 277–291 (1991).

8. Roddy, D. J. Biomass in a petrochemical world. *Interface Focus* **3,** 20120038–20120038 (2012).

9. Vennestrøm, P. N. R., Osmundsen, C. M., Christensen, C. H. & Taarning, E. Beyond petrochemicals: The renewable chemicals industry. *Angew. Chemie - Int. Ed.* **50,** 10502–10509 (2011).

10. Sun, K., Wilson, A. R., Thompson, S. T. & Lamb, H. H. Catalytic Deoxygenation of Octanoic Acid over Supported Palladium: Effects of Particle Size and Alloying with Gold. *ACS Catal.* **5,** 1939–1948 (2015).

11. Ford, J. P., Immer, J. G. & Lamb, H. H. Palladium Catalysts for Fatty Acid Deoxygenation: Influence of the Support and Fatty Acid Chain Length on Decarboxylation Kinetics. *Top. Catal.* **55,** 175–184 (2012).

12. Immer, J. G., Kelly, M. J. & Lamb, H. H. Catalytic reaction pathways in liquid-phase deoxygenation of C18 free fatty acids. *Appl. Catal. A Gen.* **375,** 134–139 (2010).

13. Snåre, M., Kubičková, I., Mäki-Arvela, P., Eränen, K. & Murzin, D. Y. Heterogeneous catalytic deoxygenation of stearic acid for production of biodiesel. *Ind. Eng. Chem. Res.* 5708–5715 (2006).

14. Mäki-Arvela, P., Snåre, M., Eränen, K., Myllyoja, J. & Murzin, D. Y. Continuous decarboxylation of lauric acid over Pd/C catalyst. *Fuel* **87,** 3543–3549 (2008).

15. Snåre, M. *et al.* Production of diesel fuel from renewable feeds: Kinetics of ethyl stearate

decarboxylation. *Chem. Eng. J.* **134,** 29–34 (2007).

16. Lopez-Ruiz, J. A. & Davis, R. J. Decarbonylation of heptanoic acid over carbon-supported platinum nanoparticles. *Green Chem.* **16,** 683 (2014).

17. Lopez-Ruiz, J. A., Pham, H. N., Datye, A. K. & Davis, R. J. Reactivity and stability of supported Pd nanoparticles during the liquid-phase and gas-phase decarbonylation of heptanoic acid. *Appl. Catal. A Gen.* **504,** 295–307 (2015).

18. Lopez-Ruiz, J. A. Decarbonylation of Carboxylic Acids over Supported Metal Catalysts. (University of Virginia, 2014).

19. Peplow, M. The Great Gas Business. *Nature* **550,** 26–28 (2017).

20. Ramberg, D. J., Henry Chen, Y. H., Paltsev, S. & Parsons, J. E. The economic viability of gas-to-liquids technology and the crude oil–natural gas price relationship. *Energy Econ.* **63,** 13–21 (2017).

21. Caporin, M. & Fontini, F. The long-run oil–natural gas price relationship and the shale gas revolution. *Energy Econ.* **64,** 511–519 (2017).

22. Brown, S. P. A. Natural gas vs. oil in U.S. transportation: Will prices confer an advantage to natural gas? *Energy Policy* **110,** 210–221 (2017).

23. Batten, J. A., Ciner, C. & Lucey, B. M. The Dynamic Linkages between Crude Oil and Natural Gas Markets. *Energy Econ.* **62,** 1–32 (2016).

24. Stangland, E. E. Shale Gas Implications for C 2 -C 3 Olefin Production : Incumbent and Future Technology. *Annu. Rev. Chem. Biomol. Eng.* 15.1-15.24 (2018).

25. Sloan, M. *IFC International, Inc.: 2016 Propane Market Outlook*. (2016).

26. Rahimpour, M. R., Jafari, M. & Iranshahi, D. Progress in catalytic naphtha reforming process: A review. *Appl. Energy* **109,** 79–93 (2013).

27. Mazzieri, V. A., Grau, J. M., Yori, J. C., Vera, C. R. & Pieck, C. L. Influence of additives on the Pt metal activity of naphtha reforming catalysts. *Appl. Catal. A Gen.* **354,** 161–168 (2009).

28. Contreras-Andrade, I., Vazquez-Zavala, A. & Viveros, T. Influence of the Synthesis Method on the Catalytic Behaviour of Pt and PtSn/Al2O3 Reforming Catalyst. *Energy and Fuels* **23,** 3835–3841 (2009).

29. de Lima, S. M. *et al.* New approaches to improving catalyst stability over Pt/ceria during ethanol steam reforming: Sn addition and CO2 co-feeding. *Appl. Catal. B Environ.* **96,** 387–398 (2010).

30. Pham, H. N., Sattler, J. J. H. B., Weckhuysen, B. M. & Datye, A. K. The Role of Sn in the Regeneration of Pt/γ-Al2O3 Light Alkane Dehydrogenation Catalysts. *ACS Catal.* **6,** 2257–2264 (2016).

31. Xiong, H. *et al.* Thermally Stable and Regenerable Platinum – Tin Clusters for Propane Dehydrogenation Prepared by Atom Trapping on Ceria. *Angew. Chem. Int. Ed. Engl.* **56,** 1–7 (2017).

32. Hill, J. M., Cortright, R. D. & Dumesic, J. A. Silica- and L-zeolite-supported Pt , Pt/Sn and Pt/Sn/K catalysts for isobutane dehydrogenation. *Appl. Catal. A Gen.* **168,** 9–21 (1998).

33. Yang, M.-L., Zhu, Y.-A., Zhou, X.-G., Sui, Z.-J. & Chen, D. First-Principles Calculations of Propane Dehydrogenation over PtSn Catalysts. *ACS Catal.* **2,** 1247–1258 (2012).

34. Shan, Y., Sui, Z., Zhu, Y., Chen, D. & Zhou, X. Effect of steam addition on the structure and activity of Pt – Sn catalysts in propane dehydrogenation. *Chem. Eng. J.* **278,** 240–248 (2015).

35. Stagg, S. M., Querini, C. A., Alvarez, W. E. & Resasco, D. E. Isobutane Dehydrogenation on Pt-Sn/SiO2 Catalysts: Effect of Preparation Variables and Regeneration Treatments. *J. Catal.* **94,** 75–94 (1997).

36. Resasco, D. E. in *Encyclopedia of Catalysis* (2000).

37. Huber, G. W., Shabaker, J. W. & Dumesic, J. A. Raney Ni-Sn catalyst for H2 production from biomass-derived hydrocarbons. *Science* **300,** 2075–7 (2003).

38. Nishiyama, S. & Hara, T. Infrared spectroscopy study of aldehydes adsorbed on Rh-Sn bimetallic systems: Selective activation of aldehydes by tin. *J. Phys. Chem. B* 4431–4439 (1999).

39. Yokoyama, T. & Yamagata, N. Hydrogenation of carboxylic acids to the corresponding aldehydes. *Appl. Catal. A Gen.* **221,** 227–239 (2001).

40. Nishiyama, S., Kubota, T. & Kimura, K. Unique hydrogenation activity of supported tin catalyst: Selective hydrogenation catalyst for unsaturated aldehydes. *J. Mol. Catal. A* **1169,** (1997).

41. Pestman, R., Duijne, A. van, Pieterse, J. A. Z. & Ponec, V. The formation of ketones and aldehydes from carboxylic acids , structure-activity relationship for two competitive reactions. *J. Mol. Catal. A Chem.* **1169,** (1995).

42. Taniya, K., Jinno, H., Kishida, M., Ichihashi, Y. & Nishiyama, S. Preparation of Sn-modified silica-coated Pt catalysts: A new PtSn bimetallic model catalyst for selective hydrogenation of crotonaldehyde. *J. Catal.* **288,** 84–91 (2012).

43. Xie, J. *et al.* Deactivation of Supported Pt Catalysts during Alcohol Oxidation Elucidated by Spectroscopic and Kinetic Analyses. *ACS Catal.* **7,** 6745–6756 (2017).

44. Alonso, D. M., Wettstein, S. G. & Dumesic, J. A. Bimetallic catalysts for upgrading of biomass to fuels and chemicals. *Chem. Soc. Rev.* **41,** 8075–98 (2012).

45. Moliner, M., Roman-Leshkov, Y. & Davis, M. E. Tin-containing zeolites are highly active catalysts for the isomerization of glucose in water. *Proc. Natl. Acad. Sci.* **107,** 6164–6168 (2010).

46. González-Borja, M. Á. & Resasco, D. E. Anisole and guaiacol hydrodeoxygenation over monolithic Pt-Sn catalysts. *Energy and Fuels* **25,** 4155–4162 (2011).

47. Musci, J. J., Merlo, A. B. & Casella, M. L. Aqueous phase hydrogenation of furfural using carbon-supported Ru and RuSn catalysts. *Catal. Today* **296,** 43–50 (2017).

48. Pouilloux, Y., Autin, F., Guimon, C. & Barrault, J. Hydrogenation of Fatty Esters over Ruthenium–Tin Catalysts; Characterization and Identification of Active Centers. *J. Catal.* **176,** 215–224 (1998).

49. Pestman, R., Koster, R. M., Pieterse, J. A. Z. & Ponec, V. Reactions of Carboxylic Acids on Oxides 1 . Selective Hydrogenation of Acetic Acid to Acetaldehyde. *J. Catal.* **168,** 255–264 (1997).

50. Sakata, Y., van Tol-Koutstaal, C. A. & Ponec, V. Selectivity Problems in the Catalytic Deoxygenation of Benzoic Acid. *J. Catal.* **169,** 13–21 (1997).

51. Alonso, D. M., Wettstein, S. G. & Dumesic, J. A. Bimetallic catalysts for upgrading of biomass to fuels and chemicals. *Chem. Soc. Rev.* **41,** 8075–8098 (2012).

52. Robinson, A. M., Hensley, J. E. & Medlin, J. W. Bifunctional Catalysts for Upgrading of Biomass-Derived Oxygenates : A Review. *ACS Catal.* **6,** 5026–5043 (2016).

53. Lam, Y. M. & Boudart, M. Preparation of small Au-Pd particles on silica. *J. Catal.* **50,** 530–540 (1977).

54. Davis, R. J. & Boudart, M. Structure of Supported PdAu Clusters Determined by X-ray Absorption Spectroscopy. *J. Phys. Chem.* **98,** 5471–5477 (1994).

55. Kaylor, N. *et al.* Vapor phase deoxygenation of heptanoic acid over silica-supported palladium and palladium-tin catalysts. *J. Catal.* **344,** 202–212 (2016).

56. Dong, H., Chen, Y.-C. & Feldmann, C. Polyol synthesis of nanoparticles: status and options regarding metals, oxides, chalcogenides, and non-metal elements. *Green Chem.* **17,** 4107–4132 (2015).

57. Baranova, E. A. *et al.* Single-step polyol synthesis of alloy Pt7Sn3 versus bi-phase Pt/SnOx nano-catalysts of controlled size for ethanol electro-oxidation. *J. Appl. Electrochem.* **40,** 1767–1777 (2010).

58. Okhlopkova, L. B. *et al.* Palladium–zinc catalysts on mesoporous titania prepared by colloid synthesis. I. Size control synthesis of PdZn nanoclusters by a polyol method. *J. Nanoparticle Res.* **14,** 1089 (2012).

59. *Handbook of Heterogeneous Catalysis*. (Wiley-VCH Verlag GmbH & Co. KGaA, 2008). doi:10.1002/9783527610044

60. Bus, E. & van Bokhoven, J. A. Hydrogen chemisorption on supported platinum, gold, and platinum–gold-alloy catalysts. *Phys. Chem. Chem. Phys.* **9,** 2894–2902 (2007).

61. Yudanov, I. V *et al.* CO Adsorption on Pd Nanoparticles: Density Functional and Vibrational Spectroscopy Studies. *J. Phys. Chem. B* **107,** 255–264 (2002).

62. X-ray crystallography. *Wikipedia* (2018). Available at: https://en.wikipedia.org/wiki/X-ray_crystallography#X-ray_diffraction.

63. Bragg law. *Encyclopedia Britannica* (2018).

64. Patterson, A. L. The Scherrer Formula for X-Ray Particle Size Determination. *Phys. Rev.* **56,** 978–982 (1939).

65. Energy-dispersive X-ray spectroscopy. *Wikipedia* (2018). Available at: https://en.wikipedia.org/wiki/Energy-dispersive_X-ray_spectroscopy.

66. Nie, J.-F. Applications of atomic-resolution HAADF-STEM and EDS-STEM characterization of light alloys Applications of atomic-resolution HAADF-STEM and EDS- STEM characterization of light alloys. in *IOP COnference Series: Materials Science and Engineering* 1–8 (2017).

67. Xie, J. *et al.* Influence of Dioxygen on the Promotional Effect of Bi during Pt- Catalyzed Oxidation of 1 , 6-Hexanediol. *ACS Catal.* **6,** 4206–4217 (2016).

68. Accardo, G. *et al. Diffuse Reflectance Infrared Fourier Transform Spectroscopy for the Determination of Asbestos Species in Bulk Building Materials*. *Materials* **7,** (2014).

69. Stuart, B. H. *Infrared Spectroscopy: Fundamentals and Applications*. (John Wiley & Sons, Ltd, 2004).

70. Fuller, M. P. & Griffiths, P. R. Diffuse Reflectance Measurements by Infrared Fourier Transform Spectrometry. *Anal. Chem.* **50,** 1906–1910 (1978).

71. Balakrishnan, K. & Schwank, J. FTIR Study of Bimetallic Pt-Sn / AI203 Catalysts. *J. Catal.* **138,** 491–499 (1992).

72. Falcone, D. D. *et al.* Evidence for the Bifunctional Nature of Pt-Re Catalysts for Selective Glycerol Hydrogenolysis. *ACS Catal.* **5,** 5679–5695 (2015).

73. Hill, I. M., Hanspal, S., Young, Z. D. & Davis, R. J. DRIFTS of Probe Molecules Adsorbed on Magnesia, Zirconia, and Hydroxyapatite Catalysts. *J. Phys. Chem. C* **119,** 9186–9197 (2015).

74. Toolenaar, F. J. C. M., Stoop, F. & Ponec, V. On Electronic and Geometric Effects of Alloying: An Infrared Spectroscopic Investigation of the Adsorption of Carbon Monoxide on Platinum-Copper Alloys. *J. Catal.* **82,** 1–12 (1983).

75. Schnohr, C. S. & Ridgway, M. C. *X-Ray Absorption Spectroscopy of Semiconductors*. **190,** (Springer, 2015).

76. Moulder, J. F., Stickle, W. F., Sobol, P. E. & Bomben, K. D. *Handbook of X-ray Photoelectron Spectroscopy*. (Perkin-Elmer Corporation, 1992).

Chapter 2:

Vapor Phase Deoxygenation of Heptanoic Acid over Silica-Supported Palladium and Palladium-Tin Catalysts*

**This section is adapted from a manuscript that was published in Journal of Catalysis, Volume 344 of December 2016, on pages 202-212.*

Abstract

Silica-supported Pd and PdSn catalysts were prepared by ion exchange or incipient wetness impregnation and characterized with H_2 chemisorption, X-ray diffraction, in situ Sn K-edge X-ray absorption near edge structure (XANES), and transmission electron microscopy. The activity of the catalysts was evaluated in the deoxygenation of vapor-phase heptanoic acid at 0.1 MPa and 573 K. A Pd catalyst synthesized via ion exchange formed nanoparticles of 1.1 ± 0.4 nm and was more stable in heptanoic acid conversion compared to a Pd catalyst synthesized via incipient wetness impregnation having nanoparticles of 2.4 ± 0.5 nm. The addition of Sn to a Pd catalyst by either co-impregnation of precursors or physical mixing of supported monometallic catalysts improved the overall catalyst stability. Moreover, Sn addition expanded the reaction network from primarily decarbonylation over Pd to include dehydration and decarboxylative ketonization over PdSn. Electron microscopy confirmed the physical migration of Sn during catalytic reaction. In situ XANES analysis during the deoxygenation of a carboxylic acid suggests that partially reduced SnO_x is the active Sn phase associated with Pd nanoparticles under reaction conditions.

2.1. Introduction

Biomass is a promising alternative feedstock to petroleum and other fossil carbon sources that is both renewable and readily available.[1–3] Biomass-derived molecules often contain a significantly higher oxygen content compared to molecules obtained from fossil resources. Therefore, oxygen must be selectively removed from those biomass-derived compounds to produce chemicals and fuels. This can be accomplished via several classes of chemical reactions including decarbonylation, decarboxylation, decarboxylative ketonization, and dehydration. [4–7]

Interest in the deoxygenation of biomass-derived organic acids has increased because of a higher demand for biodiesel.[8] Hydrocarbons can be produced via decarboxylation and decarbonylation of carboxylic acids. Snåre et al. investigated a wide variety of metal catalysts for the transformations, utilizing stearic acid as the model carboxylic acid to produce the diesel-like molecule n-heptadecane at 573 K.[4] Continuous flow experiments revealed that Pd/C and Pt/C catalysts deactivate rapidly during deoxygenation reactions utilizing lauric acid as the model acid,[9] depending on the concentration of carboxylic acid in the feed. Faster deactivation occurred when greater concentrations of lauric acid contacted the catalyst. The specific cause of catalyst deactivation, however, is not clear. Mäki-Arvela et al. concluded that coking occurs[9] while others indicate that the carbonaceous species on the catalyst surface are not associated with traditional coke.[10,11] Ping et al. reported that the decrease in the rate of decarbonylation of stearic acid over Pd/SiO_2 results from the adsorption of stearic acid on active sites together with adsorption of unsaturated products and CO.[10]

Sun et al. recently demonstrated how the stability of Pd catalysts used in deoxygenation reactions in 10% H_2/He at 533 K depends on the Pd particle size and alloying.[11] Larger Pd particles were more stable for the deoxygenation of octanoic acid and alloying Pd with Au further improved the stability of the catalyst.

Recent work by Lopez-Ruiz et al. targeted high value alpha olefins formed by the decarbonylation of concentrated heptanoic acid without co-feeding dihydrogen.[12] Alpha olefins are valuable commodity chemicals used in the production of plastics, synthetic lubricants, surfactants, and other materials. Carbon-supported Pt and Pd catalysts were shown to be active for the decarbonylation of heptanoic acid but suffered from rapid deactivation at 573 K and atmospheric pressure.[12,13] Low selectivity to 1-hexene at high conversions was observed for all tested conditions. Indeed, 20% selectivity to the desired alpha olefin product was only achieved at conversions below 10% under vapor phase conditions. The majority of products consisted of internal hexene isomers formed by the rapid isomerization of 1-hexene.

Previous work has shown that Sn can be a beneficial additive to metal catalysts for a range of chemical reactions.[14–20] Electronic effects have been observed in metal-Sn alloys resulting in a decreased heat of adsorption for CO.[21] These reported electronic effects may help decrease the rate of deactivation due to self-poisoning.[22] Furthermore, Chiappero et al. have demonstrated that Pt alloyed with Sn can improve the selectivity to alpha olefins formed during the deoxygenation of methyl esters under semi-batch conditions at temperatures ranging from 593 K to 623 K and pressures ranging from 0.2 MPa to 1.14 MPa.[23] Alpha olefin selectivity improved from 6.5% over Pt to 23% over PtSn at 623 K.

In the present study, vapor phase deoxygenation of heptanoic acid was investigated over Pd and PdSn catalysts. In particular, the stability of the catalysts and the selectivity to higher value products without co-fed dihydrogen were explored. Physical mixtures and two stage catalyst beds were also examined to probe the influence of Sn proximity on the reactivity of Pd nanoparticles. Advanced microscopy techniques and X-ray absorption near-edge structure (XANES) spectroscopy were utilized to characterize the catalysts.

2.2. Experimental Methods

2.2.1. Catalyst synthesis

Two Pd/SiO_2 catalyst samples of nominally 5 wt% each were prepared by ion exchange (IE) or incipient wetness impregnation (IWI) of the Pd precursor using Davisil 636 silica (Sigma-Aldrich) as a support. A high dispersion Pd/SiO_2 sample, denoted as Pd/SiO_2-H, was synthesized via IE using methods modified from a previously described procedure.[24] For example, the $PdCl_2$ precursor (0.510g, 99%, Sigma-Aldrich) was dissolved in a solution of aqueous ammonia (5.428 cm^3 ammonium hydroxide, ACS plus, Fisher Scientific, in 282 cm^3 distilled deionized water). The metal solution was added dropwise over 10 min to 5.70 g of acid-washed Davisil 636 silica in 114 cm^3 of distilled deionized water at 343 K. The metal salt and silica slurry was stirred for 60 min at 343 K, and then cooled to room temperature. The mixture was washed with water and vacuum dried overnight. After calcination in flowing air (medical grade, GTS-Welco) at 673 K for 2 h, the sample was pre-reduced in flowing H_2 (99.999%, GTS-Welco) at 623 K for 2 h. A low dispersion Pd/SiO_2 sample, denoted as Pd/SiO_2-L, was prepared via incipient wetness impregnation (IWI) with 10 wt% $Pd(NO_3)_2\bullet 4NH_3$ in H_2O (99.99%, Sigma-Aldrich), which was further diluted in water prior to impregnation. The sample was calcined in flowing air (medical grade, GTS-Welco) at 673 K for 2 h, and pre-reduced at 623 K in flowing H_2 (99.999%, GTS-Welco) for 2 h.

A Sn/SiO_2 catalyst sample with nominally 5.6 wt% Sn was also prepared by IWI using $SnCl_2$ (98%, Sigma Aldrich) dissolved in water, calcined in flowing air (medical grade, GTS-Welco) at 673 K for 2 h and pre-reduced at 623 K in flowing H_2 (99.999%, GTS-Welco) for 2 h.

Two types of PdSn/SiO_2 samples were prepared. First, Sn was chemically added to a Pd/SiO_2-H sample containing nominally 2.5 wt% Pd by the incipient wetness impregnation method using an aqueous solution of $SnCl_2$. After Sn impregnation, the PdSn sample was calcined and pre-reduced using the same procedure as the Sn/SiO_2 catalyst. This chemically-mixed sample was denoted as PdSn/SiO_2-C. The chemically-mixed Pd-Sn/SiO_2-C sample was prepared with a 1:1 atomic ratio of Pd:Sn having a nominal Pd loading of 2.5 wt% and a nominal Sn loading of 2.8 wt%. To prepare a second Sn and Pd loaded catalyst, the Sn/SiO_2 sample (5.6 wt% Sn) was mechanically mixed with the Pd/SiO_2-H until a uniform mixture was produced. The physically-mixed bimetallic catalyst, denoted as PdSn/SiO_2-P, was prepared with a 1:1 atomic ratio of Pd:Sn having a nominal Pd loading of 2.5 wt% and a Sn loading of 2.8 wt%. All thermal treatments utilized a temperature ramp rate of 1 K min^{-1}.

2.2.2. Dihydrogen chemisorption

The number of available metal surface sites was determined using H_2 chemisorption on a Micromeritics ASAP 2020 adsorption system. Each catalyst sample was evacuated for 10 h at 573 K followed by reduction at 623 K in flowing H_2 (99.999%, GTS-Welco) for 1 h. After reduction, the system was evacuated and cooled to 373 K for analysis. The number of available metal sites was determined by extrapolating the high pressure, linear portion of the isotherm to zero pressure. At 373 K, the stoichiometric ratio of H to surface Pd is 1:1.[13,25]

2.2.3. X-ray diffraction

Powder X-ray diffraction (XRD) patterns were measured on a PANalytical X'Pert Pro equipped with monochromatic Cu Kα-radiation (λ=1.54056 Å) using a step size of 0.0167113°.

2.2.4. Transmission electron microscopy

The high resolution transmission electron microscopy (HR-TEM) and scanning transmission electron microscopy (STEM) utilized in the line scan analysis and energy dispersive spectroscopy (STEM-EDS) maps were performed on an FEI Titan 80-300 operating at 300 kV that is equipped with a Gatan 794 Multi-scan Camera (EFTEM) and an energy dispersive spectrometer for X-ray elemental analysis.

Samples analyzed on the FEI Titan 80-300 were prepared by dispersing catalyst samples in cyclohexane and mounted on holey carbon grids.

Samples for selected area EDS composition analysis were dispersed in ethanol and mounted on holey carbon grids for examination in a JEOL 2010F 200 kV scanning transmission electron microscope equipped with an Oxford Aztec Energy Dispersive System for elemental analysis. Images were recorded in high angle annular dark field (HAADF) mode. Elemental compositions were acquired in selected regions of the sample, as indicated by "boxes" shown in the HAADF-STEM image.

2.2.5. X-ray absorption near-edge structure

The in situ Sn K-edge X-ray absorption near-edge structure (XANES) analysis during temperature programmed reduction (TPR) in H_2 was conducted at the 8C beamline in the Pohang Light Source (PLS) operating with a 3.0 GeV ring energy and a 300 mA ring current. A Si (1 1 1) double crystal monochromator was employed to vary the X-ray photon energy. The XANES spectra were obtained in the transmission mode using ionization gas chambers to detect the primary (I_o, 100% N_2) and the transmitted (I_t 70% N_2, balance Ar) beam intensities. Higher order harmonic contamination was eliminated by detuning the monochromator to reduce the incident X-ray intensity by about 30%. Energy calibration was performed using a standard Sn foil. A self-supported catalyst wafer was loaded into an in situ quartz reactor with a 25.4 mm external diameter. A quartz sample holder with a 15 mm external diameter was positioned in the center of the reactor with a thermocouple port located just about the sample. A mixture of 5% H_2 in He flowed at 100 $cm^3\ min^{-1}$ while the temperature ramped at 5 K min^{-1} from room temperature to 673 K. The catalysts examined by XANES were unreduced samples of Sn/SiO_2, PdSn/SiO_2-C, and PdSn/SiO_2-P. The relative white line intensity of each Sn sample during H_2-TPR was calculated on the basis of the normalized edge jump of Sn foil using: I_r = I (SnOx sample) / I_o (Sn foil).

The in situ Sn K-edge XANES spectra were also collected during butyric acid (99+%, Alfa Aesar) deoxygenation at the same beamline. Butyric acid was chosen as the probe molecule because of its high vapor pressure relative to heptanoic acid. A catalyst sample was pressed into a wafer that was placed directly in the quartz sample holder described above and reduced in situ in 100 cm^3 min^{-1} 5% H_2/He during a heating ramp of 10 K min^{-1} to a temperature of 623 K, after which the temperature was constant for 30 min before cooling to the reaction temperature of 573 K. Dinitrogen flowing at 500 cm^3 min^{-1} was bubbled through liquid butyric acid maintained at room temperature and the mixture was fed to the catalyst held at 573 K for XANES collection. The TPR results were processed using WinXAS 3.1 software and the in situ deoxygenation reaction results were processed using Athena software.

2.2.6. Catalytic deoxygenation of heptanoic acid

Catalysts were evaluated for activity in the deoxygenation of heptanoic acid in a continuous upward flow reactor as described previously.[12] In summary, the reactor consisted of a 0.64 cm OD x 0.089 cm wall thickness stainless steel tube that is 15 cm in length. A pre-heating section of the same material was 10 cm in length. Glass wool was placed above and below the catalyst to maintain the position of the bed. Aluminum heating jackets surrounded the reactor and pre-heating section to facilitate uniform heat transfer.

A liquid feed consisting of 95 wt% heptanoic acid (>98%, Sigma-Aldrich) and 5 wt% dodecane (>99%, Sigma-Aldrich) was pumped from an ISCO 500D syringe pump into the pre-heating section where the feed was vaporized. Dodecane was included in the feed as an internal standard.

The catalysts were reduced in situ with 150 cm^3 min^{-1} H_2 (99.999%, GTS-Welco) at 623 K for 2 h after heating with a ramp rate of 1 K min^{-1}. The reactor was then cooled to 573 K and purged with 200 cm^3 min^{-1} N_2 (99.999%, GTS-Welco) for 1 h.

Liquid-phase products were separated in a condenser positioned above the outlet of the reactor. Initial time on stream was defined as the time which liquid began to enter the condenser. Gaseous products were continuously removed by a 7 cm^3 min^{-1} purge of N_2 (99.999%, GTS-Welco) through the condenser and fed to an on-line HP 5890 Series II gas chromatograph equipped with a ShinCarbon 80/100 packed column and a thermal conductivity detector (TCD). Liquid-phase products were analyzed using an Agilent 7890 gas chromatograph equipped with a ZB-FFAP column and a flame ionization detector (FID).

Using the mass transfer criteria on the conversion of heptanoic acid over supported Pt catalysts described in a previously published paper[12], we verified the lack of internal and external mass transfer effects on the measured rates over the supported PdSn/SiO_2 catalysts used in the current work.

2.2.7. Calculation of rates and selectivity

Conversion was defined as the total rate of formation of the deoxygenation products divided by the molar feed rate of reagent as shown in Eq. 1. In this work, conversion was always less than 20%.

$$\begin{gathered} Conversion = (total\ molar\ formation\ rate\ of\ hexane + 1\text{-}hexene + i\text{-}hexene + heptanal + hexadiene + 2 \\ * tridecanone + unknown\ )/(molar\ rate\ of\ heptanoic\ acid\ fed) \end{gathered} \tag{1}$$

A blank run with SiO_2 support revealed a background conversion that was below 0.1%, and thus background conversion was neglected in this study. The reaction rate over monometallic Pd catalysts was reported as a turnover frequency (TOF), or reaction rate normalized by the number of available surface sites, to properly account for the difference in Pd particle size between the samples. We assumed that the particle size of the active Pd catalyst was equal to the size measured on fresh catalyst sample. The TOF (s^{-1}) is therefore calculated according to Eq. 2.

$$TOF = Conversion * \frac{molar\ rate\ of\ heptanoic\ acid\ fed}{moles\ of\ surface\ metal} \tag{2}$$

Liquid product selectivities were defined by molar rates of product formation divided by total molar rate of formation of all products as shown in Eq. 3.

$$Selectivity = \frac{molar\ rate\ of\ formation\ of\ product, x_i}{total\ molar\ rate\ of\ formation\ of\ products,\ \sum x_i} \tag{3}$$

Gas phase products, consisting of CO and CO_2, were measured relative to a N_2 standard and reported as the %CO in the product gas, defined by Eq. 4.

$$\%CO = \frac{CO}{CO+CO_2} * 100 \tag{4}$$

2.3. Results

2.3.1. Physical properties of Pd/SiO_2 and $PdSn/SiO_2$ catalysts

Physical properties of the catalyst samples, including results from H_2 chemisorption and particle size analysis via electron microscopy, are summarized in Table 1. The Pd/SiO_2-H catalyst prepared by the IE method exhibited the highest H/Pd ratio of 0.80 followed by Pd/SiO_2-L (H/Pd = 0.32). Only 6.1% of the Pd was exposed in the $PdSn/SiO_2$-C despite utilizing the same Pd deposition method to prepare Pd/SiO_2-H. The $PdSn/SiO_2$-P sample mixture also exhibited a decrease in exposed Pd when the sample was reduced at 623 K in flowing H_2 prior to H_2 chemisorption (H/Pd = 0.51). No chemisorbed hydrogen was detected on Sn/SiO_2.

Table 2.1: Physical properties of the Pd, Sn, and PdSn catalysts

Catalyst	**Hydrogen chemisorption (mmol H_2/g of catalyst)**	**H/Pd ratio**	**Particle diameter[a] (nm)**	**Surface-weighted avg. diameter[b] (nm)**	**Nominal metal loading (wt %)**	
					Pd	**Sn**
Pd/SiO_2-L	0.076	0.32	3.1	2.4 ± 0.5	5	-
Pd/SiO_2-H	0.19	0.80	1.3	1.1 ± 0.4	5	-
Sn/SiO_2	0	-	-	-	-	5.6
$PdSn/SiO_2$-C	0.0072	0.061	-	-	2.5	2.8
$PdSn/SiO_2$-P	0.059	0.51	-		2.5	2.8

[a] Result estimated from 1/(H/Pd).

[b] Result calculated from $\sum d^3/\sum d^2$ where diameter (d) is measured using STEM images.

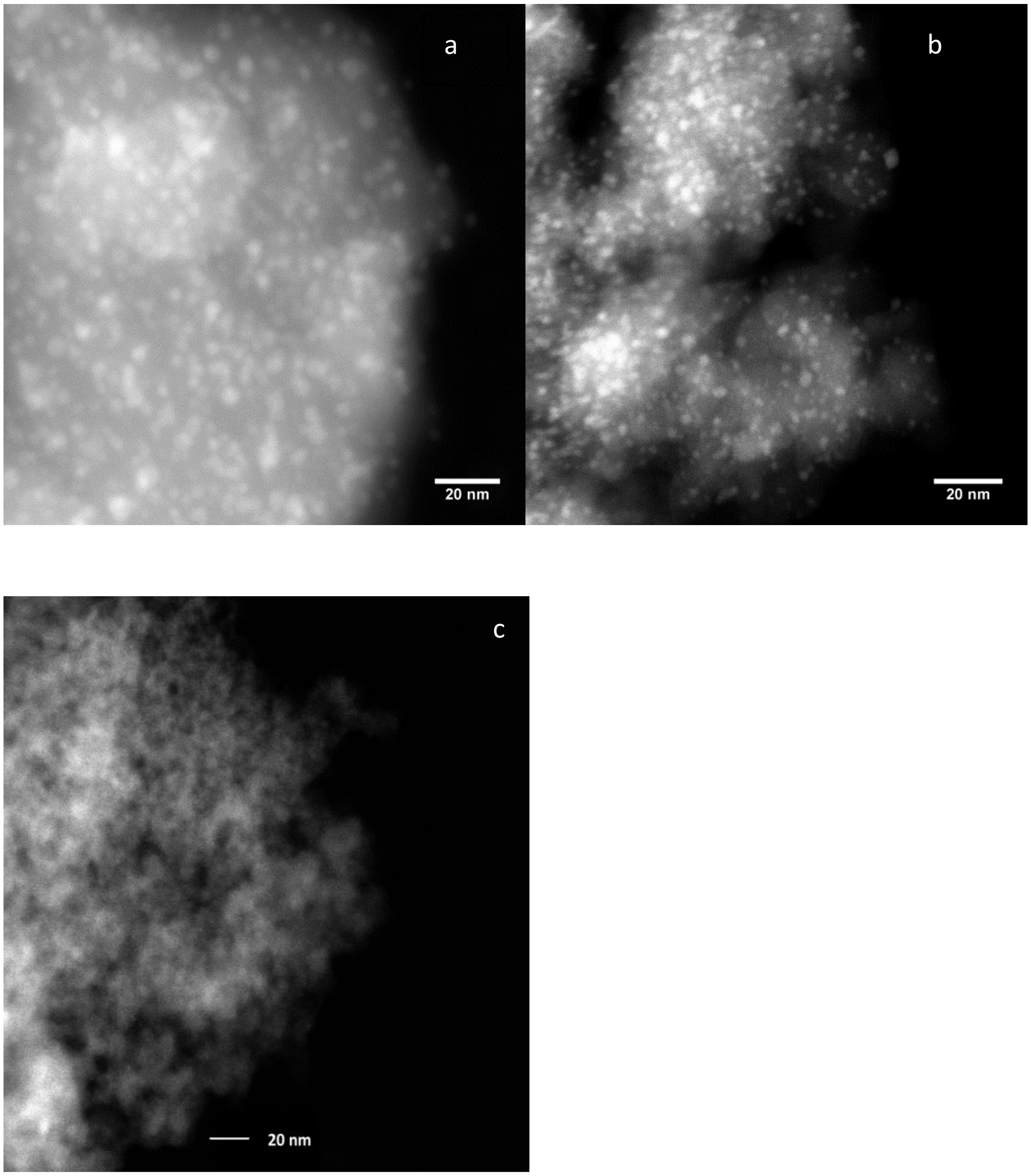

Figure 2.1: Dark field STEM images of fresh a) Pd/SiO_2-L, b) Pd/SiO_2-H, and c) Sn/SiO_2

Figure 2.1 presents dark field STEM images of the fresh monometallic Pd and Sn catalysts. The STEM images for Pd/SiO_2-L and Pd/SiO_2-H show well-dispersed nanoparticles in size ranges of 2.4 ± 0.5 and 1.1 ± 0.4 nm, respectively. As for the Sn/SiO_2 sample, individual nanoparticles were not observed in STEM, but the EDS results confirmed the presence of Sn (not shown) suggesting that Sn may be dispersed as single atoms on SiO_2.[26] Despite depositing the Pd using a technique shown to produce well-dispersed nanoparticles,[24,27–29] a low amount of Pd was exposed to the gas phase in the PdSn/SiO_2-C catalyst. Moreover, a variety of particle sizes was observed in STEM images, ranging from 1 nm to 100 nm (Fig. A1). Drift-corrected EDS line scans were used to characterize the large particles, defined as those in excess of 75 nm, in both the fresh and used catalyst samples. Those results, presented in Fig. A2, indicate the presence of both Pd and Sn in the fresh and used samples.

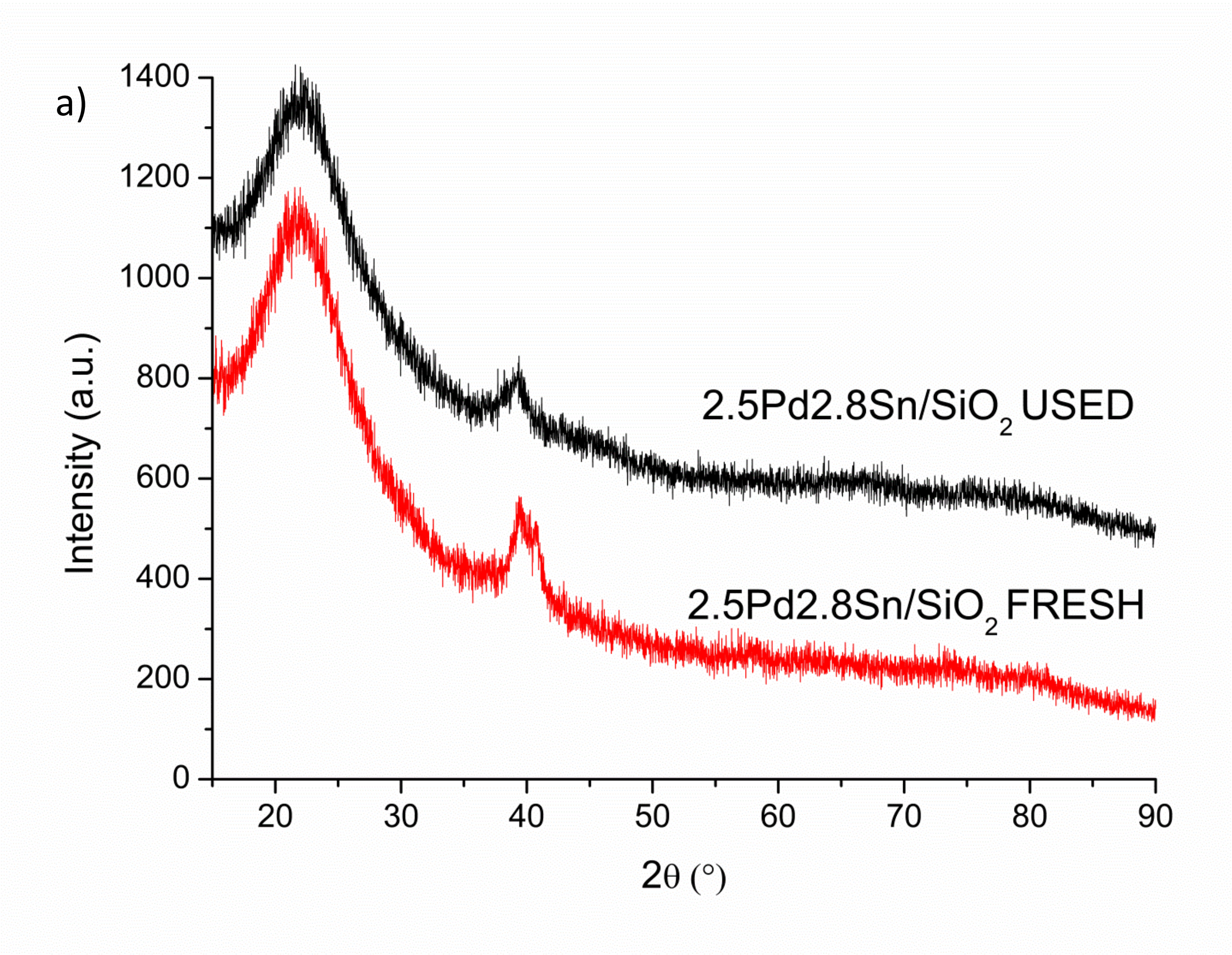

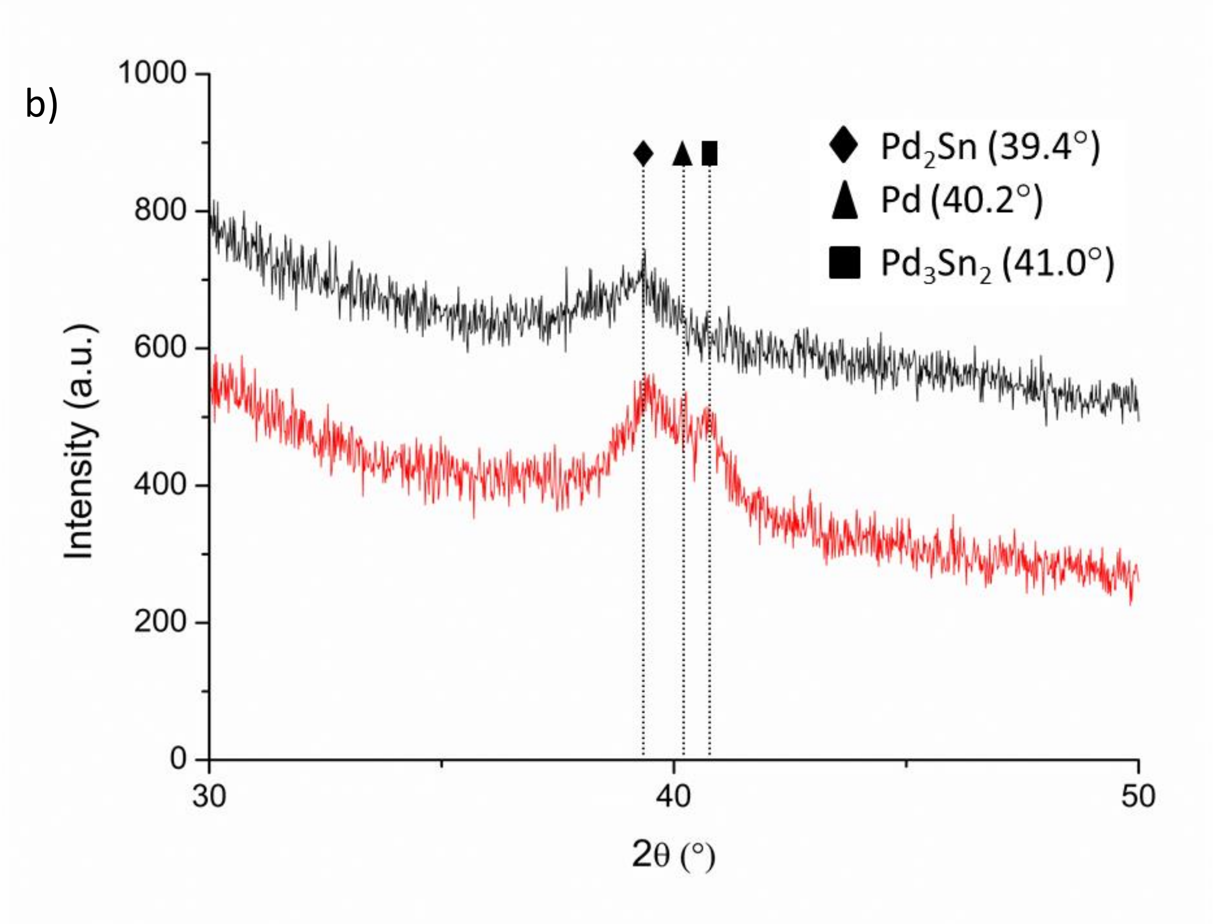

Figure 2.2: XRD pattern for fresh and used PdSn/SiO_2-C from a) 15°-90° and b) zoomed in to 30°-50°. Used catalyst was tested for heptanoic acid conversion at 573 K and 0.1 MPa for 10.75 h.

The samples were examined by X-ray diffraction and no features associated with metal particles were detected on the fresh and used monometallic Pd/SiO_2-H catalyst. Figure 2.2 shows the powder X-ray diffraction patterns of fresh and used PdSn/SiO_2-C together with the positions of selected peaks from reference Pd (JCDPS 00-005-0681), Pd_3Sn_2 (JCPDS 00-007-0170), and Pd_2Sn(JCPDS 00-026-1297). In contrast to the results from monometallic Pd/SiO_2-H, distinct XRD peaks were observed with fresh and used PdSn/SiO_2-C catalysts. The fresh PdSn/SiO_2-C catalyst exhibited a broadened feature with components at 39.4°, 40.2°, and 40.7°. The feature positions are close to characteristic XRD peaks of reference Pd, Pd_3Sn_2, and Pd_2Sn. Used PdSn/SiO_2-C exhibited a weak feature at 39.4° characteristic of Pd_2Sn.

The STEM-HAADF images and results from EDS analyses of a fresh physical mixture of Pd and Sn, denoted as PdSn/SiO$_2$-P, can be found in the supplemental materials (Fig. A3). The EDS results of the fresh catalyst sample indicate Pd and Sn are not present on the same support particles. Clearly, the Pd nanoparticles and the Sn species reside on different silica support particles prior to being subjected to reaction conditions, including pre-reduction. The EDS analysis of used PdSn/SiO$_2$-P confirmed the physical migration of Sn after the catalyst was subjected to in situ pre-reduction and reaction conditions (Fig. A4 and A5). Both Pd and Sn can be found in the same regions of the used catalysts, as well as on the same support particle (Fig. 2.3). The 3-D STEM-EDS maps (Fig. 2.3) of Pd and Sn illustrate the co-location of the metals with respect to each other in the used PdSn/SiO$_2$-P sample. A 3-D STEM-EDS map (Fig. 2.4) of used PdSn/SiO$_2$-C, formed by IWI of Sn on Pd/SiO$_2$, is included for comparison.

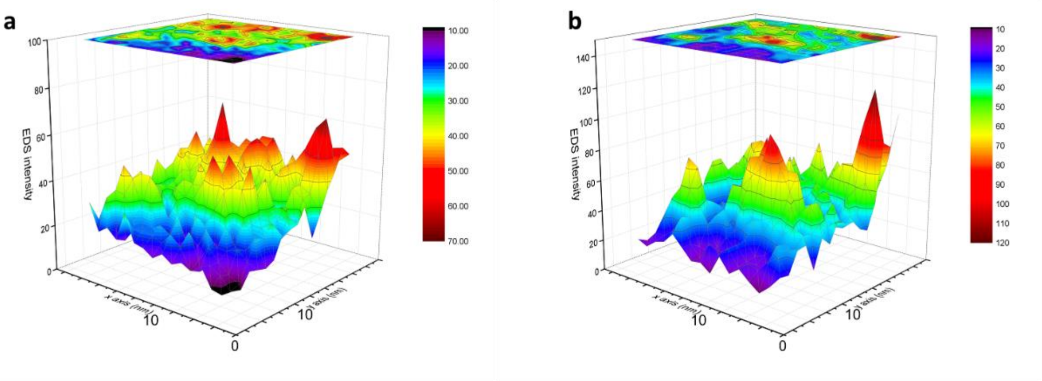

Figure 2.3: 3-D STEM-EDS map of used PdSn/SiO$_2$-P: a) Pd-L map; b) Sn-L map. Used catalyst was tested for heptanoic acid conversion at 573 K and 0.1 MPa for 10.75 h.

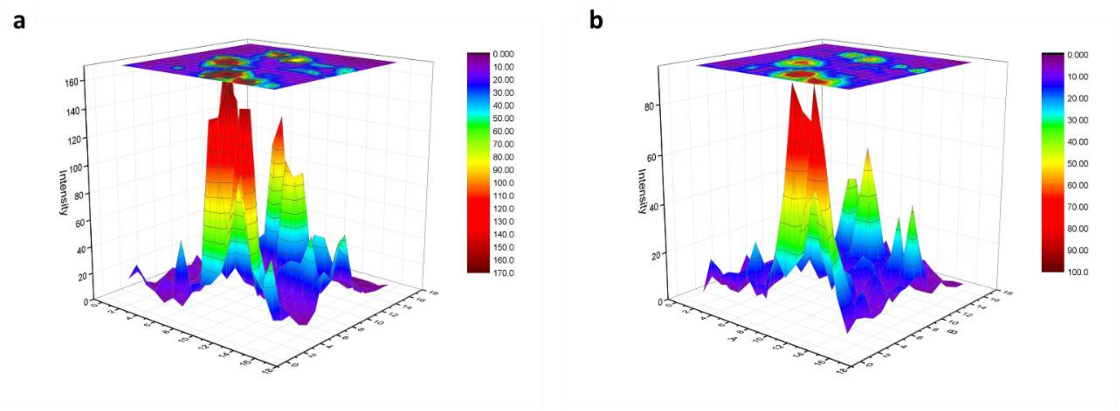

Figure 2.4: 3-D STEM-EDS map of used PdSn/SiO_2-C: a) Pd-L map; b) Sn-L map. Used catalyst was tested for heptanoic acid conversion at 573 K and 0.1 MPa for 10.75 h.

2.3.2. Catalytic activity in deoxygenation of heptanoic acid

2.3.2.1. Particle size effect

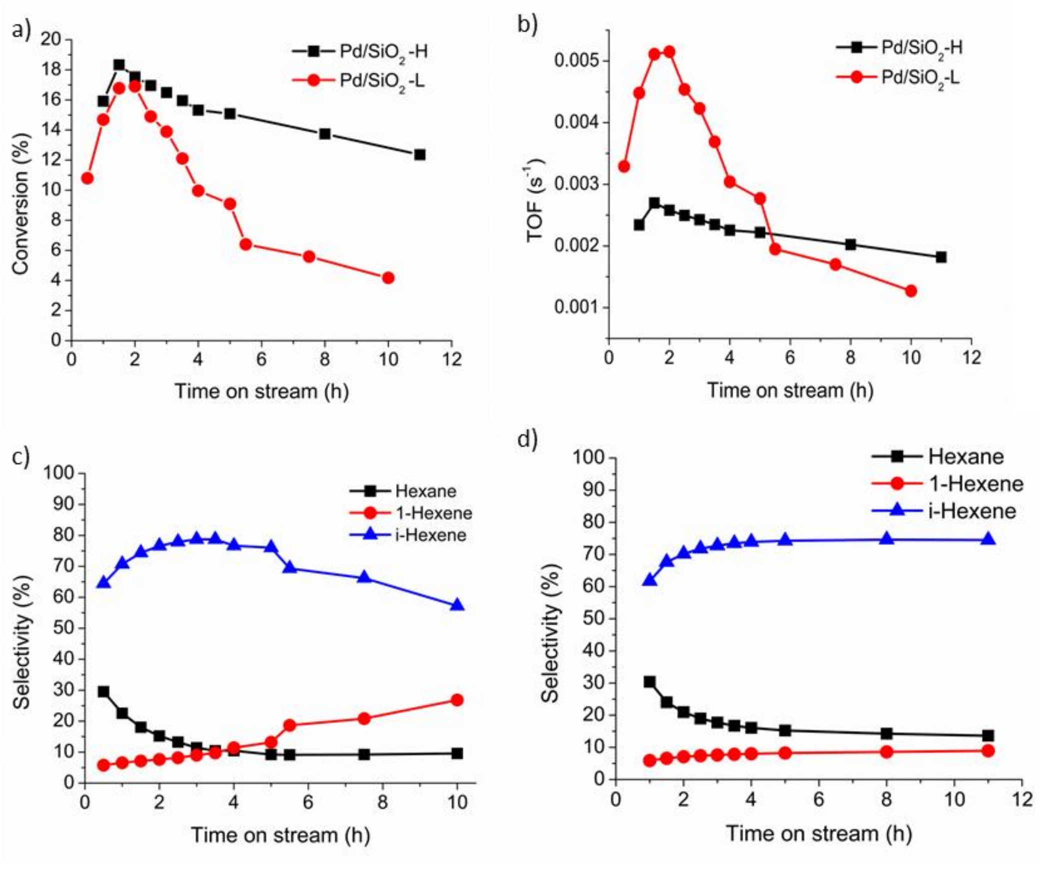

Figure 2.5: a) Conversion and b) TOF of heptanoic acid deoxygenation at 573 K and 0.1 MPa over Pd/SiO_2-L and Pd/SiO_2-H. Product selectivities are shown for c) Pd/SiO_2-L and d) Pd/SiO_2-H.

Metal particle size is correlated to the stability of catalytic Pd nanoparticles during deoxygenation reactions of fatty acids when an excess of H_2 is present.[11] In this study, Pd catalysts with particles differing in size by about a factor of 2 are compared in an environment devoid of excess co-fed H_2. The conversion of heptanoic acid with time over Pd/SiO_2-L and Pd/SiO_2-H is shown in Fig. 2.5a. Both catalysts achieved similar peak conversion of about 17-18% after 1.5 h on stream. The Pd/SiO_2-H catalyst maintained higher conversion after 10 h, exhibiting a 12% conversion of heptanoic acid compared to 4.2% conversion over the Pd/SiO_2-L catalyst. At the observed peak of activity, 1.5 h on stream, the Pd/SiO_2-L had a TOF of 0.0045 s^{-1} compared to Pd/SiO_2-H, which had a TOF of 0.0027 s^{-1}. After 10 h on stream, the TOF exhibited by Pd/SiO_2-L had decreased by 71% to 0.0013 TOF s^{-1}. The TOF over Pd/SiO_2-H decreased by 33% to 0.0018 s^{-1} after 10 h. Evidently initial rate and catalyst stability are inversely related in this system.

Product distributions characteristic of each monometallic Pd catalyst can be found in Fig. 2.5c and 5d. The primary liquid phase (C_6) product formed over both Pd catalysts is hexene, but more than 70% of these olefinic products are 2 and 3-hexene (i-hexene), while approximately 10% of the product is 1-hexene. Higher selectivity to 1-hexene, the direct alpha olefin product from decarbonylation of heptanoic acid, is favored at lower conversions, which is consistent with previous studies by Lopez-Ruiz et al.[12,13] The %CO was measured at 0.5 h time on stream and after 10 h time on stream (Table 2). The total olefin selectivity (1-hexene+i-hexene) is expected to match the %CO in the gas phase products as both are a result of decarbonylation. The %CO observed at 0.5 h and after 10 h time on stream for both the Pd/SiO_2-L and Pd/SiO_2-H are consistent with the observed liquid phase products, i.e. decarbonylation was the primary reaction path over Pd.

Table 2.2: The %CO during heptanoic acid conversion at 573 K

	%CO	
Catalyst	**TOS = 0.50 h**[a]	**TOS = 10.75 h**[a]
Pd/SiO$_2$-L	68	88[b]
Pd/SiO$_2$-H	71	88[c]
PdSn/SiO$_2$-C	8	50
PdSn/SiO$_2$-P	60	39

[a] TOS represents time on stream

[b] Result taken at 10 h time on stream.

[c] Result taken at 11 h time on stream.

2.3.3.2. Effect of Sn addition

Monometallic Sn/SiO$_2$ was relatively inactive in heptanoic acid conversion under the examined reaction conditions at metal loadings comparable to the Pd/SiO$_2$ experiments. For example, conversion of heptanoic acid after 3 h of time on stream was 0.55%, approximately 0.5% higher than the background conversion over silica. The primary product over Sn/SiO$_2$ was 7-tridecanone with a selectivity of 67%. Heptanal, hexadiene, hexane and 1-hexene were the other primary products with selectivities of 9.7%, 8.4%, 7.4%, and 4.4%, respectively. The remaining 3.1% consisted of an unknown product. A complete summary of the product distribution formed over Sn/SiO$_2$ can be found in Fig. A6.

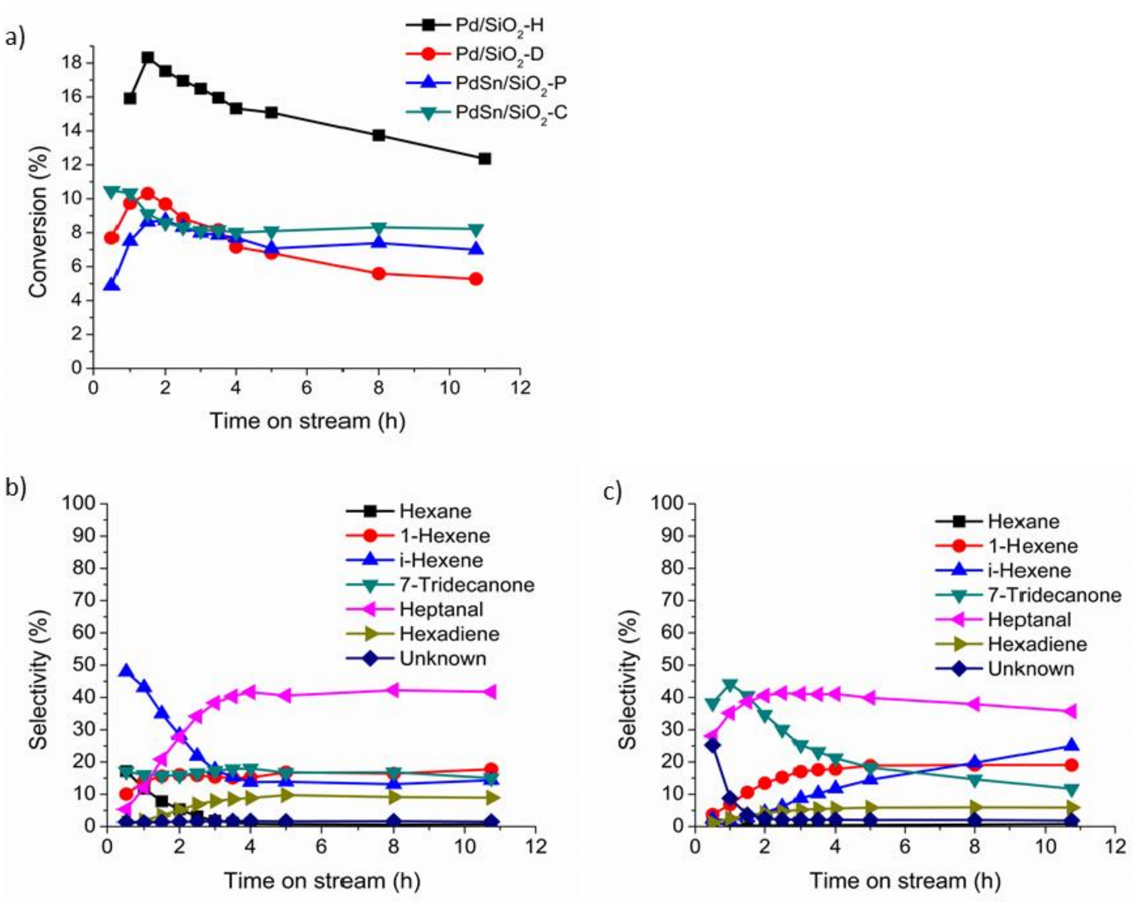

Figure 2.6: a) Conversion of heptanoic acid at 573 K and 0.1 MPa over Pd/SiO_2-H, Pd/SiO_2-D, PdSn/SiO_2-C, and PdSn/SiO_2-P and selectivity to deoxygenation products over b) PdSn/SiO_2-C and c) PdSn/SiO_2-P.

The addition of Sn to Pd may have improved the stability of Pd under the deoxygenation conditions utilized in this study (Fig. 2.6), but the conversions were not consistent between the catalysts. Most importantly, PdSn/SiO_2-C maintained relatively constant 8% conversion of heptanoic acid after the usual initial break-in period. Likewise, the physical mixture PdSn/SiO_2-P exhibited a similar level of activity and stability as the bimetallic PdSn/SiO_2-C catalyst, converting 7% of heptanoic acid after more than 10 h time on stream. An additional test involving a physical mixture of Pd/SiO_2-H and bare silica, containing the same amount of Pd/SiO_2 as PdSn/SiO_2-P and denoted as Pd/SiO_2-D, was evaluated to ensure that the activity and stability of the physical and chemical mixtures of Pd and Sn was the result of Sn and not the low TOF associated with Pd/SiO_2-H. The dilution of Pd/SiO_2-H with bare silica, Pd/SiO_2-D, did not alter the product selectivity associated with the monometallic Pd during conversion of heptanoic acid. As shown in Fig. 2.6a, the deactivation observed for Pd/SiO_2-D, which was tested at the same level of conversion as the Sn-promoted catalysts, confirms the positive effect of Sn on stabilizing the Pd catalysts.

The addition of Sn to a Pd catalyst significantly altered the product distribution observed over monometallic Pd during heptanoic acid conversion. The reaction over PdSn/SiO_2-C (Fig. 2.6b) produced 7-tridecanone, formed via decarboxylative ketonization, as a major product with a selectivity of 38% at 0.5 h time on stream. Heptanal, formed via dehydration, was also produced with a selectivity of 28% at 0.5 h time on stream. The selectivities to 1-hexene, i-hexene, hexadiene, and hexane were 3.7%, 2.3%, 1.2%, and 1.2%, respectively. An unknown product was detected at 0.5 h time on stream with a selectivity of 25%, assuming a similar response factor, but the selectivity decreased to 2% after 2 h. As the time on stream increased to 10.75 h, the selectivity to 7-tridecanone decreased to 12% and the selectivity to heptanal increased to 36%. Roughly equal amounts of 1-hexene and i-hexene were produced with selectivities of 18% and 22 %, respectively, and hexadiene was produced with a selectivity of 5.9%. Interestingly, hexane was not produced in significant quantities after 10.75 h time on stream.

Initially, the physical mixture of PdSn/SiO_2-P (Fig. 2.6c) had a product distribution that was largely characteristic of Pd/SiO_2-catalyzed heptanoic acid deoxygenation. More than 80% of the initial products were consistent with a monometallic Pd/SiO_2 catalyst, with 7-tridecanone making up the balance. The product distribution changed with time on stream until the selectivity patterns of PdSn/SiO_2-P and the PdSn/SiO_2-C catalysts were nearly identical. Heptanal was the primary deoxygenated product over the PdSn/SiO_2-P catalyst with a selectivity of 42%. Internal double bond isomers of hexene comprised 14% of the products while 1-hexene was 18%. The 7-tridecanone product accounted for 15% whereas hexadiene was 9.0% of the products.

The %CO in the gas phase products observed during the conversion of heptanoic acid over the PdSn/SiO_2-C and PdSn/SiO_2-P catalysts is shown in Table 2. The %CO observed over both PdSn catalysts after 10 h on stream did not match well the selectivity to decarbonylation products. The explanation for the lower than anticipated %CO observed is unknown, but it might indicate some conversion of CO to CO_2 via the water-gas-shift reaction.

2.3.4. Effect of Sn proximity to Pd

To further probe the promotional effect of Sn on Pd, heptanoic acid was passed through a reactor containing a Pd/SiO_2-H section and a Sn/SiO_2 section separated by glass wool to ensure there was no direct contact between the supported catalysts. The two different catalyst bed configurations that were tested are illustrated in Fig. 2.7a. The configurations are designated as M_1/M_2 where M_1 was the catalyst at the bottom of the reactor and was the first to contact the heptanoic acid feed.

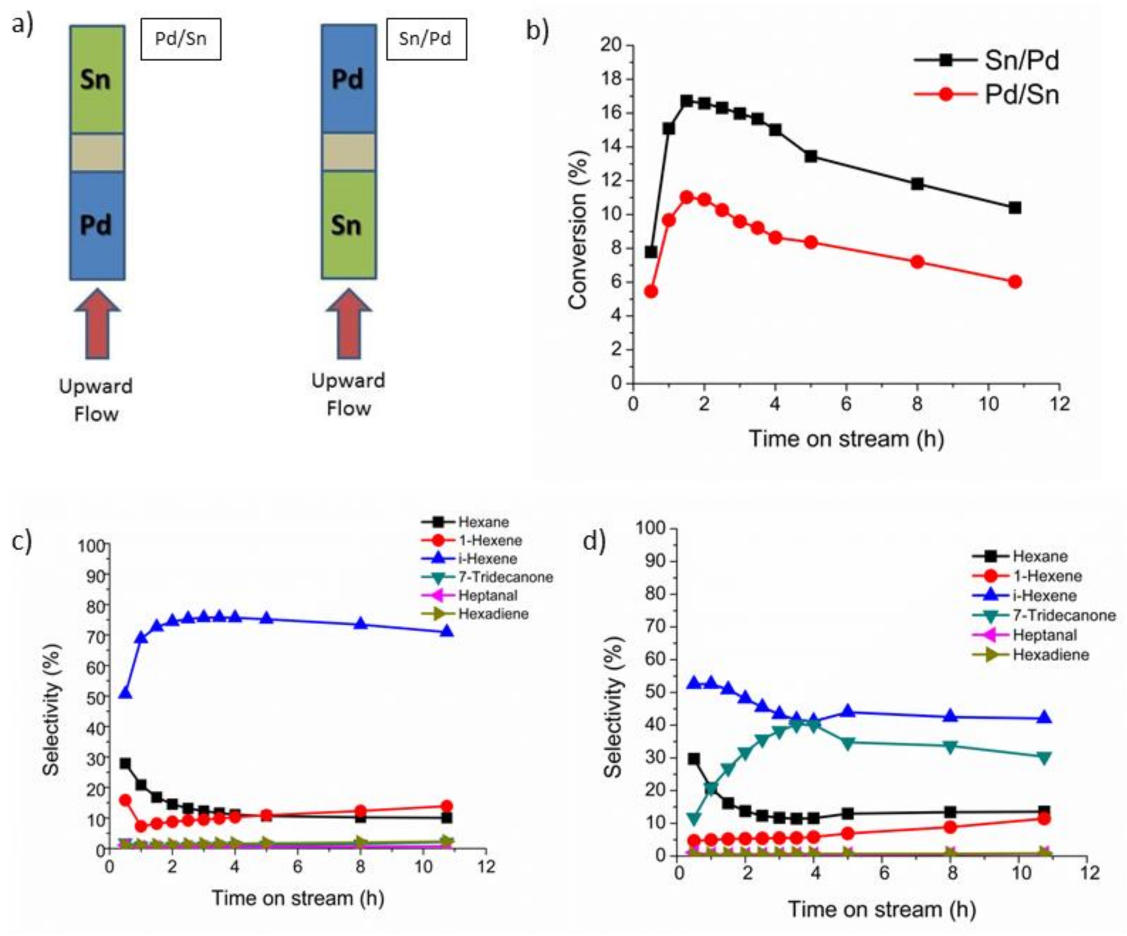

Figure 2.7: a) Configuration of two different catalyst beds in the reactor. Catalyst beds were separated by glass wool. Configurations are designated as M_1/M_2 where M_1 is the first catalyst to contact the reagent. b) Conversion of heptanoic acid at 573 K and 0.1 MPa over separated beds of Pd/SiO_2-H and Sn/SiO_2. c) Product selectivity during reaction over Pd/Sn configuration. d) Product selectivity over Sn/Pd configuration.

The general shape of the conversion curves for both configurations (Fig. 2.7b) is nearly identical to Pd/SiO_2-H (Fig. 2.5a) in which there is an increase in conversion to a maximum followed by deactivation. When heptanoic acid contacted the Pd catalyst first (Pd/Sn), the product distribution reported in Fig. 2.7c resembled that from a reaction catalyzed by a monometallic Pd/SiO_2 catalyst. Most importantly, 7-tridecanone and heptanal were not observed in the reaction products.

The configuration in which the heptanoic acid contacted Sn/SiO_2 prior to Pd/SiO_2 (Sn/Pd) exhibited greater conversion of heptanoic acid compared to the Pd/Sn configuration (Fig. 2.7b). The greater heptanoic acid conversion when it contacts the Sn catalyst first is reflected in a new product distribution (Fig. 2.7d). For the Sn/Pd configuration, 7-tridecanone was formed at a selectivity of 30% after 10.75 h on stream, whereas i-hexene selectivity was only 42%. The selectivity to 1-hexene and hexane remained largely unchanged from those produced over the Pd/Sn configuration at 11 and 14%, respectively.

The percent of CO in the gas phase from each catalyst bed configuration is presented in Table 3. The %CO is largely consistent with the measured amounts of decarbonylation products versus decarboxylative ketonization product.

Table 2.3: The %CO during heptanoic acid conversion at 573 K over two separated catalyst beds

Catalyst configuration	**%CO**	
	TOS = 0.50 h[a]	**TOS = 10.75 h[a]**
Sn/Pd	64	54
Pd/Sn	76	94

[a]TOS represents time on stream

2.3.3. In situ XANES analysis

Figure 2.8 shows the Sn K-edge XANES spectra collected over the course of H_2 TPR for Sn/SiO_2, PdSn/SiO_2-C, and PdSn/SiO_2-P catalysts. Compared to bulk SnO_2[30], which has an E_o at 29.2053 keV, all the unreduced catalyst samples present a very similar spectrum with an identical E_o white line intensity at 298 K, indicating that the oxidation state of Sn in the samples is close to that of SnO_2. During the temperature ramp in flowing 5% H_2/He, the XANES spectrum of Sn/SiO_2 revealed a gradual decrease in the white line intensity up to 508 K (Figs. 8a and 8d), indicating a partial reduction of the supported SnO_2. Addition of Pd, i.e. in PdSn/SiO_2-C, promoted a more extensive reduction of the SnO_2 as evidenced by a more substantial decrease in the white line intensity (Figs. 8b and 8d) and likely caused by hydrogen spill-over[31]. The white line intensities associated with the physically mixed PdSn/SiO_2-P catalyst were positioned between those of Sn/SiO_2 and PdSn/SiO_2-C (Figs. 8c and 8d).

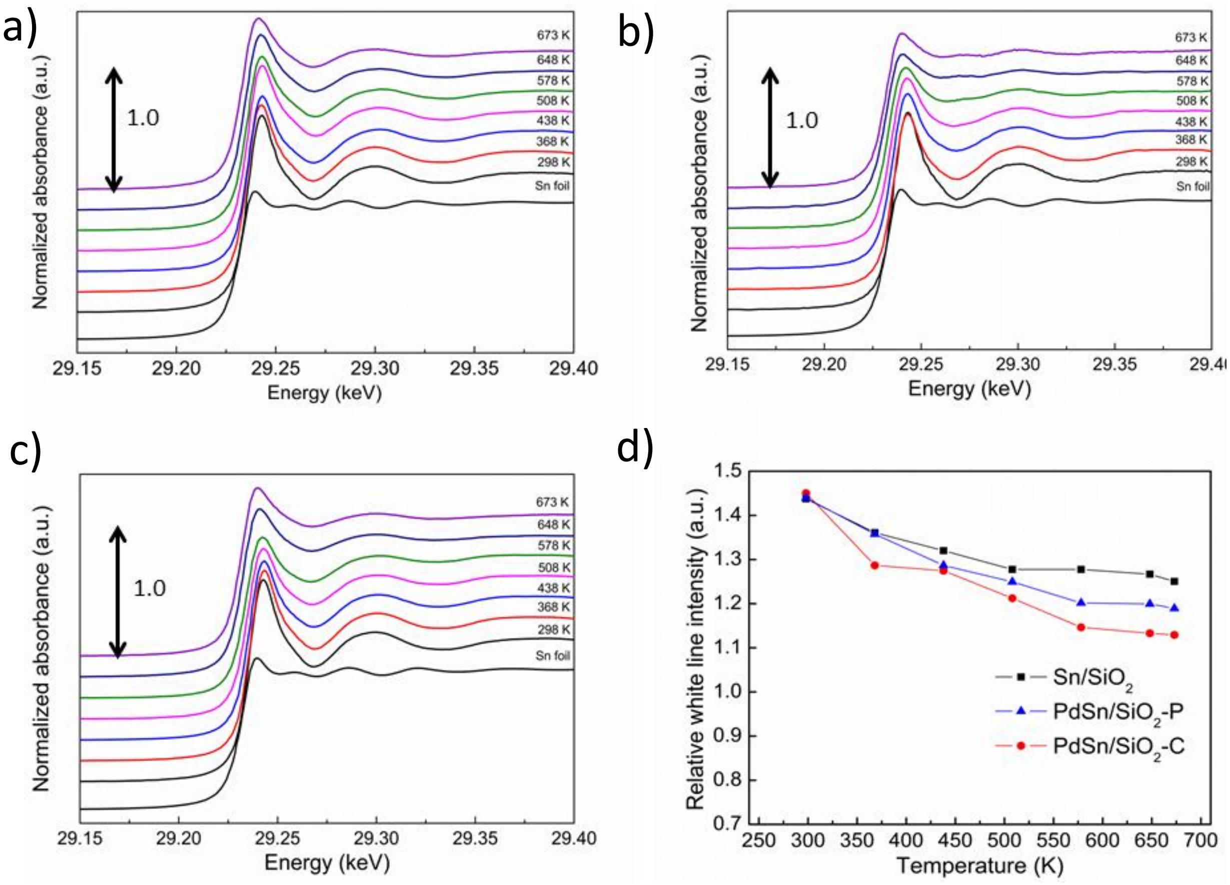

Figure 2.8: In situ Sn K-edge XANES spectra during temperature programmed reduction in 5% H_2 of a) Sn/SiO_2, b) $PdSn/SiO_2$-C, c) $PdSn/SiO_2$-P, and d) comparison of white line intensities. Spectra are offset for clarity.

Figure 2.9 presents the in situ XANES spectra for $PdSn/SiO_2$-C and $PdSn/SiO_2$-P catalysts during butyric acid conversion at 573K. The XANES spectrum of $PdSn/SiO_2$-P in the presence of butyric acid remained unchanged from that of pre-reduced $PdSn/SiO_2$-P, indicating the Sn species present under reaction conditions are likely partially reduced oxides (Fig. 2.9b). The lower intensity of the white line in the XANES spectrum of pre-reduced $PdSn/SiO_2$-C (Fig. 2.9a) compared to $PdSn/SiO_2$-P (Fig 11b) indicates the Sn species is more reduced in $PdSn/SiO_2$-C. The presence of butyric acid, however, slightly increased the white line intensity of $PdSn/SiO_2$-C resulting in an E_o that was very close to that of $PdSn/SiO_2$-P catalyst (Fig. 2.9b). Thus, the chemical state of the Sn in the bimetallic catalyst during reaction is similar to that of the physical mixture.

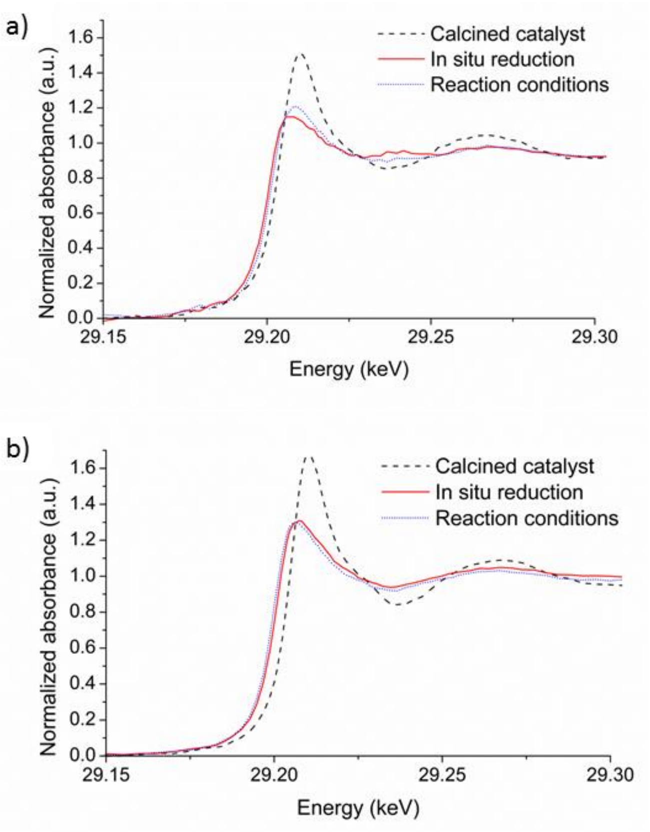

Figure 2.9: In situ Sn K-edge XANES of a) PdSn/SiO_2-C and b) PdSn/SiO_2-P during the conversion of butanoic acid. Spectra for "calcined catalyst" are associated with fresh, unreduced catalyst in flowing N_2. Spectra for "in situ reduction" are associated with the catalyst after reduction in situ at 623 K for 30 min under 100 $cm^3\ min^{-1}$ 5% H_2/He. Spectra for "reaction conditions" are associated with the catalyst at 573 K after 150 min exposure to butanoic acid in N_2.

2.4. Discussion

2.4.1. Structural properties of Pd, Sn, and PdSn catalysts

The lack of XRD features associated with the monometallic catalysts is consistent with the very high dispersion of the Pd/SiO_2 and the Sn/SiO_2 samples. In contrast, XRD features were observed for both the fresh and used PdSn/SiO_2-C catalyst, as illustrated in Fig. 2. The expected Pd (111) peak at 40.1° appeared to be shifted to 39.4° for the fresh and used PdSn/SiO_2-C, which is attributed to the substitution of the larger Sn atom into the Pd lattice. Indeed, the peak at 39.4° is consistent with a

Pd_2Sn alloy.[32] An additional peak at 40.7° is observed in the diffraction pattern of the fresh PdSn/SiO_2-C sample, which could suggest a Pd_3Sn_2 crystal structure, which exhibits a strong diffraction peak at 41.0°. The peak at 40.7° is, however, absent in the diffraction pattern of the used PdSn/SiO_2-C catalyst.

2.4.2. Catalytic performance of Pd, Sn, and PdSn catalysts in deoxygenation of heptanoic acid

2.4.2.1. Activity of Pd catalysts

Deoxygenation of fatty acids over carbon and silica supported noble metal catalysts, including Pd, has been demonstrated to proceed via decarbonylation and decarboxylation (Schemes 1A and 1B).[9,12,13,33] In the present study, the high selectivity to olefin products accompanied by formation of CO indicates that decarbonylation is the primary route of deoxygenation over monometallic Pd/SiO_2 catalysts under the examined reaction conditions. For example, after 10.75 h on stream, hexenes accounted for 84% of the hydrocarbon products and the %CO found in the gas phase product stream was 88% (Table 2). The other major product formed over Pd/SiO_2 was hexane, with a selectivity of 14%, which corresponds well to the %CO_2 value of 12%. Since the product selectivity exhibited by both monometallic Pd catalysts was similar, the Pd particle size between 1-2 nm did not affect the preferred reaction path.

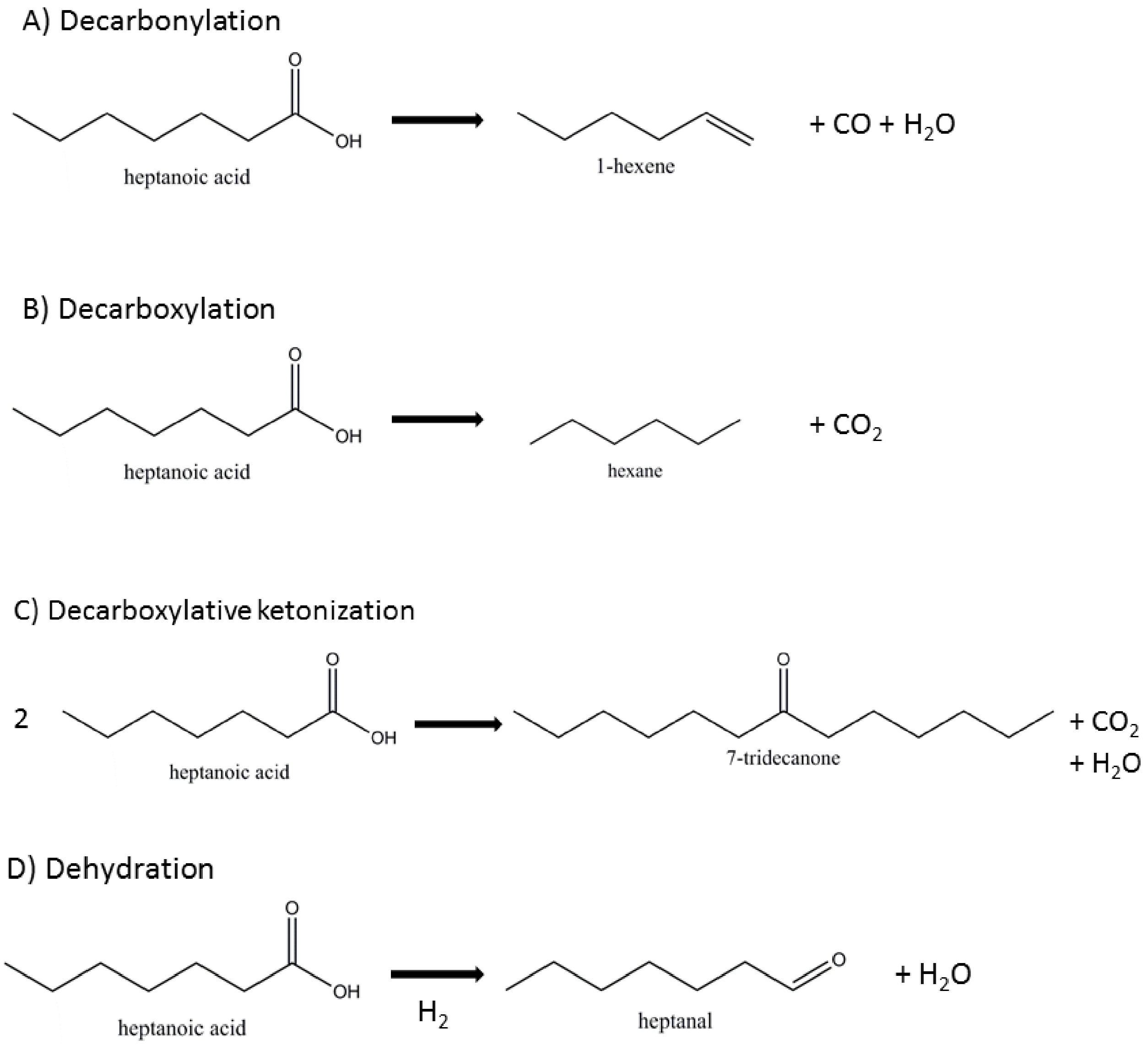

Scheme 2.1: Deoxygenation of heptanoic acid via A) decarbonylation, B) decarboxylation, C) decarboxylative ketonization, and D) dehydration.

In contrast, the particle size influenced the stability and TOF of the Pd/SiO_2 catalyst. Sun et al. observed that larger particles experienced less severe deactivation while converting octanoic acid over Pd/SiO_2 in the presence of dihydrogen.[11] The opposite result was observed in the current work on conversion of heptanoic acid in absence of dihydrogen. Results in Fig. 2.5 clearly show the catalyst with larger Pd particles (Pd/SiO_2-L) deactivating faster than the catalyst with smaller Pd particles (Pd/SiO_2-H). Smaller Pd particles may deactivate slower because they are catalyzing the reaction at a lower TOF.

Lugo-José et al. showed that the TOF for hydrodeoxygenation of propanoic acid over Pd/SiO_2 remains constant when particles are between 3.0-12.4 nm, but decreases by a factor of 2-3 as the Pd particles decreased in size below 3 nm.[34] In the present study, lower TOF of the smaller Pd particles may decrease the rate of self-poisoning which is manifested as more stable activity of the catalyst.

2.4.2.2. Activity of PdSn catalysts

The physical mixture of Pd and Sn, $PdSn/SiO_2$-P, initially exhibited selectivity in heptanoic acid conversion that was characteristic of monometallic Pd/SiO_2-H. The change in product selectivity over the $PdSn/SiO_2$-P from primarily decarbonylation (typical of monometallic Pd) to primarily dehydration, decarbonylation and decarboxylative ketonization suggests the catalyst structure changes under reaction conditions. The EDS analysis of used $PdSn/SiO_2$-P indicates the physical migration of Sn to the silica support particles containing Pd nanoparticles. Treatment in H_2 appears to facilitate some of the Sn migration during the pre-reduction step, as indicated by the decreased H/Pd from H_2 chemisorption results observed for the $PdSn/SiO_2$-P compared to the Pd/SiO_2-H. However, the change in product selectivity with time on stream suggests that a more substantial migration occurred when heptanoic acid flowed over the catalyst.

The migrating Sn species during reaction are hypothesized to be volatile tin carboxylates formed via the reaction between SnO_x species and heptanoic acid.[35] These tin species may decompose on Pd sites located on and within nearby silica particles or simply be deposited on the silica support.[35] The SnO_x species present in the fresh $PdSn/SiO_2$-P catalyst are extremely well dispersed as indicated by the lack of observable particles by HR-TEM. The very low heptanal formation rate observed over the Sn/Pd reactor configuration compared to that observed from the $PdSn/SiO_2$-P and $PdSn/SiO_2$-C catalysts indicates Sn species are incapable of migrating through the glass wool separating the Sn and Pd catalyst beds.

In situ XANES studies suggest that a Pd and Sn bulk alloy is not likely the active phase of the bimetallic system. Migration and redeposition of Sn in the physical mixture PdSn/SiO_2-P forms a partially reduced SnO_x that was responsible for the production of heptanal under reaction conditions. Metal oxide catalysts possessing moderate strength metal-oxygen bonds, including Fe_2O_3 and SnO_2, have been shown to be selective for dehydration of carboxylic acids in the presence of H_2 through a reverse Mars and Van Krevelen mechanism (Scheme 1D).[36–38] Addition of a metal capable of hydrogen spillover, such as Pt, facilitates reduction of the metal oxide, thus promoting aldehyde formation.[38,39] The hydrogen required to form oxygen vacancies may come from the water-gas shift reaction on Pd sites. Such a side reaction is consistent with the observed discrepancy of %CO observed for both PdSn/SiO_2-C and PdSn/SiO_2-P.

The product distribution from heptanoic acid conversion over bimetallic PdSn/SiO_2-C changed throughout the course of the 10.75 h run. The XRD patterns for the fresh and used bimetallic catalyst indicate a change in crystal structure of the metal particles after exposure to reaction conditions. Nevertheless, the in situ XANES study of PdSn/SiO_2-C during butyric acid conversion confirms partially reduced SnO_x species are similar to those present on the physical mixture. Carboxylic acids containing two α-hydrogens, such as heptanoic acid, will undergo decarboxylative ketonization on metal oxide surfaces that do not contain a prevalence of oxygen vacancies.[37,38] Evidently, the initial state of PdSn/SiO_2-C favors production of 7-tridecanone (Fig. 2.6b) which decreases at later times on stream.

2.4.2.3. Stability of PdSn catalysts

The SnO_x species surrounding Pd sites in both physically-mixed and chemically-mixed PdSn/SiO_2 catalysts appear to promote the stability of the catalyst. Prior work demonstrated SnO_x can supply oxygen-containing species that oxidatively remove CH_3CO and CO adsorbed on adjacent noble metal sites.[40,41] In addition, Pd-promoted SnO_x/SiO_2 has been reported to exhibit higher rates of CO oxidation compared to unpromoted SnO_x/SiO_2.[17] Thus, removal of product CO and unreacted heptanoic acid might be facilitated by the presence of Sn. Although an alloy phase was detected in the chemically mixed PdSn/SiO_2-C, we suspect it resides in the few large bimetallic particles that would likely be irrelevant in the reaction.

2.5. Conclusion

The reactivity of silica-supported Pd, Sn, and PdSn bimetallic catalysts was evaluated in the conversion of heptanoic acid. Whereas monometallic Pd converted heptanoic acid primarily through decarbonylation, addition of Sn altered the reaction network to include dehydration and decarboxylative ketonization. In addition to altering the product distribution, addition of Sn to Pd improved the stability of the catalyst. Physically-mixed PdSn/SiO_2-P and chemically-mixed PdSn/SiO_2-C catalysts exhibited similar rates and selectivites after long times on stream, suggesting the final state of the catalyst is similar in both cases. Characterization of a used catalyst revealed a physical migration of Sn to Pd during reaction over the physical mixture. Analysis of Sn K-edge XANES suggests that the chemical state of Sn on the PdSn catalysts is a SnO_x species that forms under reaction conditions.

2.6. Acknowledgements

This material was based upon the work supported by the National Science Foundation under award number EEC-0813570. The XANES studies were funded by the Korea Institute of Energy Technology Evaluation and Planning (KETEP-20154030200830). The authors would like to acknowledge Dr. Helge Heinrich in the Department of Materials Science and Engineering at the University of Virginia as well as Ki-Duk Kim at Dankook University, South Korea. Helpful discussions with Dr. Derek Falcone, Zachary Young, and James Kammert are also acknowledged.

2.7. References for Chapter 2

1. Keim, W. Petrochemicals: Raw material change from fossil to biomass? *Pet. Chem.* **50,** 298–304 (2010).

2. Alonso, D. M., Wettstein, S. G. & Dumesic, J. A. Bimetallic catalysts for upgrading of biomass to fuels and chemicals. *Chem. Soc. Rev.* **41,** 8075–98 (2012).

3. Swinnen, J. & Tollens, E. Bulk chemicals from biomass in the EC: feasibility and potential outlets. *Bioresour. Technol.* **36,** 277–291 (1991).

4. Snåre, M., Kubičková, I., Mäki-Arvela, P., Eränen, K. & Murzin, D. Y. Heterogeneous catalytic deoxygenation of stearic acid for production of biodiesel. *Ind. Eng. Chem. Res.* 5708–5715 (2006). at <http://pubs.acs.org/doi/abs/10.1021/ie060334i>

5. Snåre, M. *et al.* Catalytic deoxygenation of unsaturated renewable feedstocks for production of diesel fuel hydrocarbons. *Fuel* **87,** 933–945 (2008).

6. Immer, J. G., Kelly, M. J. & Lamb, H. H. Catalytic reaction pathways in liquid-phase deoxygenation of C18 free fatty acids. *Appl. Catal. A Gen.* **375,** 134–139 (2010).

7. Pestman, R., Duijne, A. van, Pieterse, J. A. Z. & Ponec, V. The formation of ketones and aldehydes from carboxylic acids , structure-activity relationship for two competitive reactions. *J. Mol. Catal. A Chem.* **1169,** (1995).

8. Lestari, S. *et al.* Diesel-like Hydrocarbons from Catalytic Deoxygenation of Stearic Acid over Supported Pd Nanoparticles on SBA-15 Catalysts. *Catal. Letters* **134,** 250–257 (2009).

9. Mäki-Arvela, P., Snåre, M., Eränen, K., Myllyoja, J. & Murzin, D. Y. Continuous decarboxylation of lauric acid over Pd/C catalyst. *Fuel* **87,** 3543–3549 (2008).

10. Ping, E. W. *et al.* On the nature of the deactivation of supported palladium nanoparticle catalysts in the decarboxylation of fatty acids. *Appl. Catal. A Gen.* **396,** 85–90 (2011).

11. Sun, K., Wilson, A. R., Thompson, S. T. & Lamb, H. H. Catalytic Deoxygenation of Octanoic Acid over Supported Palladium: Effects of Particle Size and Alloying with Gold. *ACS Catal.* **5,** 1939–1948 (2015).

12. Lopez-Ruiz, J. A. & Davis, R. J. Decarbonylation of heptanoic acid over carbon-supported platinum nanoparticles. *Green Chem.* **16,** 683 (2014).

13. Lopez-Ruiz, J. A., Pham, H. N., Datye, A. K. & Davis, R. J. Reactivity and stability of supported Pd nanoparticles during the liquid-phase and gas-phase decarbonylation of heptanoic acid. *Appl. Catal. A Gen.* 1–13 (2015). doi:10.1016/j.apcata.2015.01.032

14. López-Suárez, F. E. *et al.* Platinum–tin/carbon catalysts for ethanol oxidation: Influence of Sn content on the electroactivity and structural characteristics. *Int. J. Hydrogen Energy* **40,** 12674–12686 (2015).

15. Rodríguez, D., Sánchez, J. & Arteaga, G. Effect of tin and potassium addition on the nature of platinum supported on silica. *J. Mol. Catal. A Chem.* **228,** 309–317 (2005).

16. Nishiyama, S., Kubota, T. & Kimura, K. Unique hydrogenation activity of supported tin catalyst: Selective hydrogenation catalyst for unsaturated aldehydes. *J. Mol. Catal. A* **1169,** (1997).

17. Bond, G. C., Molloy, R. & Fuller, M. J. Oxidation of Carbon Monoxide over Palladium-Tin (IV) Oxide Catalysts : An Example of Spillover Catalysis. *J. Chem. Soc. Chem. Commun.* 2–3 (1975).

18. Tshabalala, T. E., Coville, N. J. & Scurrell, M. S. Dehydroaromatization of methane over doped Pt/Mo/H-ZSM-5 zeolite catalysts: The promotional effect of tin. *Appl. Catal. A Gen.* **485,** 238–244 (2014).

19. Huber, G. W., Shabaker, J. W. & Dumesic, J. A. Raney Ni-Sn catalyst for H2 production from biomass-derived hydrocarbons. *Science* **300,** 2075–7 (2003).

20. Yeh, T. M., Hockstad, R. L., Linic, S. & Savage, P. E. Hydrothermal decarboxylation of unsaturated fatty acids over PtSn x = C catalysts. *Fuel* **156,** 219–224 (2015).

21. Alcala, R., Shabaker, J. W., Huber, G. W., Sanchez-Castillo, M. A. & Dumesic, J. A. Experimental and DFT Studies of the Conversion of Ethanol and Acetic Acid on. *J. Phys. Chem. B* **109,** 2074–2085 (2005).

22. Burch, R. & Garla, L. C. Platinum-tin reforming catalysts: 2. Activity and selectivity in hydrocarbon reactions. *J. Catal.* **71,** 360–372 (1981).

23. Chiappero, M., Do, P. T. M., Crossley, S., Lobban, L. L. & Resasco, D. E. Direct conversion of triglycerides to olefins and paraffins over noble metal supported catalysts. *Fuel* **90,** 1155–1165 (2011).

24. Lam, Y. M. & Boudart, M. Preparation of small Au-Pd particles on silica. *J. Catal.* **50,** 530–540 (1977).

25. Nakatsuji, H., Hada, M. & Yonezawa, T. Theoretical study on the chemisorption of a hydrogen molecule on palladium. *J. Am. Chem. Soc.* **19,** 1902–1912 (1987).

26. Pham, H. N., Sattler, J. J. H. B., Weckhuysen, B. M. & Datye, A. K. The Role of Sn in the Regeneration of Pt/γ-Al2O3 Light Alkane Dehydrogenation Catalysts. *ACS Catal.* **6,** 2257–2264 (2016).

27. Davis, R. J. & Boudart, M. Structure of Supported PdAu Clusters Determined by X-ray Absorption Spectroscopy. *J. Phys. Chem.* **98,** 5471–5477 (1994).

28. Cho, H. & Regalbuto, J. R. The rational synthesis of Pt-Pd bimetallic catalysts by electrostatic adsorption. *Catal. Today* **246,** 143–153 (2015).

29. Lambert, S. *et al.* Synthesis of very highly dispersed platinum catalysts supported on carbon xerogels by the strong electrostatic adsorption method. *J. Catal.* **261,** 23–33 (2009).

30. Protesescu, L. *et al.* Unraveling the Core-Shell Structure of Ligand-Capped Sn/SnO x Nanoparticles by Surface-Enhanced Nuclear Magnetic Resonance , Mössbauer , and X-ray Absorption Spectroscopies. *ACS Nano* **8,** 2639–2648 (2014).

31. Gavagnin, R., Biasetto, L., Pinna, F. & Strukul, G. Nitrate removal in drinking waters : the effect of tin oxides in the catalytic hydrogenation of nitrate by Pd / SnO 2 catalysts. *Appl. Catal. B Environ.* **38,** 91–99 (2002).

32. Esmaeili, E., Rashidi, A. M., Khodadadi, A. A., Mortazavi, Y. & Rashidzadeh, M. Palladium–Tin nanocatalysts in high concentration acetylene hydrogenation: A novel deactivation mechanism. *Fuel Process. Technol.* **120,** 113–122 (2014).

33. Lugo-José, Y. K., Monnier, J. R. & Williams, C. T. Gas-phase, catalytic hydrodeoxygenation of propanoic acid, over supported group VIII noble metals: Metal and support effects. *Appl. Catal. A Gen.* **469,** 410–418 (2014).

34. Lugo-José, Y. K., Monnier, J. R., Heyden, A. & Williams, C. T. Hydrodeoxygenation of propanoic acid over silica-supported palladium: effect of metal particle size. *Catal. Sci. Technol.* **4,** 3909–3916 (2014).

35. Andor, J. A., Berkesi, O., Dreveni, I. & Varga, E. Physical and Chemical Modification of Zinc Carboxylate-containing Lubricants by Molecular Structure Changes. *Lubr. Sci.* **11-2,** (1999).

36. Lange, M. W. de, Ommen, J. G. van & Lefferts, L. Deoxygenation of benzoic acid on metal oxides 1 . The selective pathway to benzaldehyde. **220,** 41–49 (2001).

37. Yokoyama, T. & Yamagata, N. Hydrogenation of carboxylic acids to the corresponding aldehydes. *Appl. Catal. A Gen.* **221,** 227–239 (2001).

38. Pestman, R., Koster, R. M., Pieterse, J. A. Z. & Ponec, V. Reactions of Carboxylic Acids on Oxides 1 . Selective Hydrogenation of Acetic Acid to Acetaldehyde. *J. Catal.* **168,** 255–264 (1997).

39. Pritchard, J., Filonenko, G. A., van Putten, R., Hensen, E. J. M. & Pidko, E. A. Heterogeneous and homogeneous catalysis for the hydrogenation of carboxylic acid derivatives: history, advances and future directions. *Chem. Soc. Rev.* **44,** 3808–3833 (2015).

40. Zignani, S. C., Gonzalez, E. R., Baglio, V., Siracusano, S. & Aricò, A. S. Investigation of a Pt 3 Sn / C Electro-Catalyst in a Direct Ethanol Fuel Cell Operating at Low Temperatures for Portable Applications. *Int. J. Electrochem. Sci.* **7,** 3155–3166 (2012).

41. Lu, H., Fan, Y., Huang, P. & Xu, D. SnO2 nanospheres supported Pd catalyst with enhanced performance for formic acid oxidation. *J. Power Sources* **215,** 48–52 (2012).

Chapter 3:

Propane Dehydrogenation over Supported Pt-Sn Nanoparticles*

**This section is adapted from a manuscript that was submitted to the Journal of Catalysis in June 2018.*

Abstract

The influences of support (SiO_2 versus Al_2O_3), synthesis method (impregnation versus colloidal synthesis) and Sn loading on the performance of Sn-promoted Pt nanoparticles for propane dehydrogenation to propene at 773 K were explored. Catalysts were characterized extensively by X-ray diffraction, temperature-programmed reduction/oxidation, chemisorption, electron microscopy, X-ray photoelectron spectroscopy, and DRIFTS of adsorbed CO. Catalyst stability and selectivity to propene were correlated with extent of Pt-Sn interactions within the nanoparticles, which was favored at high Sn loading, and when the particles were supported on a weakly interacting carrier such as silica. However, oxidative regeneration irreversibly deactivated bimetallic nanoparticles on silica relative to those on alumina. The extended performance of Sn-promoted Pt catalysts is an optimization of the Pt-Sn interactions with the ability to oxidatively redisperse the metals during regeneration.

3.1. Introduction

Improvements to fracking technology have increased the availability of natural gas and natural gas liquids thus decreasing the cost of chemicals production.[1] The abundant supply of light hydrocarbons has motivated the development of processes for on-purpose dehydrogenation of light alkanes to alkenes that are key building-block molecules in the plastics and specialty chemicals industries.[1,2] Several processes that have been commercialized utilize chromium-based catalysts, which suffer from environmental concerns,[2,3] or platinum-based catalysts.[2] Supported Pt catalysts in particular are highly active for the dehydrogenation of light alkanes, including the conversion of propane to propene. Unfortunately, Pt is also known to catalyze hydrocarbon hydrogenolysis and coke formation at the conditions required for alkane dehydrogenation.[2,4–8] Platinum is therefore typically promoted by a second metal such as Ga[9], Cu[10], Zn[11,12], and Sn[2,5].

Tin is a well-known promoter of Pt group metals that has been studied in a wide variety of reactions.[13–27] For example, the addition of Sn to Pt propane dehydrogenation catalysts increased selectivity to propene while decreasing catalyst deactivation due to coke formation.[5,7,8,28–30] The promotional role of Sn on Pt catalysts has been attributed to both electronic and geometric effects.[2,5,31–34] Electronic promotion is proposed to occur by the donation of electronic charge from Sn to Pt, which decreases the heat of ethene[32,34] and propene[31] adsorption as well as increases the barrier for dissociative adsorption of light alkanes,[31] which is postulated to be the rate determining step for the dehydrogenation of propane on Pt.[2,5,35–37] As an increased barrier of the dissociative chemisorption of propane will slow the rate of propane dehydrogenation, there is a trade-off between catalytic activity and stability of Pt-Sn alloys with varying Sn content. Density-functional theory was used to determine that the binding strength of 1-propyl, a key surface intermediate during the dehydrogenation of propane, decreases with increasing Sn-alloy content in the following series: Pt(111) > Pt_3Sn > Pt_2Sn >

$PtSn_2$.[31] The decrease in binding energy of dehydrogenated species on the Pt surface lowers the steady state coverage of these unsaturated molecules, inhibiting deep dehydrogenation and coke formation.

The geometric effect of adding Sn to Pt results from the dilution of Pt ensembles. Large ensembles of Pt surface atoms are required for some undesired side reactions including deep dehydrogenation, which leads to coke formation, and hydrogenolysis. Thus, surface dilution of Pt ensembles is thought to enhance selectivity to propene during propane dehydrogenation while decreasing coke formation.[2,4,28–30,32,37] The presence of Sn atoms has also been suggested to improve the regeneration of deactivated Pt/Al_2O_3 by acting as nucleation sites for mobilized Pt atoms during oxidative treatments.[4,30,38,39]

The mode and extent of Sn promotion of Pt depends on many factors including synthesis method and catalyst support. For example, co-impregnation of an acidic solution containing $SnCl_2$ and H_2PtCl_6 forms the bimetallic $PtCl_2(SnCl_3)_2^{2-}$ complex that results in a high degree of Pt-Sn interaction during the post-synthesis thermal treatment.[5,30,40] Direct reduction of Pt-Sn/SiO_2 prepared by incipient wetness impregnation was more active than analogous samples treated in inert gas or air prior to reduction.[41] Additionally, the composition of the catalyst support influences the interactions between Pt and Sn. A support such as SiO_2, which interacts weakly with the metals, allows for a greater extent of metal interaction with themselves, resulting in a higher degree of alloy formation.[2,5,42,43] On the contrary, a support such as Al_2O_3, which interacts strongly with Sn, stabilizes the promoter in an oxidized state.[2,5,8,44] Alloy formation has only been observed on Al_2O_3-supported PtSn catalysts with high Sn loadings.[44,45] The Sn is typically found near the Pt-Al_2O_3 interface or on Pt defect sites as determined by FTIR spectroscopy utilizing CO as a probe molecule.[46]

Advanced synthesis techniques have been employed recently to produce a narrow size distribution of nanoparticles as well as specific Pt:Sn ratios within those nanoparticles. Particle size is known to influence catalyst stability and product selectivity for monometallic Pt catalysts[47,48] and bimetallic PtSn catalysts.[32] Step sites on monometallic Pt catalysts, which dominate the activity on smaller particles,[48] bind propene more strongly and can lead to the formation of deep dehydrogenation products during propane dehydrogenation.[31] A narrow particle size distribution for the monometallic and bimetallic catalysts can be achieved using colloidal synthesis techniques.[23,32,49–52] In addition, manipulation of nanoparticle composition will influence the alloy phases that are produced. For example, increasing the atomic Sn content from 97:3 (Pt:Sn) to 75:25 has been show to increase the content of Pt_3Sn alloy as evidenced by powder X-ray diffraction.[52]

In the present study, the dehydrogenation of propane to propene was investigated over Pt and PtSn catalysts. In particular, the influence of the catalyst support (SiO_2 versus Al_2O_3) and the Sn loading on the catalyst stability and selectivity were investigated, with and without co-fed H_2. The performance of colloidal PtSn nanoparticles synthesized using a modified polyol method is compared to those synthesized by incipient wetness impregnation. The influence of Sn and the support on the regeneration of catalysts was also explored.

3.2. Experimental methods

3.2.1. Catalyst synthesis

Nominal 1 wt% Pt/SiO_2, denoted as 1Pt/SiO_2, was synthesized via incipient wetness impregnation (IWI) using $H_2PtCl_6 \bullet 6H_2O$ (>37.5% Pt, Sigma-Aldrich) dissolved in distilled, deionized (DI) water. The catalyst was supported on Davisil 636 SiO_2 (Sigma-Aldrich). Following impregnation, the catalyst was dried overnight in air at 393 K and treated in 100 $cm^3\ min^{-1}$ H_2 (99.999%, GTS-Welco) at 923 K for 3 h following a 1 K min^{-1} ramp rate. Alumina-supported nominal 1wt% Pt/Al_2O_3, denoted as 1Pt/Al_2O_3, was synthesized by IWI utilizing Al_2O_3 with a mixed phase (pore size 58Å, ~150 mesh, Sigma-

Aldrich 267740) and $H_2PtCl_6•6H_2O$. Following impregnation, the catalyst was dried overnight in air at 393 K and treated in 100 cm^3 min^{-1} air (medical grade, GTS-Welco) at 773 K for 3 h following a 1 K min^{-1} ramp rate. After cooling to room temperature, the $1Pt/Al_2O_3$ catalyst was reduced in 100 cm^3 min^{-1} H_2 at 923 K for 3 h following a 1 K min^{-1} ramp rate.

Bimetallic $Pt-Sn/SiO_2$ catalysts were synthesized by IWI using $H_2PtCl_6•6H_2O$ and $SnCl_2$ (98%, Sigma-Aldrich) precursors and Davisil 636 SiO_2 (Sigma-Aldrich) as the catalyst support. The Pt and Sn precursors were co-impregnated in an HCl (ACS reagent, 37%, Sigma-Aldrich) solution diluted in DI water with an HCl to $SnCl_2$ molar ratio of 3 to 1. The catalysts were dried overnight in air at 393 K and then treated in 100 cm^3 min^{-1} H_2 at 923 K for 3 h following a 1 K min^{-1} ramp rate. The bimetallic catalysts had a nominal loading of Pt of 1 wt% and a nominal loading of Sn ranging from 0.2 wt% to 2.4 wt%. These catalysts were denoted as $1PtxSn/SiO_2$ where x is the nominal Sn weight loading.

Bimetallic $Pt-Sn/Al_2O_3$ catalysts were synthesized by IWI using $H_2PtCl_6•6H_2O$ and $SnCl_2$ precursors and the mixed phase Al_2O_3 support. The Pt and Sn precursors were co-impregnated in an HCl solution utilizing the same dilution and $HCl:SnCl_2$ molar ratio as the bimetallic SiO_2-supported catalysts. The bimetallic samples were subsequently treated in air and H_2 following the same protocol used to prepare monometallic Pt/Al_2O_3. The bimetallic alumina-supported catalysts were denoted as $1PtxSn/Al_2O_3$ where x is the nominal Sn weight percent.

A bimetallic nominal 1 wt% Pt and 0.6 wt% Sn supported on SiO_2 catalyst was also synthesized by a modified polyol method.[49] In summary, 0.18 g NaOH (reagent grade ≥98%, Sigma-Aldrich) was dissolved in 50 cm^3 ethylene glycol (99.8%, anhydrous, Sigma-Aldrich) at 323 K. The solution was cooled to room temperature followed by the addition of 0.053 g $PtCl_4$ (99.99%, Sigma-Aldrich) and 0.030 g $SnCl_2$. The metal precursor solution was stirred for 1 h at room temperature before 2.952 g of SiO_2 was added under stirring conditions. The slurry was then rapidly heated to 463 K where it was held for 2 h and stirred under reflux. The mixture was cooled to room temperature, thoroughly washed with DI water, and dried under vacuum. The catalyst was dried overnight in air at 393 K. Lastly, the catalyst was treated in 100 cm^3 min^{-1} air (medical grade, GTS-Welco) at 723 K for 1 h to remove any remaining ethylene glycol, cooled to room temperature, and then treated in 100 cm^3 min^{-1} H_2 (99.999%, GTS-Welco) at 773 K for 3 h. All ramp rates were 1 K min^{-1}. This polyol-synthesized bimetallic catalyst was denoted as 1Pt0.6Sn/SiO_2-P.

A second bimetallic catalyst synthesized by the polyol method composed of 1 wt% Pt and 0.6 wt% Sn supported on Al_2O_3 was also prepared.[49] For this sample, 0.30 g NaOH was dissolved in 50 cm^3 ethylene glycol (99.8%, anhydrous, Sigma-Aldrich) at 323 K. The higher concentration of NaOH, relative to that used for 1Pt0.6Sn/SiO_2-P synthesis, was utilized to ensure that the solution pH was above the point of zero charge for Al_2O_3. The solution was then cooled to room temperature followed by the addition of 0.053 g $PtCl_4$ and 0.030 g $SnCl_2$. The solution containing the metal precursors was stirred for 1 h at room temperature before 2.952 g of Al_2O_3 was added under stirring conditions. The slurry was then rapidly heated to 463 K and stirred for 2 h under reflux. The recovered solid was treated the same way as the 1Pt0.6Sn/SiO_2-P catalyst. The polyol-synthesized Al_2O_3-supported bimetallic catalyst was denoted as 1Pt0.6Sn/Al_2O_3-P.

Catalyst compositions of some of the samples were analyzed using inductively coupled plasma optical emission spectroscopy (ICP-OES) provided by Galbraith Laboratories, Inc. (2323 Sycamore Drive, Knoxville, TN 37921). Sample calculations for Weisz-Prater criterion can be found in the Supplemental Materials.

3.2.2. Catalyst characterization

3.2.2.1. Chemisorption of H_2 and CO

The number of exposed Pt surface sites was estimated by H_2 and CO chemisorption using a Micromeritics ASAP 2020 automated adsorption analyzer. All IWI-synthesized catalysts were heated ex situ at 923 K (or 773 K for polyol-synthesized catalysts), in flowing H_2 for 3 h prior to chemisorption analysis. The catalysts were heated in situ at 1 K min^{-1} to 723 K under H_2 (99.999%, GTS-Welco) and held at temperature for 2 h. The samples were then cooled to 473 K and evacuated for 2 h before being cooled to 308 K for H_2 chemisorption. This sequence was repeated for CO chemisorption using the same sample without exposure to air. The amount of exposed Pt was calculated using the total amount of adsorbed H_2 or CO extrapolated to zero pressure. Nominal weight loadings were used for the calculations of H/Pt and CO/Pt unless otherwise noted.

3.2.2.2. X-Ray diffraction

X-Ray diffraction patterns of the powder samples were measured using a PANalytical X'Pert Pro equipped with monochromatic Cu Kα-radiation (λ=1.54056Å) utilizing a scan rate of 0.0088 ° s^{-1} from 15° to 90°.

3.2.2.3. Temperature-programmed reduction

The Al_2O_3-supported Pt and Pt-Sn catalysts were probed with temperature programmed reduction (TPR) using a Micromeritics Autochem II 2920 equipped with a thermal conductivity detector (TCD). Approximately 100 mg of catalyst that was freshly calcined in flowing air from the synthesis procedure (prior to reduction in H_2) was heated at a rate of 5 K min^{-1} in 5% H_2/Ar (GTS-Welco) to 1073 K.

3.2.2.4. Transmission electron microscopy

Samples analyzed by scanning transmission electron microscopy (STEM) were prepared by dispersing the powders in cyclohexane (99.5%, anhydrous, Sigma-Aldrich) and sonicating for 1 h before mounting on Cu-supported holey carbon grids. The catalyst samples were imaged using an FEI Titan 80-300 operating at 300 kV.

3.2.2.5. X-Ray photoelectron spectroscopy

X-Ray photoelectron spectroscopy (XPS) was performed using a Phi VersaProbe III with a monochromatic Al Kα X-ray source (1486.6 eV) and a hemispherical analyzer. A magnetic lens with a 100 µm spot size was utilized with a pass energy of 26 eV for region scans at 50 ms per step. Charge compensation was utilized with a low energy external Ar ion flood gun and an internal electron flood gun at 1 eV. Spectra were deconvoluted utilizing CasaXPS. The Si $2p_{3/2}$ peak for SiO_2 (103.5 eV) was used to reference the peak positions. Peak areas were calculated after subtracting the background and utilizing curve fitting parameters for Pt and Sn reported previously.[53]

3.2.2.6. Diffuse reflectance infrared Fourier transform spectroscopy

A Bruker BioRad FTS-60A FTIR spectrometer equipped with a Harrick praying mantis diffuse reflectance cell with KBr windows was used for the diffuse reflectance infrared Fourier transform spectroscopy (DRIFTS) experiments. The spectra are reported in Kubelka-Munk units and were averaged over 150 scans collected at 1 cm^{-1} resolution. Alumina-supported catalysts were used as prepared. Silica-supported catalysts were diluted to 50 wt% in Al_2O_3, which was previously calcined at 773 K, and lightly ground with a mortar and pestle. Samples were loaded into the diffuse reflectance cell and treated in 20 $cm^3\ min^{-1}$ H_2 (passed through an OMI-2 purifier) at 773 K for 1 h following a 2 K min^{-1} ramp rate. Catalysts were then cooled to 303 K and purged for 30 min with 30 $cm^3\ min^{-1}$ He (99.999%, GTS-Welco, passed through an OMI-2 purifier). Carbon monoxide (99.9%, GTS-Welco) was passed through a SiO_2 trap maintained at 195 K to remove carbonyls. The CO was diluted to approximately 1% in He to give a total flow rate of approximately 100 cm^3 min^{-1}. The catalyst sample was exposed to the dilute CO for 30 min, and was subsequently purged with He. Spectra were collected starting 15 min after the beginning of the He purge and were recorded every 15 min thereafter.

3.2.2.7. Catalytic dehydrogenation of propane

The catalytic dehydrogenation of propane to propene was performed in a stainless steel continuous flow reactor in a downward configuration with a 0.64 cm OD. A stainless steel pre-heater section was located above the reactor. The catalyst bed was supported by quartz wool. For reactions targeting 2% initial conversion of propane and the effect of co-fed H_2, catalysts were diluted with SiO_2 to give a total bed loading of about 300 mg. For reactions in which deactivation and regeneration of the catalyst were studied, the catalysts were used without diluent. The undiluted catalyst allowed for the recovery of used catalyst material for additional characterization. Once loaded, catalyst was heated at 1 K min^{-1} in 100 cm^3 min^{-1} H_2 (99.999%, GTS-Welco) and held at 923 K for 3 h for IWI-synthesized catalysts and at 773 K for polyol-synthesized catalysts. The reactor was then cooled to 773 K and purged with 60 cm^3 min^{-1} N_2 (99.999%, GTS-Welco) before initiating the flow of the propane feed mixture. The feed consisted of 25% propane and 75% N_2 with total flow rate varying from 40 cm^3 min^{-1} to 200 cm^3 min^{-1}. Experiments utilizing co-fed H_2 had a molar ratio of 1:2:5 for H_2:propane: N_2. An Agilent 7890A gas chromatograph equipped with a flame ionization detector and an HP-PLOT/Q column was used to analyze the reaction products.

The influence of regeneration conditions was investigated by utilizing a synthetic air blend consisting of 20.7% O_2 with balance He (GTS-Welco) to mimic the oxidation treatment required to remove coke. Typically, catalysts were first used for propane dehydrogenation for 24 h. The reactor was subsequently purged with 60 cm^3 min^{-1} N_2 (99.999%, GTS-Welco) for 1 h at reaction temperature. The coke deposits were removed by treatment in 80 cm^3 min^{-1} of synthetic air at 773 K for 1 h and then purged for 1 h with 60 cm^3 min^{-1} N_2. Finally, the catalysts were re-reduced in situ at 773 K in 100 cm^3 min^{-1} in flowing H_2 for 2 h and purged for 1 h with 60 cm^3 min^{-1} N_2 prior to resuming the flow of the reaction gas mixture.

Equilibrium conversion at 773 K was calculated to be 33% for a 1:3 propane:N_2 feed ratio and 19% for a 1:2:5 H_2:propane:N_2 feed ratio. The Wiesz-Prater criterion was used to verify the absence of mass transfer limitations.

3.2.2.8. Temperature-programmed oxidation of coked samples

The weight percent of coke formed on each catalyst was measured using a TA Instruments SDT Q600 thermogravimetric analyzer (TGA). Approximately 4-10 mg of used catalyst sample was placed in a small Al_2O_3 cup that was heated in 20.7% O_2/He (GTS-Welco) to 1073 K at a rate of 10 K min^{-1} for Al_2O_3 catalysts and 20 K min^{-1} for SiO_2 catalysts. Results from the Al_2O_3 catalyst support were used to subtract background water loss from Al_2O_3-supported catalysts.

3.2.3. Calculation of rate, selectivity, and deactivation

The typical products observed during propane dehydrogenation reactions included methane, ethane, ethene, and propene. The conversion of propane was calculated on a carbon basis as shown in equation 1:

$$Conversion = X = \frac{\sum n_i F_i}{\sum n_i F_i + 3F_{propane}} \qquad (1)$$

where n_i is the number of carbons in product i flowing at molar flow rate of F_i. The selectivity to propene was defined on a carbon basis as shown in equation 2:

$$Selectivity = \frac{3F_{propene}}{\sum n_i F_i} \qquad (2)$$

The rate of catalytic conversion of propane was defined as the conversion of propane (equation 1) multiplied by the molar flow rate of propane ($F_{propane}$) as show in equation 3:

$$Rate = Conversion \times F_{propane} \qquad (3)$$

Rates were sometimes normalized by the initial rate of propane conversion, which was estimated by extrapolation back to time zero. Site-time-yields (STY) were calculated by normalizing the rate by the amount of exposed Pt measured by CO chemisorption. A first-order deactivation mechanism was assumed to estimate the initial rate of catalyst deactivation.[2,54] The deactivation coefficient, k_d (h^{-1}) is defined by equation 4:

$$k_d = \frac{\ln\frac{1-X_t}{X_t} - \ln\frac{1-X_{start}}{X_{start}}}{t} \qquad (4)$$

where X_{start} is defined as the initial conversion at zero time on stream, X_t is the conversion at time t, which is defined here as 0.83 h.

A long term deactivation parameter D quantifies the deactivation of the catalyst after the initial rapid decline in activity over the first 0.83 h on stream and is defined by equation 5:

$$D = \frac{X_t - X_{end}}{X_t} \qquad (5)$$

where X_t is the conversion at time t, defined at 0.83 h on stream, and X_{end} is the conversion after 3.1 h on stream.

3.3. Results

3.3.1. Catalyst characterization

3.3.1.1. Chemisorption of H_2 and CO

Table 3.1 shows the H_2 and CO chemisorption results on both SiO_2- and Al_2O_3-supported Pt and Pt-Sn catalysts. The H/Pt and CO/Pt for $1Pt/SiO_2$ were 0.33 and 0.30, respectively, while the H/Pt and CO/Pt for $1Pt/Al_2O_3$ were 0.50 and 0.51, respectively, indicating excellent agreement between the adsorption of the two probe molecules on the monometallic catalysts.

Table 3.1: Results from chemisorption of H_2 and CO on Pt and Pt-Sn catalysts

Catalyst	**H/Pt**	**CO/Pt**
$1Pt/SiO_2$	0.33	0.30
$1Pt0.2Sn/SiO_2$	0.083	0.11
$1Pt0.6Sn/SiO_2$[a,b]	0.044	0.081
$1Pt1.2Sn/SiO_2$	0.019	0.070
$1Pt2.4Sn/SiO_2$	0.0033	0.033
$1Pt/Al_2O_3$	0.50	0.51
$1Pt0.2Sn/Al_2O_3$	0.43	0.64
$1Pt0.6Sn/Al_2O_3$[c]	0.33	0.61
$1Pt1.2Sn/Al_2O_3$	0.20	0.56
$1Pt2.4Sn/Al_2O_3$	0.14	0.49

[a] Three separate chemisorption analyses were averaged to obtain the H/Pt and CO/Pt for $1Pt0.6Sn/SiO_2$.
[b] ICP-OES data was used to calculate H/Pt and CO/Pt for $1Pt0.6Sn/SiO_2$. The Pt wt% was 0.94% and the Sn wt% was 0.61%.
[c] ICP-OES data was used to calculate H/Pt and CO/Pt for $1Pt0.6Sn/Al_2O_3$. The Pt wt% was 0.93% and the Sn wt% was 0.68%.

For the $Pt\text{-}Sn/SiO_2$ catalysts, both the H_2 and CO uptake were inhibited as the Sn content increased. Interestingly, the uptake of H_2 was inhibited by Sn to a greater extent than the uptake of CO. Chemisorption of H_2 was also inhibited by Sn on the bimetallic Al_2O_3-supported catalysts, but not to the same extent as those supported on SiO_2. For example, the addition of 2.4 wt% Sn to $1Pt/SiO_2$ decreased the measured H/Pt ratio from 0.33 to 0.0033, whereas addition of 2.4 wt% Sn to $1Pt/Al_2O_3$ only decreased the H/Pt ratio from 0.50 to 0.14. On the alumina supported catalysts, addition of Sn did not inhibit CO uptake, which ranged from 0.49 to 0.64 over the entire range of Sn loadings.

3.3.1.2. X-Ray diffraction

The XRD patterns in the region where low index planes of the metals are present for as synthesized SiO_2-supported Pt and Pt-Sn catalysts are displayed in Figure 3.1. The $1Pt/SiO_2$ sample reveals features characteristic of Pt (111) and (200) at 39.8° and 46.1° (JCDPS 00-004-0802), respectively, whereas the addition of 0.2 wt% Sn shifted the Pt (111) and (200) peaks to lower angles (39.2° and 45.7°) indicative of incorporation of Sn into the Pt lattice. Increasing the Sn content to 0.6 wt% resulted in features associated with a Pt_3Sn alloy of 39.0° and 45.4° (JCDPS 00-035-1360) and with a PtSn alloy at 41.7° and 44.0° (JCDPS 00-025-0614). Addition of 1.2 wt% Sn decreased the intensity of the Pt_3Sn alloy peaks while increasing the intensity of the PtSn alloy peaks. The most heavily Sn-promoted (2.4 wt%) catalyst had peaks at 41.7° and 44.2°, suggesting the presence of PtSn alloy without any detectable Pt_3Sn alloy. The overlap of peaks from γ-Al_2O_3 with those of Pt-Sn alloys prevented the characterization of the alumina-supported catalysts by XRD.

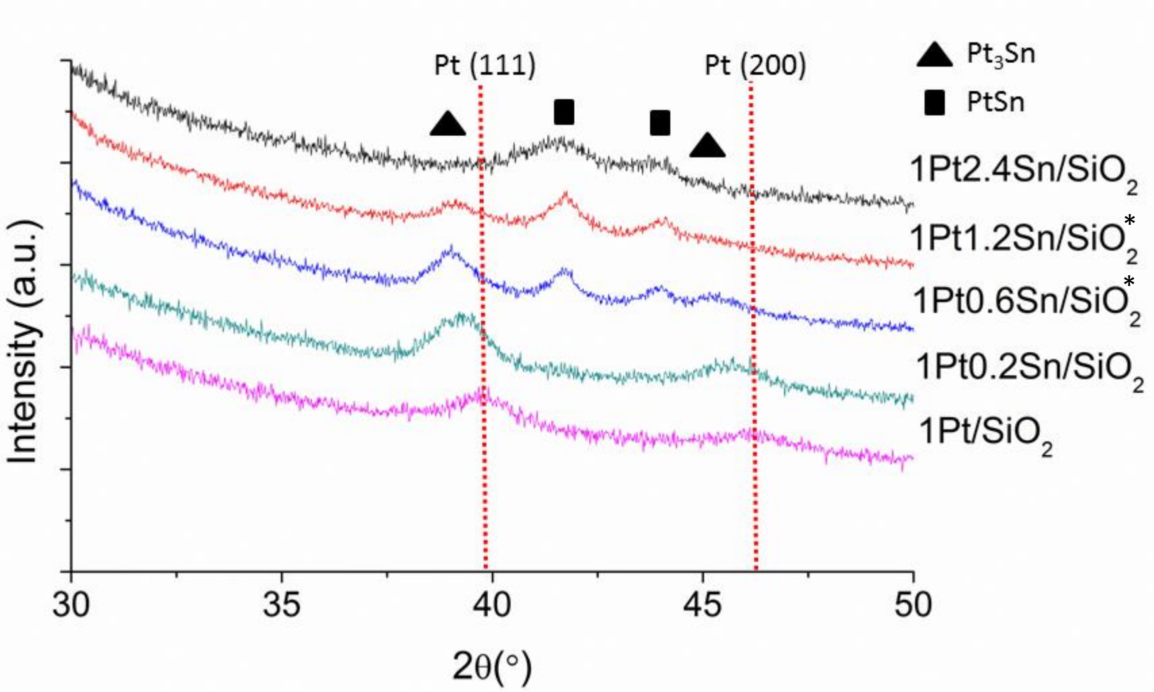

Figure 3.1: X-ray diffraction patterns of fresh Pt and Pt-Sn catalysts supported on SiO_2. Patterns are offset for clarity and *indicates a pattern was reduced by a factor of 2.

3.3.1.3. Temperature-programmed reduction

The alumina-supported catalysts were characterized by temperature-programmed reduction as an alternative to XRD (Figure 3.2). The samples were probed by TPR after the high temperature oxidative treatment but prior to pre-reduction in H_2. The oxidized 1Pt/Al_2O_3 sample revealed H_2 uptake at 444 K which is characteristic of the reduction of PtO_x species.[24,55–57] The higher temperature feature at 550 K was attributed to either hydrogen spillover on the catalyst support[35,58] or the reduction of oxychlorinated Pt species that have a strong interaction with the catalyst support.[24]

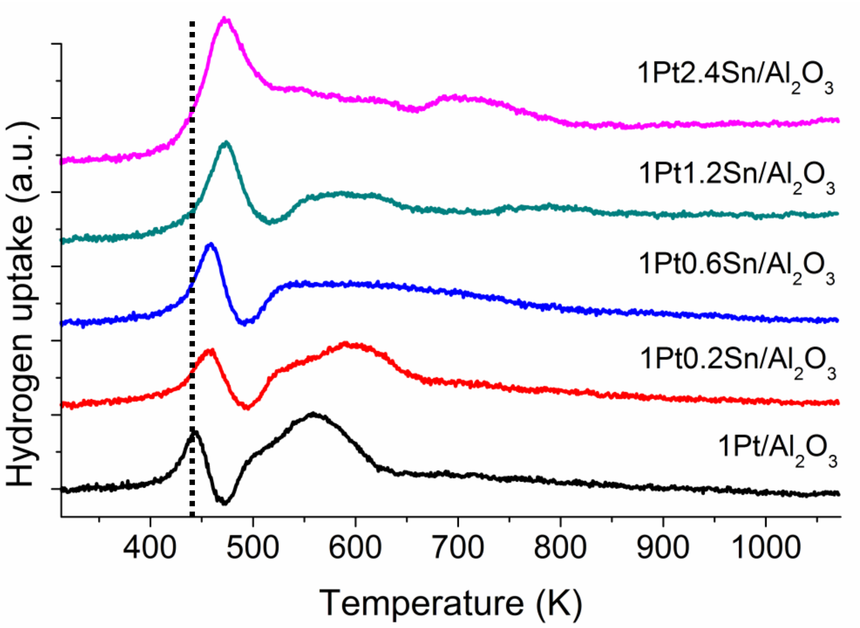

Figure 3.2: Temperature-programmed reduction of Al_2O_3-supported Pt and Pt-Sn catalysts. Patterns are offset for clarity.

The addition of Sn slightly increased the temperature of the main reduction peak of the PtO_x species. Both 0.2 wt% and 0.6 wt% Sn samples have a H_2 consumption peak at 459 K, while samples containing 1.2 wt% and 2.4 wt% Sn shift that feature to 473 K. This shift to higher reduction temperature suggests an interaction between Pt and Sn species that increases with higher Sn loadings.[55] The high temperature feature found on the 0.2 wt% Sn sample may be similar to the feature found on the monometallic Pt catalyst, which is attributed to hydrogen spillover or reduction of oxychlorinated species. This high temperature feature becomes much broader as the Sn content increases, with H_2 consumption occurring as high as 850 K. Tin species interacting with Pt have been shown to have TPR features between 573-673 K,[24,55,59] with those occurring at 700-850 K being attributed to Sn species interacting with the Al_2O_3 in the absence of nearby Pt.[22,57]

3.3.1.4. Diffuse reflectance infrared Fourier transform spectroscopy

The DRIFTS spectra of adsorbed CO on SiO_2-supported Pt and Pt-Sn catalysts are shown in Figure 3.3A. The $1Pt/SiO_2$ sample exhibits an intense band at 2067 cm^{-1} and a weak band at 1780 cm^{-1} corresponding to linear-bonded CO and bridge-bonded CO, respectively.[22,46,55,60] Addition of a small amount of Sn, as low as 0.2 wt% Sn, eliminated the weak band associated with bridge-bonded CO. Tin also slightly shifted the linear-bonded CO absorption band to 2071 cm^{-1} possibly indicating a modification of the Pt surface due to the presence of Sn.[46] The complication associated with dipolar coupling of adsorbed CO prevents a definitive conclusion based on line shift. The intensity of the linear-bonded CO band also decreased with increasing Sn content, which is consistent with the CO chemisorption results reported in Table 1.

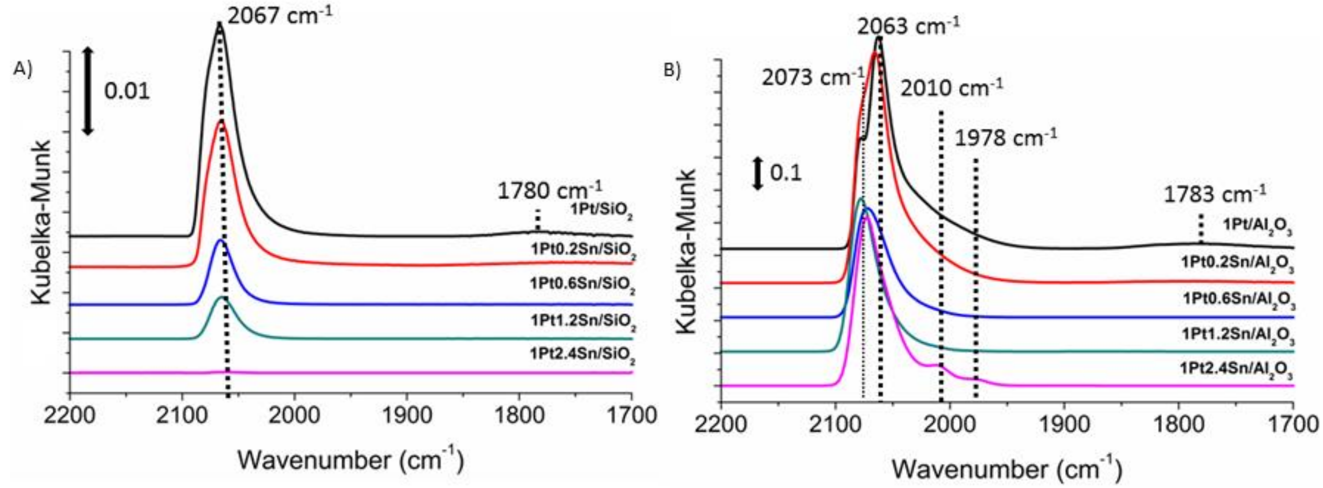

Figure 3.3: DRIFTS spectra of adsorbed CO on A) SiO_2-supported and B) Al_2O_3-supported Pt and Pt-Sn catalysts. Spectra are offset for clarity.

The DRIFTS spectra of adsorbed CO on Al_2O_3-supported Pt and Pt-Sn catalysts are shown in Figure 3.3B. Similar to the monometallic SiO_2-supported Pt catalyst, the 1Pt/Al_2O_3 sample exhibited both linear- and bridge-bonded CO adsorption with features at 2073 cm^{-1}, 2063 cm^{-1}, and 1783 cm^{-1}. The bands at 2073 cm^{-1} and 2063 cm^{-1} are indicative of linear-bonded CO on two different lattice faces of Pt nanoparticles while the peak at 1783 cm^{-1} is indicative of bridge-bonded CO.[46] Bridge-bonded CO was again eliminated by the addition of 0.2 wt% Sn on Al_2O_3-supported catalysts. Increasing Sn content also eliminated the primary feature at 2063 cm^{-1} while the feature at 2073 cm^{-1} remained, indicating modification to the exposed Pt facets. The linear band at 2073 cm^{-1} narrowed with increasing Sn content. A band at 2020 cm^{-1} has been attributed to adsorption on higher-Miller index sites or on Pt sites that interact strongly with the Al_2O_3 support.[46] Narrowing of the linear-bonded CO feature suggests that the sites corresponding to the feature at 2020 cm^{-1} are where Sn preferentially adsorbs on Pt/Al_2O_3. Two new features were observed on the heavily-promoted 2.4 wt% Sn sample at 2010 cm^{-1} and 1978 cm^{-1}, which perhaps suggests a greater extent of interaction between Pt and Sn on this heavily promoted sample.

3.3.2. Conversion of propane at constant initial conversion

The conversion of light alkanes to olefins is known to be inhibited by dehydrogenation reaction products.[2,5,29,35–37,61,62] Inhibition of the forward reaction was observed in the present study when varying the reactant flow rate and the catalyst mass over the range of values displayed in Figure 3.4. As the extent of product inhibition above propane conversions of 2% was significant, the influence of Sn promotion on the catalyst performance was evaluated under conditions at which the initial conversion was about 2%.

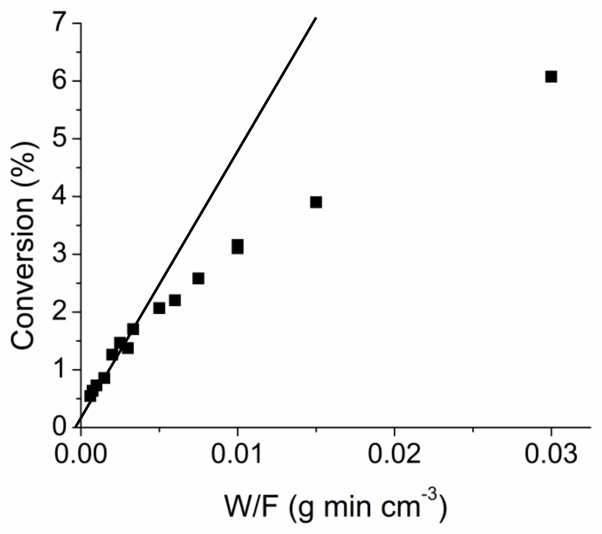

Figure 3.4: Conversion of propane at 773 K and 0.1 MPa total pressure over 1Pt2.4Sn/SiO_2 at varying flow rates and catalyst loadings. Each point represents the average steady-state conversion after at least 4 h of time on stream at each condition sampled every 15 minutes.

3.3.2.1. Influence of Sn loading at 2% initial conversion

Figure 3.5 compares the normalized rate of propane conversion over A) SiO_2- and B) Al_2O_3-supported catalysts with an initial propane conversion of ~2%. In both sets of materials, the rate of propane dehydrogenation declined rapidly over the first hour followed by a much slower rate of decline. As the Sn content was increased on the silica-supported catalysts, the relative extent of the initial deactivation decreased. The initial deactivation constant decreased from k_d= 1.4 h^{-1} to k_d= 0.22 h^{-1} as the Sn content increased from 0 wt% to 2.4 wt%, indicating a much slower rate of deactivation at early time on stream with Sn loading. The longer term deactivation parameter, D, decreased from 0.66 for Pt/SiO_2 to approximately 0 for the 1Pt2.4Sn/SiO_2 sample, indicating the highly-promoted catalyst did not deactivate appreciably after the slight initial deactivation. Whereas Sn promoted catalyst stability for the silica-supported Pt, the overall rate of conversion was substantially lowered by the presence of Sn. For example, the rate of propane conversion at 2% conversion over 1 Pt/SiO_2 and 1Pt2.4Sn/SiO_2 was 0.097 and 0.014 $mol_{propane}$ g_{cat}^{-1} h^{-1}, respectively.

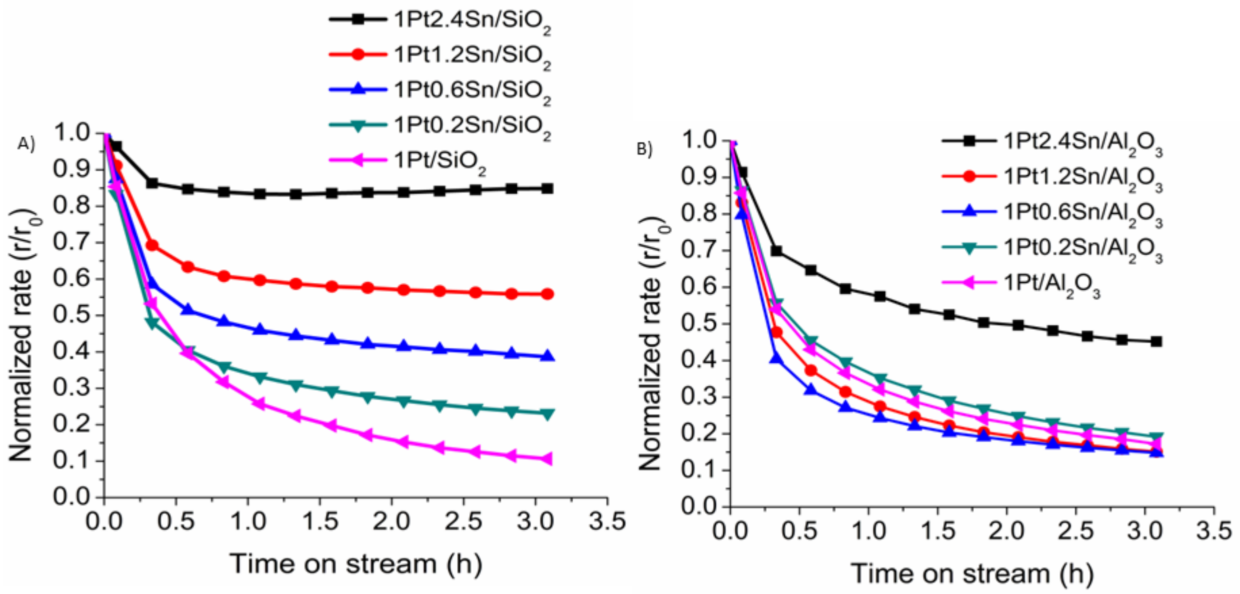

Figure 3.5: Normalized rate of propane conversion at 773 K and 0.1 MPa over A) SiO_{2}- and B) Al_2O_3-supported catalysts. The initial conversion over each catalyst was approximately 2%.

In contrast to Pt-Sn/SiO_2, the Sn content did not appear to significantly impact the stability of 1Pt/Al_2O_3 at Sn weight loadings between 0.2-1.2 wt%. The rate of deactivation was slowed on the highly promoted 2.4 wt% Sn catalyst as measured by the decrease in k_d from 1.2 h^{-1} to 0.62 h^{-1} for 1Pt/Al_2O_3 and 1Pt2.4Sn/Al_2O_3, respectively. The longer term deactivation parameter D remained relatively constant at a value of approximately 0.5 as Sn content varied from 0 to 1.2 wt% but decreased to 0.24 for the highly loaded 2.4 wt% Sn sample. The values for k_d and D are summarized in Table 3.2 and the conversion versus time plots can be found in Figure B1 of the Supplemental Materials. The selectivity to propene was greater than 99% during the propane dehydrogenation results reported in Figure 3.5.

Table 3.2: Parameters k_d and D associated with initial and longer term deactivation of Pt-Sn catalysts during propane dehydrogenation.[a]

Catalyst	k_d (h^{-1})	D
1Pt/SiO_2	1.4	0.66
1Pt0.2Sn/SiO_2	1.1	0.3
1Pt0.6Sn/SiO_2	0.92	0.2
1Pt1.2Sn/SiO_2	0.61	0.081
1Pt2.4Sn/SiO_2	0.22	0
1Pt/Al_2O_3	1.2	0.53
1Pt0.2Sn/Al_2O_3	1.1	0.52
1Pt0.6Sn/Al_2O_3	1.6	0.42
1Pt1.2Sn/Al_2O_3	1.4	0.52
1Pt2.4Sn/Al_2O_3	0.63	0.24

[a] Initial conversion was 2%.

3.3.3. Coke deposition on the catalysts

To explore the level of carbon deposited on the catalysts during propane dehydrogenation, higher initial propane conversions were employed (~4-8%) over catalysts that were not diluted in the reactor. Figure 3.6A shows the conversion of propane with time over SiO_2-supported Pt-Sn catalysts in the absence of catalyst diluent. The relative stability of the catalysts at higher conversion was similar to that reported at low conversion in Figure 3.5A. The monometallic 1Pt/SiO_2 deactivated the fastest, converting 8.0% of the propane at 5 min on stream and only 0.20% after 24 h on stream. The coke content after 24 h on stream was measured to be 1 wt% from TPO (Supplemental Materials Figure B2). The addition of 0.6 wt% Sn reduced the rate of deactivation, resulting in a conversion of 7.5% at 5 min on stream and 3.3% after 24 h on stream. The amount of coke on this sample was 0.9 wt% which is similar to that on 1Pt/SiO_2. The most stable of the three catalysts was promoted by 2.4 wt% Sn, which had 6.2% conversion at 5 min on stream and 5.1% after 24 h on stream. This sample had only 0.3 wt% coke after 24 h.

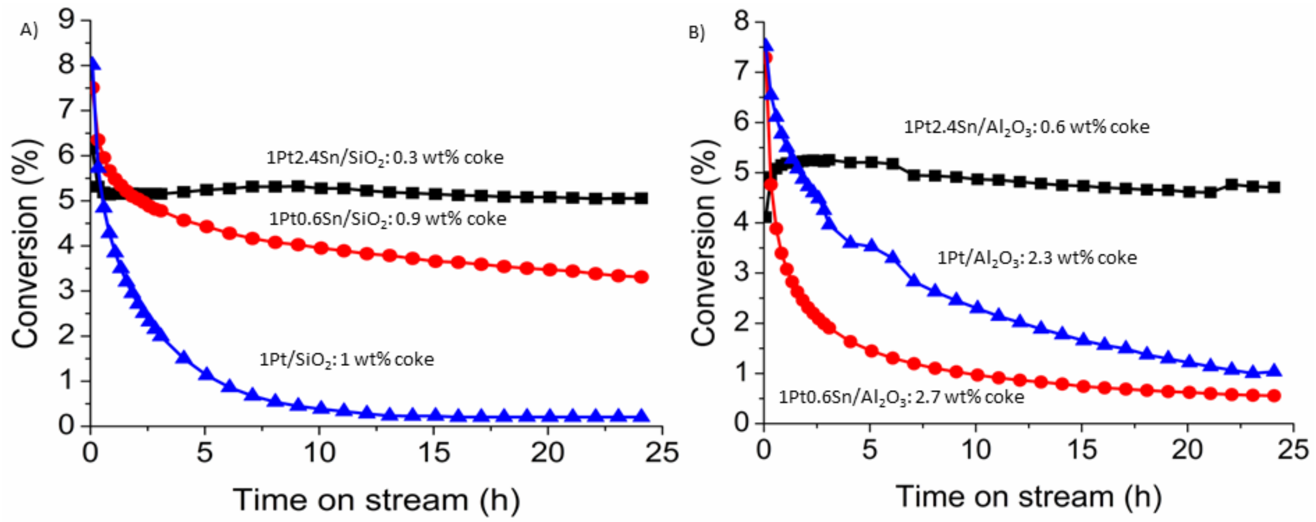

Figure 3.6: Conversion of propane with time on stream over A) SiO_2- and B) Al_2O_3-supported Pt and PtSn catalysts at 773 K and 0.1 MPa. The relative amount of coke was determined utilizing TPO.

Figure 3.6B shows the conversion of propane over undiluted Al_2O_3-supported catalysts at higher conversions. The overall trend regarding deactivation was similar to that reported in Figure 3.5 at much lower conversions. The 1Pt2.4Sn/Al_2O_3 catalyst converted 4.1% of the propane at 5 min on stream and 4.7% after 24 h on stream with only 0.6 wt% coke formed after 24 h. The monometallic 1Pt/Al_2O_3 catalyst exhibited a conversion of 7.5% at 5 min on stream and 1.0% after 24 h on stream, producing 2.3 wt% of coke, which is consistent with the greater rate of deactivation. The 1Pt0.6Sn/Al_2O_3 catalyst converted 7.3% of the propane at 5 min on stream and 0.56% after 24 h and produced 2.7 wt% coke. Interestingly, the 1Pt0.6Sn/Al_2O_3 sample deactivated the fastest and produced more coke than the un-promoted 1Pt/Al_2O_3 sample (Figure 3.6B). This may be explained by the presence of very small Pt nanoparticles, as evidenced by the number average particle size standard deviation roughly equal to the average particle size. Smaller Pt nanoparticles possess more steps and kinks, which are suggested to be where deep dehydrogenation reactions occur, and thus produce coke very rapidly with time on stream.[47] As with the silica catalysts, the most highly promoted catalysts deposited the lowest wt% of coke.

3.3.4. Evolution of metal particle size

The metal particle size of fresh samples and catalysts that had been subjected to 24 h of propane dehydrogenation at 773 K are summarized in Table 3.3. The monometallic 1Pt/SiO_2 and 1Pt/Al_2O_3 catalysts did not exhibit a signification change in Pt particle size after reaction. In the case of the Sn-promoted SiO_2 catalysts, the 0.6 wt% Sn sample increased in number average particle size from 3.8 ± 2.7 nm to 5.1 ± 2.7 nm while the 2.4 wt% Sn sample increased in number average size from 3.4 ± 1.7 nm to 4.5 ± 2.5 nm, despite the observed minimal deactivation of the 2.4 wt% Sn catalyst. For the alumina-supported catalysts, metal particle size was relatively unaffected by 24 h of reaction.

Table 3.3: Metal particle sizes determined from TEM of fresh, used, and regenerated Pt-Sn catalysts for propane dehydrogenation.

Catalyst	**Number average article size (nm)**		
	Fresh	**24 h on stream**	**Post-regeneration**
1Pt/SiO_2	3.7 ± 2.1	3.6 ± 2.9	5.1 ± 3.6
1Pt0.6Sn/SiO_2	3.8 ± 2.7	5.1 ± 2.7	5.4 ± 3.6
1Pt2.4Sn/SiO_2	3.4 ± 1.7	4.5 ± 2.5	4.8 ± 2.2
1Pt/Al_2O_3	2.5 ± 1.8	2.9 ± 1.3	2.3 ± 1.7
1Pt0.6Sn/Al_2O_3	2.9 ± 3.1	3.1 ± 3.3	3.2 ± 2.0
1Pt2.4Sn/Al_2O_3	2.8 ± 2.1	2.0 ± 2.1	1.4 ± 0.5

3.3.5 Regeneration of Pt-Sn catalysts

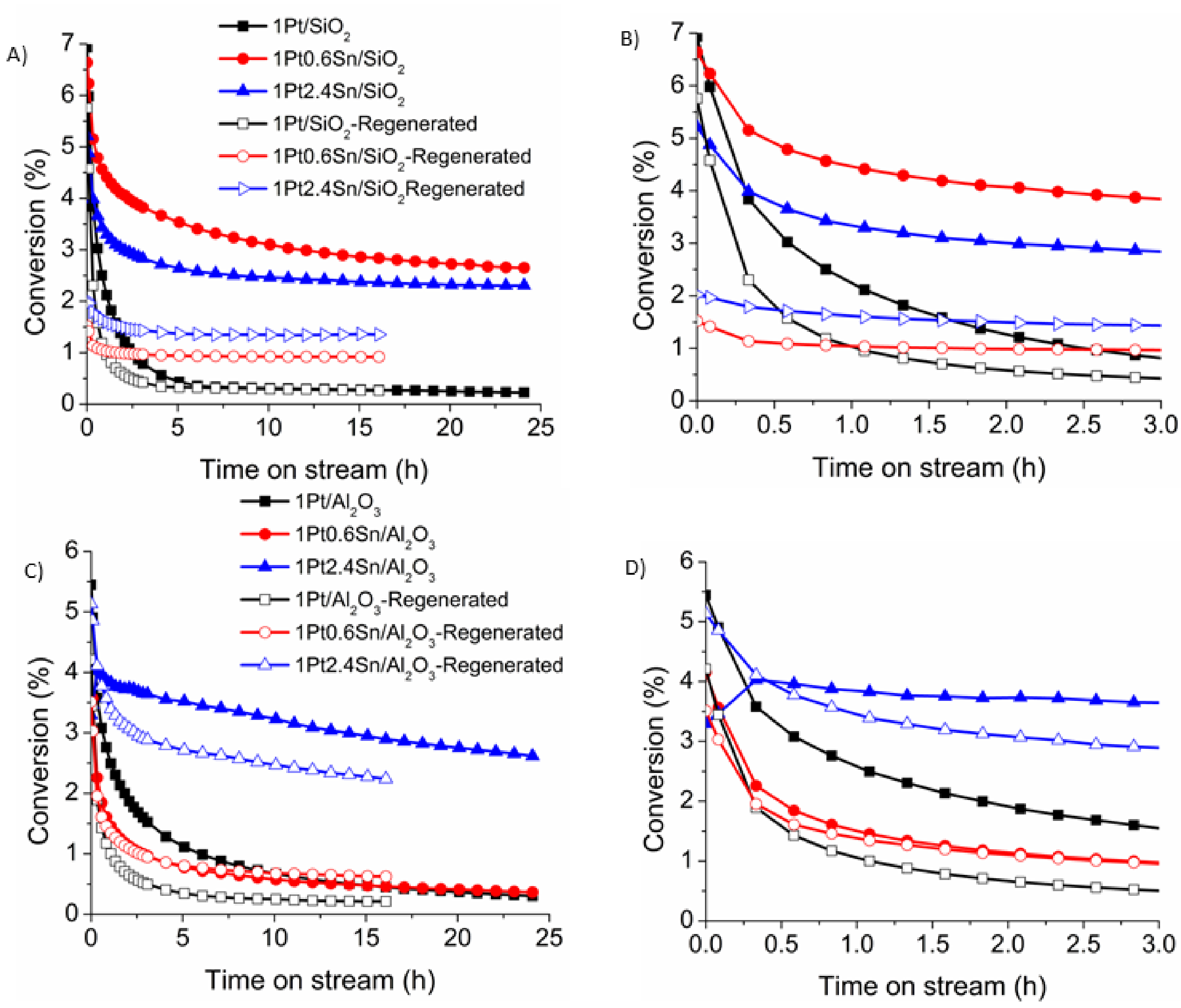

Figure 3.7: Influence of oxidative regeneration treatment on catalytic performance of A) SiO_2-supported Pt-Sn catalysts, B) first 3 h of SiO_2-supported Pt-Sn catalysts C) Al_2O_3-supported catalysts, and D) first 3 h of Al_2O_3-supported Pt-Sn catalysts. Fresh catalysts were treated in 20% O_2/He at 773 K for 1 h after initial 24.1 h on stream then re-reduced at 773 K in H_2 for 2 h.

The performance of the Pt-Sn catalysts following an oxidative treatment to remove coke in situ is compared to that of fresh catalysts in Figure 3.7. The regeneration treatment did not significantly impact the initial conversion over 1Pt/SiO_2 (5.8% vs 6.9% over fresh catalyst) and 1Pt/Al_2O_3 (5.0 % vs 5.4% over fresh catalyst). However, the oxidative treatment utilized in this study substantially decreased the initial conversion over Pt-Sn/SiO_2 catalysts. For example, the initial conversion over fresh 1Pt0.6Sn/SiO_2 was 6.6% compared to an initial conversion of 1.5% over the sample after in situ regeneration, which corresponds to a 77% loss in activity. In contrast, the unpromoted Pt catalyst recovered 84% of its initial activity. The overall influence of Sn on the stability of the catalysts as measured by the deactivation parameters k_d and D was relatively unaffected by the regeneration procedure (Table 3.4).

Table 3.4: Deactivation coefficient, long term deactivation parameter, and initial conversion over A) SiO_2- and B) Al_2O_3-supported Pt and Pt-Sn catalysts after regeneration.

Catalyst	**k_d (hr^{-1})**	**D**	**Initial conversion (%)**
1Pt/SiO_2	1.3	0.91	6.9
1Pt0.6Sn/SiO_2	0.48	0.42	6.6
1Pt2.4Sn/SiO_2	0.52	0.18	5.2
1Pt/SiO_2-Regenerated	2.0	0.78	5.8
1Pt0.6Sn/SiO_2- Regenerated	0.44	0.13	1.5
1Pt2.4Sn/SiO_2- Regenerated	0.21	0.33	2
1Pt/Al_2O_3	0.85	0.89	5.4
1Pt0.6Sn/Al_2O_3	1.2	0.77	4.1
1Pt2.4Sn/Al_2O_3	-	0.33	3.3
1Pt/Al_2O_3- Regenerated	1.6	0.82	5.0
1Pt0.6Sn/Al_2O_3- Regenerated	1.1	0.75	3.5
1Pt2.4Sn/Al_2O_3- Regenerated	0.078	0.37	5.1

The oxidation state of Sn in the fresh and regenerated 1Pt0.6Sn/SiO_2 samples was analyzed using XPS (Sn $3d_{5/2}$) and the photoemission spectra are shown in Figure 3.8. The fresh sample showed two Sn features corresponding to Sn(0) and SnO_x, of which approximately 43% was Sn(0). After regeneration, the amount of Sn(0) decreased to 29% and two features corresponding to SnO_x species were observed. The decrease in Sn(0) suggests that restructuring of the bimetallic catalyst, presumably by de-alloying of the Pt-Sn particles, occurred during the regeneration procedure. The observed decrease in activity after regeneration was likely caused by additional SnO_x species on the Pt surface as evidenced by the increase in Sn/Pt ratio from 2.2 to 2.5 for the fresh and regenerated samples, respectively. An enrichment of the Pt surface with SnO_x can physically block Pt sites and depress the observed catalytic activity. The oxidation state of Pt was also evaluated by XPS (Pt $4f_{7/2}$) and photoemission spectra are provided in Figure B3 in the Supplemental Materials. Both fresh and regenerated 1Pt0.6Sn/SiO_2 were consistent with Pt(0) at 70.6 eV and 70.7 eV, with no features corresponding to PtO_x.

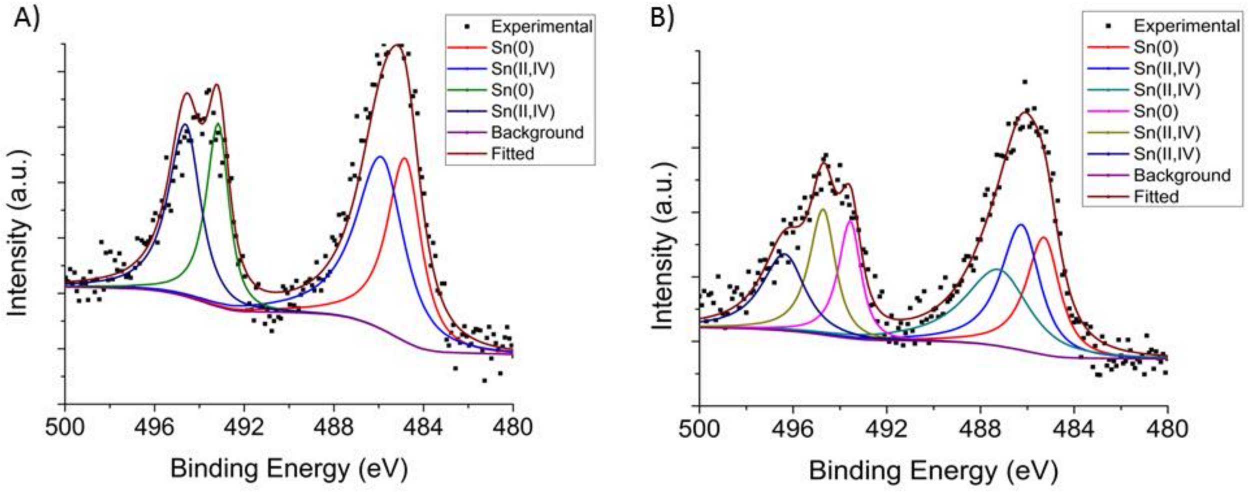

Figure 3.8: Tin $3d_{5/2}$ photoemission spectra of A) fresh and B) regenerated 1Pt0.6Sn/SiO_2. The regenerated sample was tested for propane dehydrogenation for 24 and regenerated in situ in flowing synthetic air for 1 h at 773 K followed by reduction in flowing H_2 for 2 h at 773 K. After regeneration, the catalyst was then tested for propane dehydrogenation activity for an additional 16 h prior to XPS analysis.

The effect of regeneration conditions on the conversion of propane over Al_2O_3-supported Pt and Pt-Sn catalysts is shown in Figure 3.7C. Unlike the case with SiO_2, the highly promoted 2.4 wt% Sn catalyst on Al_2O_3 was successfully regenerated without substantial loss of activity. The monometallic Pt/Al_2O_3 catalyst exhibited a 93% recovery of the initial activity but its k_d increased from 0.85 to 1.6 h^{-1} as a result of the more rapid deactivation observed post regeneration. The regeneration performance of the low loaded Sn catalyst (1Pt0.6Sn/Al_2O_3) was similar to that of unpromoted Pt/Al_2O_3.

Representative STEM images used to analyze particle sizes of samples after regeneration can be found in the Supplemental Materials (Figures B4 (SiO_2) and B5 (Al_2O_3)) and a summary of the particle sizes can be found in Table 3.3. Minor sintering was observed on the 1Pt/SiO_2 sample following reaction and regeneration. The fresh 1Pt/SiO_2 had a number average particle size of 3.7 ± 2.1 nm while the regenerated sample was 5.1 ± 3.6 nm, which may partially account for the slight decrease in activity and the more rapid deactivation observed over the regenerated 1Pt/SiO_2 catalyst. Additional sintering was observed on the 1Pt0.6Sn/SiO_2 sample. Reaction and regeneration increased the particle size of all of the Sn-promoted Pt/SiO_2 samples investigated (Table3).

In contrast to the silica-supported catalyst, the particle size of the 1Pt2.4/Al_2O_3 sample actually decreased after oxidative regeneration treatment, presumably by oxidative redispersion. The monometallic 1Pt/Al_2O_3 and 1Pt0.6Sn/Al_2O_3 experienced little change in metal particle size following reaction and regeneration.

3.3.6. Pt-Sn catalysts prepared by the polyol method

3.3.6.1. Physical properties of catalysts

Table 3.5: Results for H_2 and CO chemisorption on polyol-synthesized catalysts.

Catalyst	H/Pt	CO/Pt	Pt (wt%)[a]	Sn (wt%)[a]
1Pt0.6Sn/SiO_2-P	0.053	0.13	0.66	0.55
1Pt0.6Sn/Al_2O_3-P	0.059	0.51	0.71	0.49

[a]Weight loadings of Pt and Sn were measured via ICP-OES.

The chemisorption uptakes for the polyol-synthesized catalysts are shown in Table 3.5. The 1Pt0.6Sn/SiO_2-P sample had H/Pt and CO/Pt ratios of 0.053 and 0.13, respectively. These chemisorption results are similar to those observed for the 1Pt0.6Sn/SiO_2 sample synthesized by IWI (Table 1). The hydrogen uptake on 1Pt0.6Sn/Al_2O_3-P resulted in H/Pt=0.059, which is a low value consistent with the silica-supported sample, but completely different than the 1Pt0.6Sn/Al_2O_3-P prepared by IWI (H/Pt=0.33). Clearly, the method of preparation is very important when alumina is used as a support.

The uptake of CO on 1Pt0.6Sn/Al_2O_3-P gave CO/Pt=0.51 which is similar to the analogous catalyst prepared by IWI.

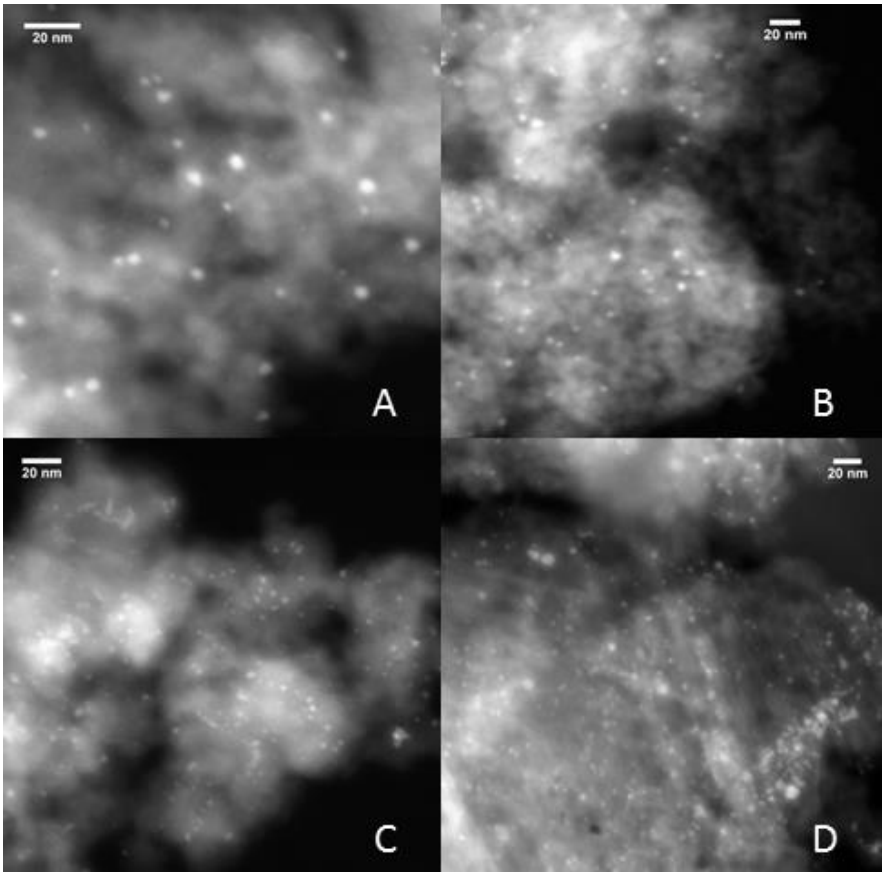

Figure 3.9: STEM images of A) fresh 1Pt0.6Sn/SiO_2-P, B) regenerated 1Pt0.6Sn/SiO_2-P, C) fresh 1Pt0.6Sn/Al_2O_3-P, and D) regenerated 1Pt0.6Sn/Al_2O_3-P.

Dark-field STEM images of fresh polyol-synthesized catalysts are shown in Figure 3.9 (A & C). Particle sizes summarized in Table 3.6 illustrate the relative uniformity of sizes achieved by colloidal synthesis. The average particle size for silica-supported and alumina-supported 1Pt0.6Sn particles prepared by the polyol method was 3.1 ± 1.5 nm and 3.5 ± 1.1 nm, respectively.

Table 3.6: Particle size of fresh and regenerated polyol-synthesized catalysts.

Catalyst	**Average particle size (nm)**	
	Fresh	**Post-regeneration**
1Pt0.6Sn/SiO_2-P	3.1 ± 1.5	3.4 ± 1.2
1Pt0.6Sn/Al_2O_3-P	3.5 ± 1.1	2.2 ± 0.9

The XRD pattern for the 1Pt0.6Sn/SiO_2-P sample is given in Figure B6 in the Supplemental Materials. Peaks associated with Pt_3Sn alloy (39.0° and 45.3°) and PtSn alloy (41.8° and 44.1°) were present in the pattern, which is consistent with the alloys detected by XRD in the analogous sample prepared by IWI (Figure 3.1).

Temperature-programmed reduction of the 1Pt0.6Sn/Al_2O_3-P catalyst shown in Figure B7 of the Supplemental Materials revealed two major hydrogen uptake features at ~360 K and ~510 K. The feature at ~510 K is similar to that observed on the Al_2O_3-supported catalysts prepared by IWI and is attributed to Pt and Pt-Sn reduction.[24,55] The low temperature feature at ~360 K is thought to result from reduction of surface oxide or chemisorbed oxygen on Pt that was previously reduced during the polyol synthesis process.

The adsorption of CO on polyol-synthesized catalysts evaluated by DRIFTS is shown in Figure B8 of the Supplemental Materials. The 1Pt0.6Sn/SiO_2-P sample displayed a single band at 2064 cm^{-1} corresponding to linearly adsorbed CO and the intensity of the band was an order of magnitude lower than that observed on the IWI-synthesized 1Pt0.6Sn/SiO_2 catalyst (Figure 3.3A). The 1Pt0.6Sn/Al_2O_3-P also showed a single band attributed to linear-bonded CO at 2070 cm^{-1} and the intensity of the feature on this Al_2O_3-supported polyol catalyst was an order of magnitude lower than that associated with CO on the IWI-synthesized 1Pt0.6Sn/Al_2O_3 sample (Figure 3.3B).

3.3.6.2 Conversion of propane over polyol-synthesized Pt-Sn catalysts

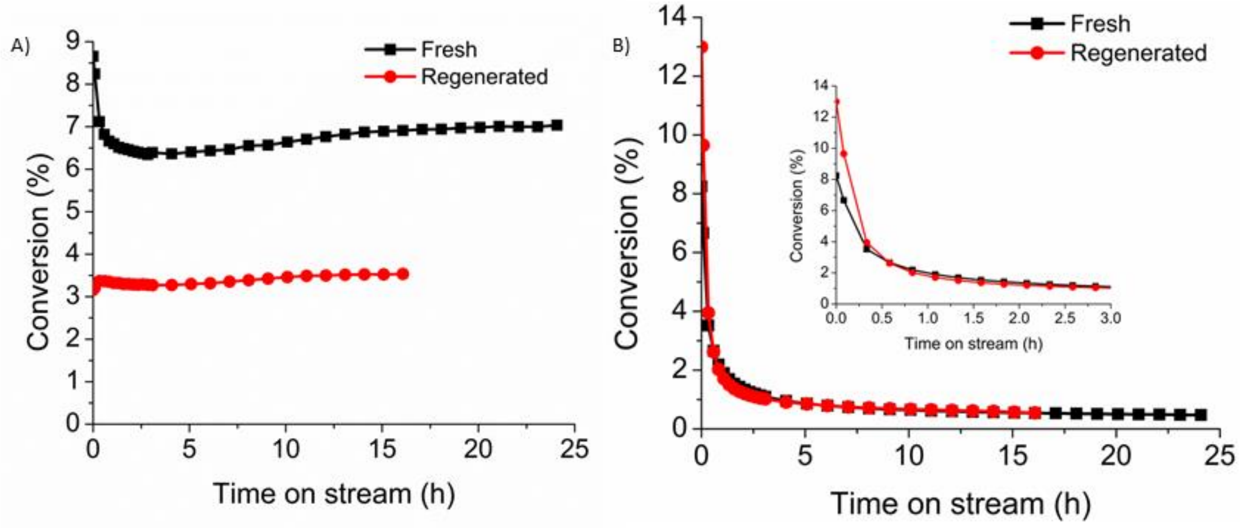

Figure 3.10: Conversion of propane with time over A) 1Pt0.6Sn/SiO$_2$-P and B) 1Pt0.6Sn/Al$_2$O$_3$-P at 773 K and 0.1MPa. A zoomed-in region of the Al$_2$O$_3$-supported catalyst is included for clarity.

Figure 3.10A shows the conversion of propane over both fresh and in situ-regenerated 1Pt0.6Sn/SiO$_2$-P. The initial conversion over the fresh catalyst was 8.7% prior to deactivating to 6.7% conversion at 0.83 h on stream, resulting in a k_d of 0.34 h^{-1}. As the analogous IWI-synthesized 1Pt0.6Sn/SiO$_2$ catalyst exhibited a k_d= 0.92 hr^{-1} (Table 2), apparently the polyol synthesis method improved the initial catalyst stability. Moreover, the 0.6 wt% Sn SiO$_2$-polyol catalyst remained relatively stable on stream for 24 h without exhibiting longer term deactivation. Interestingly, the conversion slowly increased after 3 h on stream. After 24 h the catalyst was subjected to our standard regeneration treatment in situ and re-evaluated for activity. The regenerated catalyst converted 3.2% of the propane initially, which is a 63% decrease in the initial conversion rate compared to the fresh catalyst. As with the catalysts prepared by IWI, we attribute the irreversible loss in catalyst activity to de-alloying and surface enrichment of SnO$_x$. Since the deactivation of the regenerated sample was negligible, no deactivation coefficient k_d can be reported for the regenerated 1Pt0.6Sn/SiO$_2$-P catalyst. Examination of the sample after regeneration did not reveal any significant change in metal particle size (3.1 nm vs 3.4 nm as reported in Table 3.6).

Figure 3.10B displays the conversion of propane during 24h over the fresh and in situ-regenerated 1Pt0.6Sn/Al_2O_3-P catalyst. The calculated deactivation parameters k_d and D of the fresh polyol-synthesized alumina-supported catalyst were 1.7 h^{-1} and 0.78, respectively, but changed to 2.4 h^{-1} and 0.73 after regeneration. The average particle size was reduced to 2.2 ±0.9 nm following regeneration (Table 3.6).

3.3.7. Propane conversion with co-fed H_2

3.3.7.1. Influence of Sn promoter on propene selectivity

The influence of Sn promotion on the product selectivity in the presence of co-fed H_2 was explored utilizing the 1Pt/Al_2O_3 and 1Pt0.6Sn/Al_2O_3-P catalysts (Figure 3.11A). In the absence of co-fed H_2, the selectivity to propene was >99% over all catalysts, with the lone exceptions being the monometallic Pt catalysts at 5 min on stream. The selectivity to propene in the aforementioned exceptions was still >98% for those initial conversion points. In contrast, the presence of co-fed H_2 decreased the selectivity to propene over the 1Pt/Al_2O_3 sample when the initial conversion was ~4% or greater (Figure 3.11), producing methane, ethane, and ethene as side products. The addition of Sn to Pt has been suggested to improve the selectivity to propene during propane dehydrogenation by diluting large Pt ensembles that are required for hydrogenolysis.[2,29,62] Indeed, the presence of Sn improved the selectivity to propene even in the presence of co-fed H_2 (Figure 3.11A). Hydrogenolysis products were not detected over the 1Pt0.6Sn/Al_2O_3-P at conversions below ~7%. The selectivity to propene at 11.8% conversion over the promoted catalyst was >98%, which is an improvement compared to the 92% propene selectivity at 11.3% conversion over 1Pt/Al_2O_3. Interestingly, selectivity to propene increased with time on stream over 1Pt/Al_2O_3 (Figure 3.11B), which suggests that trace amounts of coke deposited on Pt promote propene selectivity, presumably by disrupting the large ensembles of Pt needed to catalyze hydrogenolysis.

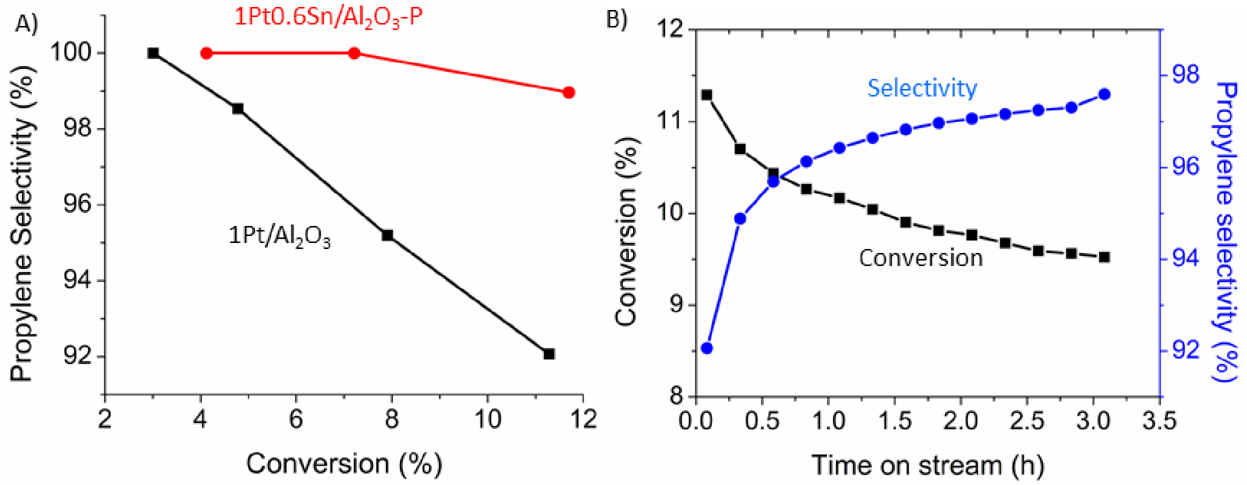

Figure 3.11: A) Influence of initial conversion on the selectivity to propene measured at 5 min on stream in the presence of co-fed H_2. B) Effect of time on stream on conversion and selectivity over $1Pt/Al_2O_3$. Total catalyst loading and flow rate were varied to adjust the initial conversion at 773 K. The H_2:propane:N_2 ratio was 1:2:5 at a total pressure of 0.1 MPa.

3.3.7.2 Catalytic rate

Co-fed H_2 decreased the rate of coke formation and thus improved catalyst stability during propane dehydrogenation, allowing for the quantification of catalytic rates.[5,37] Thus, the conversion and site time yield (STY, normalized by CO/Pt) of propene over Pt/SiO_2 and $Pt\text{-}Sn/SiO_2$ in the presence of co-fed H_2 is shown is Figure 3.12. The initial STY of Pt/SiO_2 was about 3 s^{-1} based on Pt dispersion evaluated from CO chemisorption. For comparison, Barias et al. report an initial turnover frequency for propane dehydrogenation of 1 s^{-1} at 792 K and 0.3 bar propane over their synthesized Pt/SiO_2, which compares very well to the current study.[63] Moreover, the turnover rate for isobutane dehydrogenation over Pt/SiO_2 at 773 K as reported by Stagg et al. was about 3 s^{-1}, albeit at a partial pressure of hydrocarbon that was 2.7 times that used in the current work.[30] Although a Weisz-Prater analysis (see Supplemental Material) indicates the most active Pt/SiO_2 catalyst may be slightly affected by transport limitations during propane dehydrogenation in H_2, the lower observed rates over the Sn-promoted catalysts and those catalysts that have undergone deactivation are clearly free from transport artifacts.

The STY of the two bimetallic catalysts appeared to be impacted by their respective synthesis methods. The polyol-synthesized catalyst exhibited initial activity less than half that of the monometallic catalyst. In contrast, the IWI-synthesized 1Pt0.6Sn/SiO_2 sample had an initial STY 40% higher than the monometallic catalyst. Despite similar H/Pt and CO/Pt ratio observed on the 1Pt0.6Sn/SiO_2 catalysts, the observed initial STY differed by a factor of 3.4.

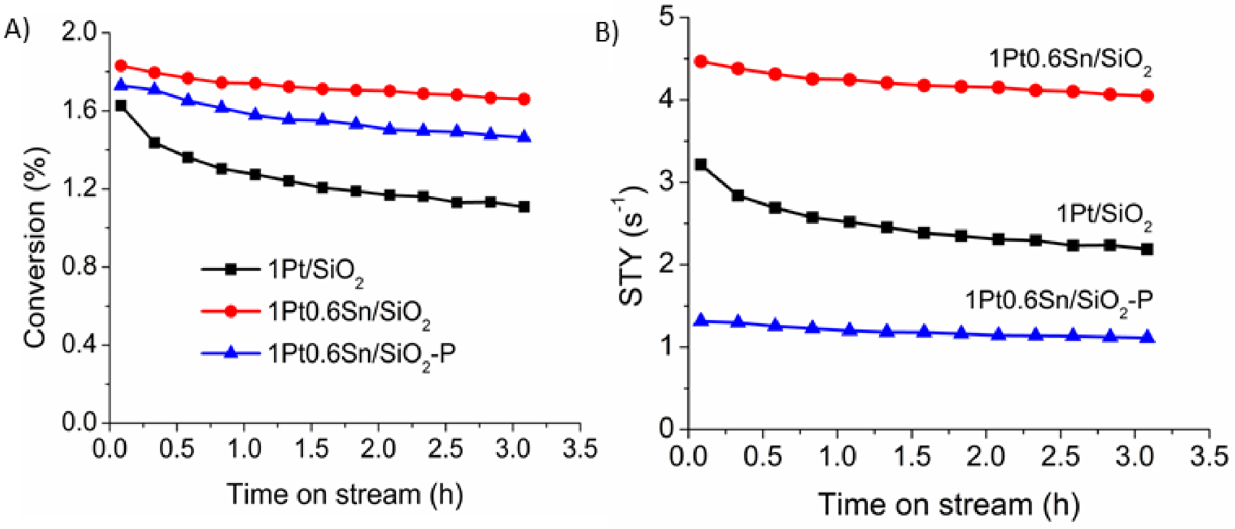

Figure 3.12: Conversion of propane over A) SiO_2- and B) Al_2O_3-supported Pt and Pt-Sn catalysts. STY normalized by CO/Pt over C) SiO_2- and D) Al_2O_3-supported Pt and Pt-Sn catalysts. The reaction temperature was 773 K at 0.1 MPa total pressure. Total catalyst loading and flow rates were varied to adjust the conversion. The H_2:propane:N_2 ratio was 1:2:5.

3.4. Discussion

3.4.1. Influence of catalyst support and Sn loading

3.4.1.1. SiO_2 support

Hydrogen chemisorption was inhibited by increasing the Sn content on Pt/SiO_2, and this inhibition has been attributed to the disruption of Pt ensembles by Sn.[64] The dissociative adsorption of H_2, which is required for hydrogen chemisorption, requires adjacent Pt sites and can be inhibited by the formation of Pt-Sn alloys or by SnO_x surface species blocking these pairwise ensembles. Interestingly, CO chemisorption was not inhibited by Pt-Sn to the same extent as observed with hydrogen chemisorption. For example, the H/Pt and CO/Pt ratios on the $1Pt2.4Sn/SiO_2$ sample were 0.3% and 3%, respectively. The disparity between the chemisorption results on this heavily promoted sample suggests disruption of Pt ensembles because CO chemisorption can occur on isolated Pt surface sites while hydrogen chemisorption may not. Furthermore, charge donation from Sn to Pt has been reported previously and will alter the electronic structure of Pt.[64] This so-called ligand effect may also influence the chemisorption of hydrogen as the dissociative adsorption of H_2 on Pt-Sn alloys can become a more activated process compared to Pt alone. A third alternative for the difference between H/Pt and CO/Pt on the silica-supported samples is CO induced surface segregation of Pt during the chemisorption experiment.

Computational modeling has suggested Pt-Sn alloys can improve the stability of propane dehydrogenation activity while decreasing the catalyst activity by increasing the barrier for dissociative adsorption of propane.[31] Alloys with greater Sn contents (i.e. Pt_2Sn or $PtSn_2$) have been proposed to exhibit lower activity compared to Pt_3Sn alloy and unalloyed Pt.[31] Indeed, XRD characterization reported here showed that as the Sn content is increased on SiO_2-supported catalysts, the PtSn content increased while Pt_3Sn content decreased until only PtSn alloy was present at 2.4wt% Sn loading (Figure 3.1). The trend in the normalized rate of propane conversion over SiO_2-supported catalysts (Figure 3.5) supports the idea that Pt-Sn alloy formation improves stability while decreasing activity. In Figure 3.5, similar catalyst loadings were used to achieve approximately 2% initial conversion for the 0.6 wt% Sn catalyst and the 1.2 wt% Sn catalyst. However, the rate differed by a factor of ~2 with observed rates over $1Pt0.6Sn/SiO_2$ and $1Pt1.2Sn/SiO_2$ equal to 0.28 and 0.13 $mol_{propane}\ g_{cat}^{-1}\ h^{-1}$, respectively . The 2.4 wt% Sn catalyst only showed features indicative of the PtSn alloy, exhibited the most stable activity, but exhibited the lowest rate at 0.014 $mol_{propane}\ g_{cat}^{-1}\ h^{-1}$.

The relative amount of coke formed on each catalyst also decreased with increasing Sn content. Tin is known to inhibit the side reactions leading to coke formation and can also help coke precursors migrate from Pt sites to the catalyst support.[2,7] It is speculated that the similar amount of coke on the 0.6 wt% Sn catalyst compared to $1Pt/SiO_2$ indicates that the coke resides on the SiO_2 surface instead of on the Pt sites due to the coke precursor mobility of Sn-promoted catalysts. The total amount of coke was actually highest on the $1Pt2.4Sn/SiO_2$ despite having the lowest relative amount of coke (wt%). The disconnect between relative and total amount of coke arises from the total amount of catalyst in the reactor. A total of 250 mg of $1Pt2.4Sn/SiO_2$ was used in Figure 3.6, compared to 50 mg of $1Pt/SiO_2$. The higher amount of silica support and sustained reactivity in the 2.4 wt% Sn sample allows for more coke precursors to be captured by the support over 24 h on stream.

Attempts to regenerate the bimetallic SiO_2-supported catalysts proved to be unsuccessful. The XPS results from regenerated $1Pt0.6Sn/SiO_2$ suggest that some Sn de-alloyed from the bimetallic particles and migrated to the Pt nanoparticle surface and support surface, as evidenced by the increase in Sn/Pt surface ratio from 2.2 to 2.5 post-regeneration. These results are consistent with those reported by Xie et al. who demonstrated that Pt-Sn/C forms Pt-Sn alloy after reduction but de-alloys and phase segregates following the aqueous phase oxidation of 1,6-hexanediol.[53] Freakley et al. observed a similar enrichment of SnO_x on Pd nanoparticle surfaces following a calcination-reduction treatment which was attributed to a stronger affinity between SnO_x and Pd than between the SnO_x and TiO_2 support.[65]

3.4.1.2. Al_2O_3 support

Similar to the SiO_2-supported catalysts, the bimetallic Al_2O_3-supported catalysts exhibited a decrease in H/Pt with the addition of Sn. However, the CO chemisorption uptake did not appear to be impacted to the same extent as the hydrogen chemisorption. The majority of the Sn, however, likely resided on the Al_2O_3 surface due to its strong interaction with the support material instead of on the Pt nanoparticle surface.[2,4,5,45,46,57,66] Since Sn exhibits weaker interactions with SiO_2, any excess SnO_x could interact with Pt sites resulting in a significant decrease to both H/Pt and CO/Pt on the silica-supported samples. The CO DRIFTS results (Figure 3.3B) on the alumina-supported catalysts suggest that any Sn on the Pt surface resides on higher Miller index sites such as the steps and kinks, as evidenced by the narrowing on the linear adsorption band.[46] The difference between H and CO adsorption on Pt-Sn/Al_2O_3 is quite intriguing and may result from a higher barrier to dissociative chemisorption of H_2 on bimetallic particles.

In contrast to the SiO_2-supported catalysts, an improvement in catalyst stability (Figure 3.5B) was only observed at the relatively high 2.4 wt% Sn loading. This 1Pt2.4Sn/Al_2O_3 sample was also the only one examined to exhibit bands for linear-adsorbed CO at 2010 and 1978 cm^{-1}, which suggested a higher degree of interaction between the Pt and Sn species. Such interaction is consistent with the improved catalyst stability observed even at higher conversions (Figure 3.6B). A higher Sn content was shown to reduce coke formation on the 2.4 wt% Sn catalyst and thus improve the catalyst stability, which was consistent with the Pt-Sn/SiO_2 catalysts. Recent work by Pham et al. has suggested that the deactivation of Al_2O_3-supported PtSn catalysts may be due to particle sintering in addition to coke formation.[4] It appears that the relative coke content after 24 h on stream observed in our work correlated well with the observed deactivation trends while sintering played a minor role in the extent of deactivation under the reaction conditions used in this study.

The widely utilized Oleflex industrial propane dehydrogenation process is known to utilize a Pt-Sn/Al_2O_3 catalyst system.[2] The contrast between the ability to regenerate Pt-Sn on SiO_2 compared to Al_2O_3 highlights one of the reasons why Al_2O_3 is utilized in the industrial process. Regeneration of all three of the examined Pt-Sn/Al_2O_3 catalysts resulted in recovery of the catalytic activity as well as redispersion of Pt-Sn nanoparticles (Tables 3 & 6). Pham et al. demonstrated that Sn can act as a nucleation site for Pt redispersion during regeneration, aiding in the recovery of catalytic activity.[4] This explains the unique activity and particle size change observed on the 1Pt2.4Sn/Al_2O_3 and 1Pt0.6Sn/Al_2O_3-P samples after regeneration.

3.4.2. Influence of synthesis method

The polyol synthesis method has been demonstrated to produce monodisperse bimetallic nanoparticles[49,67] and our results reported in Table 3.6 are consistent with those reports. For example, the fresh 1Pt0.6Sn/SiO_2-P sample had an average particle size of 3.1 ± 1.5 nm whereas the fresh 1Pt0.6Sn/SiO_2 prepared via traditional incipient wetness impregnation had an average particle size of 3.8 ± 2.7 nm. The greater standard deviation associated with catalysts prepared by incipient wetness impregnation is indicative of a wider distribution of particle sizes than the sample prepared by the polyol synthesis method.

A second advantage of the polyol synthesis method is the creation of bimetallic precursor particles in solution prior to depositing them on the support. Therefore, the Pt-Sn interaction can be achieved before the affinity of the supports for Sn affects the formation of bimetallic particles. Reactivity results of the polyol-synthesized silica-supported catalysts were consistent with a more extensive interaction between Pt and Sn than an analogous sample prepared by standard impregnation of metal precursors. Unfortunately, oxidative regeneration of 1Pt0.6Sn/SiO_2-P irreversibly deactivated the catalyst, presumably by de-alloying the Pt particles. The strong interaction of Sn with the alumina support ultimately resulted in promoted catalysts that were similar in performance regardless of preparation method. Indeed, the oxidative regeneration of 1Pt0.6Sn/Al_2O_3-P (Figure 3.10B) was very similar to the analogous catalyst prepared by incipient wetness impregnation (Figure 3.7C).

3.5. Conclusion

The reactivity of SiO_2- and Al_2O_3-supported Pt and Pt-Sn catalysts for propane dehydrogenation is affected by the strength of interaction of Sn with Pt relative to the support. Low weight loadings of Sn were much less effective at promoting propene selectivity and stability of Pt/Al_2O_3 than Pt/SiO_2 during propane dehydrogenation because of the high affinity of Sn species for the alumina. The primary factor influencing catalyst deactivation was the deposition of coke, regardless of the support. In contrast to the alumina-supported catalysts, oxidative regeneration of SiO_2-supported catalysts caused irreversible loss of activity attributed to the segregation of SnO_x species to the surfaces of the bimetallic particles. Although preforming bimetallic particles via a colloidal synthesis method achieved a narrower particle size distribution, the performance of the catalyst was still correlated with the interaction of metals with the support.

3.6. Acknowledgements

This material was based upon the work partially supported by the National Science Foundation under award number EEC-0813570. Any opinions, findings, and conclusions or recommendations expressed in these materials are those of the author(s) and do not necessarily reflect the views of the National Science Foundation. The authors would like to acknowledge Dr. Helge Heinrich and Catherine Dukes in the Department of Materials Science and Engineering at the University of Virginia. Helpful discussions with Dr. Jiahan Xie, Dr. Zachary Young, and James Kammert are also acknowledged.

3.7. References for Chapter 3

1. Alper, J. *The Changing Landscape of Hydrocarbon Feedstocks for Chemical Prodction: Implications for Catalysis: Proceedings of a Workshop*. (The National Academies Press, 2016). doi:10.17226/23555

2. Sattler, J. J. H. B., Ruiz-Martinez, J., Santillan-Jimenez, E. & Weckhuysen, B. M. Catalytic Dehydrogenation of Light Alkanes on Metals and Metal Oxides. *Chem. Rev.* **114,** 10613–10653 (2014).

3. Weckhuysen, B. M. & Schoonheydt, R. A. Alkane dehydrogenation over supported chromium oxide catalysts. *Catal. Today* **51,** 223–232 (1999).

4. Pham, H. N., Sattler, J. J. H. B., Weckhuysen, B. M. & Datye, A. K. The Role of Sn in the Regeneration of Pt/γ-Al2O3 Light Alkane Dehydrogenation Catalysts. *ACS Catal.* **6,** 2257–2264 (2016).

5. Resasco, D. E. in *Encyclopedia of Catalysis* (2000).

6. Volter, J. & Kurschner, U. Deactivation of Supported Pt and Pt-Sn catalysts in the Conversion of Methylcyclopentane. *Appl. Catal.* **8,** 167–176 (1983).

7. Vu, B. K. *et al.* Location and structure of coke generated over Pt-Sn/Al2O3 in propane dehydrogenation. *J. Ind. Eng. Chem.* **17,** 71–76 (2011).

8. Vu, B. K. *et al.* Pt-Sn alloy phases and coke mobility over Pt-Sn/Al2O3 and Pt-Sn/ZnAl2O4 catalysts for propane dehydrogenation. *Appl. Catal. A Gen.* **400,** 25–33 (2011).

9. Sattler, J. J. H. B. *et al.* Platinum-Promoted Ga / Al 2 O 3 as Highly Active , Selective , and Stable Catalyst for the Dehydrogenation of Propane **. *Angew. Chem. Int. Ed. Engl.* **53,** 9251–9256 (2014).

10. Ma, Z., Wu, Z. & Miller, J. T. Effect of Cu content on the bimetallic Pt – Cu catalysts for propane dehydrogenation. *Catal. Struct. React.* **3,** 43–53 (2017).

11. Cybulskis, V. J. *et al.* Zinc Promotion of Platinum for Catalytic Light Alkane Dehydrogenation: Insights into Geometric and Electronic Effects. *ACS* **7,** 4173–4181 (2017).

12. De Cola, P. L., Glaser, R. & Weitkamp, J. Non-oxidative propane dehydrogenation over Pt – Zn-containing zeolites. *Appl. Catal. A Gen.* **306,** 85–97 (2006).

13. López-Suárez, F. E. *et al.* Platinum–tin/carbon catalysts for ethanol oxidation: Influence of Sn content on the electroactivity and structural characteristics. *Int. J. Hydrogen Energy* **40,** 12674–12686 (2015).

14. Gavagnin, R., Biasetto, L., Pinna, F. & Strukul, G. Nitrate removal in drinking waters : the effect of tin oxides in the catalytic hydrogenation of nitrate by Pd / SnO 2 catalysts. *Appl. Catal. B Environ.* **38,** 91–99 (2002).

15. Schmid, W., Bârsan, N. & Weimar, U. Sensing of hydrocarbons and CO in low oxygen conditions

with tin dioxide sensors: possible conversion paths. *Sensors Actuators B Chem.* **103,** 362–368 (2004).

16. Santori, G., Casella, M. & Siri, G. Hydrogenation of crotonaldehyde on Pt/SiO 2 catalysts modified with tin added via surface organometallic chemistry on metals techniques. *Appl. Catal. A Gen.* **197,** 141–149 (2000).

17. Huber, G. W., Shabaker, J. W. & Dumesic, J. A. Raney Ni-Sn catalyst for H2 production from biomass-derived hydrocarbons. *Science* **300,** 2075–7 (2003).

18. Kaylor, N. *et al.* Vapor phase deoxygenation of heptanoic acid over silica-supported palladium and palladium-tin catalysts. *J. Catal.* **344,** 202–212 (2016).

19. Deng, T. & Liu, H. Promoting effect of SnO x on selective conversion of cellulose to polyols over bimetallic Pt–SnO x /Al 2 O 3 catalysts. *Green Chem.* **15,** 116–124 (2013).

20. Jiang, L., Zhou, Z., Li, W., Zhou, W. & Song, S. Effects of Treatment in Different Atmosphere on Pt 3 Sn / C Electrocatalysts for Ethanol Electro-oxidation. *Energy Fuels* **18,** 866–871 (2004).

21. Piscina, P. R. De, Llorca, J., Sales, J. & Homs, N. Bimetallic Silica-Supported Catalysts Based on Ni - Sn , Pd - Sn , and Pt - Sn as Materials in the CO Oxidation Reaction. *Chem. Mater.* **10,** 1333–1342 (1998).

22. Contreras-Andrade, I., Vazquez-Zavala, A. & Viveros, T. Influence of the Synthesis Method on the Catalytic Behaviour of Pt and PtSn/Al2O3 Reforming Catalyst. *Energy and Fuels* **23,** 3835–3841 (2009).

23. Liu, M. *et al.* Design of Highly Efficient Pt-SnO $_2$ Hydrogenation Nanocatalysts using Pt@Sn Core–Shell Nanoparticles. *ACS Catal.* **7,** 1583–1591 (2017).

24. Mazzieri, V. A., Grau, J. M., Yori, J. C., Vera, C. R. & Pieck, C. L. Influence of additives on the Pt metal activity of naphtha reforming catalysts. *Appl. Catal. A Gen.* **354,** 161–168 (2009).

25. Pei, Y. *et al.* Intermetallic structures with atomic precision for selective hydrogenation of nitroarenes. *J. Catal.* **356,** 307–314 (2017).

26. Shu, Y. *et al.* Bimetallic Pt-Sn nanoparticles on hydrogenated MoOx for the selective hydrogenation of functionalized nitroarenes. *ChemCatChem* **3,** 4199–4205 (2017).

27. Pritchard, J., Filonenko, G. A., van Putten, R., Hensen, E. J. M. & Pidko, E. A. Heterogeneous and homogeneous catalysis for the hydrogenation of carboxylic acid derivatives: history, advances and future directions. *Chem. Soc. Rev.* **44,** 3808–3833 (2015).

28. Yang, M.-L. *et al.* Tuning selectivity and stability in propane dehydrogenation by shaping Pt particles : A combined experimental and DFT study. *J. Mol. Catal. A Chem.* **395,** 329–336 (2014).

29. Cortright, R. D., Hill, J. M. & Dumesic, J. A. Selective dehydrogenation of isobutane over supported Pt/Sn catalysts. *Catal. Today* **55,** 213–223 (2000).

30. Stagg, S. M., Querini, C. A., Alvarez, W. E. & Resasco, D. E. Isobutane Dehydrogenation on Pt-Sn/SiO2 Catalysts: Effect of Preparation Variables and Regeneration Treatments. *J. Catal.* **94,** 75–94 (1997).

31. Yang, M.-L., Zhu, Y.-A., Zhou, X.-G., Sui, Z.-J. & Chen, D. First-Principles Calculations of Propane Dehydrogenation over PtSn Catalysts. *ACS Catal.* **2,** 1247–1258 (2012).

32. Wu, J., Peng, Z. & Bell, A. T. Effects of composition and metal particle size on ethane dehydrogenation over PtxSn100−x/Mg(Al)O (70...x...100). *J. Catal.* **311,** 161–168 (2014).

33. Llorca, J. *et al.* Supported Pt–Sn catalysts highly selective for isobutane dehydrogenation: preparation, characterization and catalytic behavior. *Appl. Catal. A Gen.* **189,** 77–86 (1999).

34. Becker, C. *et al.* Adsorption of Simple Alkenes on Pt (111) and Pt - Sn Surface Alloys : Bond Strength versus Heat of Adsorption. *J. Phys. Chem. C* **112,** 14693–14695 (2008).

35. Gomez-Quero, S. *et al.* Kinetics of propane dehydrogenation over Pt-Sn/Al2O3. *Catal. Sci. Technol.* **3,** 962–971 (2013).

36. Li, Q., Sui, Z., Zhou, X. & Chen, D. Applied Catalysis A : General Kinetics of propane dehydrogenation over Pt–Sn/Al2O3 catalyst. *Appl. Catal. A Gen.* **398,** 18–26 (2011).

37. Cortright, R. D., Levin, P. E. & Dumesic, J. A. Kinetic Studies of Isobutane Dehydrogenation and Isobutene Hydrogenation over Pt/Sn-Based Catalysts. *Ind. Eng. Chem. Res.* **37,** 1717–1723 (1998).

38. Xiong, H. *et al.* Thermally Stable and Regenerable Platinum – Tin Clusters for Propane Dehydrogenation Prepared by Atom Trapping on Ceria. *Angew. Chem. Int. Ed. Engl.* **56,** 1–7 (2017).

39. Lin, L., Zang, J. & Xu, Z. ENHANCEMENT OF THE STABILITY OF PtSn CATALYSTS IN REGENERATION CYCLES BY A1203 DOPING WITH RARE-EARTH OXIDES Cycle Number Cycle Number. in *10th International Congress on Catalysis* 2507–2510 (1993).

40. Prakash, N., Lee, M. H., Yoon, S. & Jung, K. D. Role of acid solvent to prepare highly active PtSn/θ-Al2O3 catalysts in dehydrogenation of propane to propylene. *Catal. Today* **293–294,** 33–41 (2017).

41. Deng, L., Shishido, T., Teramura, K. & Tanaka, T. Effect of reduction method on the activity of Pt–Sn /SiO2 for dehydrogenation of propane. *Catal. Today* **232,** 33–39 (2014).

42. Ping, E. W. *et al.* On the nature of the deactivation of supported palladium nanoparticle catalysts in the decarboxylation of fatty acids. *Appl. Catal. A Gen.* **396,** 85–90 (2011).

43. Zhang, Y. *et al.* Comparative study of bimetallic Pt-Sn catalysts supported on different supports for propane dehydrogenation. *J. Mol. Catal. A Chem.* **381,** 138–147 (2014).

44. Merlen, E., Beccat, P., Bertolini, J. C. & Delich, P. Characterization of Bimetallic Pt – Sn / Al 2 O 3 Catalysts : Relationship between Particle Size and Structure. *J. Catal.* **159,** 178–188 (1996).

45. Srinivasan, R., De Angelis, R. J. & Davis, B. H. Alloy formation in Pt-Sn-alumina catalysts: In situ X-ray diffraction study. *J. Catal.* **106,** 449–457 (1987).

46. Balakrishnan, K. & Schwank, J. FTIR Study of Bimetallic Pt-Sn / AI203 Catalysts. *J. Catal.* **138,** 491–499 (1992).

47. Zhu, J. *et al.* Size-Dependent Reaction Mechanism and Kinetics for Propane Dehydrogenation

over Pt Catalysts. *ACS Catal.* **5,** 6310–6319 (2015).

48. Zhang, S. *et al.* Tuning Nanoparticle Structure and Surface Strain for Catalysis Optimization. *J. Am. Chem. Soc.* **136,** 7734–7739 (2014).

49. Baranova, E. A. *et al.* Single-step polyol synthesis of alloy Pt7Sn3 versus bi-phase Pt/SnOx nano-catalysts of controlled size for ethanol electro-oxidation. *J. Appl. Electrochem.* **40,** 1767–1777 (2010).

50. Cho, H. & Regalbuto, J. R. The rational synthesis of Pt-Pd bimetallic catalysts by electrostatic adsorption. *Catal. Today* **246,** 143–153 (2015).

51. Lopez-Ruiz, J. A., Pham, H. N., Datye, A. K. & Davis, R. J. Reactivity and stability of supported Pd nanoparticles during the liquid-phase and gas-phase decarbonylation of heptanoic acid. *Appl. Catal. A Gen.* **504,** 295–307 (2015).

52. Maligal-Ganesh, R. V. *et al.* A Ship-in-a-Bottle Strategy to Synthesize Encapsulated Intermetallic Nanoparticle Catalysts: Exemplified for Furfural Hydrogenation. *ACS Catal.* **6,** 1754–1763 (2016).

53. Xie, J., Falcone, D. D. & Davis, R. J. Restructuring of supported PtSn bimetallic catalysts during aqueous phase oxidation of 1 , 6-hexanediol. *J. Catal.* **332,** 38–50 (2015).

54. Serrano-Ruiz, J. C., Sepúlveda-Escribano, A. & Rodríguez-Reinoso, F. Bimetallic PtSn/C catalysts promoted by ceria: Application in the nonoxidative dehydrogenation of isobutane. *J. Catal.* **246,** 158–165 (2007).

55. Carvalho, L. S. *et al.* Trimetallic naphtha reforming catalysts I. Properties of the acid function and influence of the order of addition of the metallic precursors on Pt-Re-Sn/γ-Al2O3-Cl. *Appl. Catal. A Gen.* **269,** 105–116 (2004).

56. Carvalho, L. S. *et al.* Trimetallic naphtha reforming catalysts II. Properties of the acid function and influence of the order of addition of the metallic precursors on Pt-Re-Sn/γ-Al2O3-Cl. *Appl. Catal. A Gen.* **269,** 105–116 (2004).

57. Yin, M. *et al.* Effect of alumina support on catalytic performance of Pt-Sn/Al2O3 catalysts in one-step synthesis of N-phenylbenzylamine from aniline and benzyl alcohol. *Chinese J. Catal.* **34,** 1534–1542 (2013).

58. Cheng, H., Chen, L., Cooper, A. C., Sha, X. & Pez, G. P. Hydrogen spillover in the context of hydrogen storage using solid-state materials. *Energy Environ. Sci.* **1,** 338 (2008).

59. Salmones, J., Wang, J. A., Galicia, J. A. & Aguilar-Rios, G. H2 reduction behaviors and catalytic performance of bimetallic tin-modified platinum catalysts for propane dehydrogenation. *J. Mol. Catal. A Chem.* **184,** 203–213 (2002).

60. Shan, Y., Sui, Z., Zhu, Y., Chen, D. & Zhou, X. Effect of steam addition on the structure and activity of Pt – Sn catalysts in propane dehydrogenation. *Chem. Eng. J.* **278,** 240–248 (2015).

61. Sheintuch, M., Liron, O., Ricca, A. & Palma, V. Propane dehydrogenation kinetics on supported Pt catalyst. *Appl. Catal. A Gen.* **516,** 17–29 (2016).

62. Hill, J. M., Cortright, R. D. & Dumesic, J. A. Silica- and L-zeolite-supported Pt , Pt/Sn and Pt/Sn/K

catalysts for isobutane dehydrogenation. *Appl. Catal. A Gen.* **168,** 9–21 (1998).

63. Barias, O. A., Holmen, A. & Blekkan, E. A. Propane Dehydrogenation over Supported Pt and Pt–Sn Catalysts: Catalyst Preparation, Characterization, and Activity Measurements. *J. Catal.* **158,** 1–12 (1996).

64. Verbeek, H. & Sachtler, W. M. H. The study of the alloys of platinum and tin by chemisorption. *J. Catal.* **42,** 257–267 (1976).

65. Freakley, S. J. *et al.* Palladium-tin catalysts for the direct synthesis of H 2 O 2 with high selectivity. *Science (80-.).* **351,** 965–968 (2016).

66. De Miguel, S. R., Baronetti, G. T., Castro, A. A. & Scelza, O. A. Platinum-Tin / Alumina Catalyst: Modification of the Metallic Phase after successive Oxidation- Reduction Cycles. *Appl. Catal.* **45,** 61–69 (1988).

67. Wang, X. *et al.* Colloidal Synthesis and Structural Control of PtSn Bimetallic Nanoparticles. *Langmuir* **27,** 11052–11061 (2011).

4. Conclusion and future work

4.1. Concluding remarks

The influence of Sn promoter on Pd and Pt catalysts was explored utilizing two probe reactions. The first probe reaction was the conversion of heptanoic acid over supported Pd and Pd-Sn catalysts. The second probe reaction was the conversion of propane over Pt and Pt-Sn catalysts. The goal was to elucidate the role of Sn as a promoter in the presence of oxygenated species and in a high temperature reducing environment.

The conversion of heptanoic acid over supported Pd catalysts resulted in rapid deactivation and poor selectivity to the α-olefin product. The rate of deactivation of monometallic Pd/SiO_2 was reduced by decreasing the Pd nanoparticle size through an ion exchange synthesize technique. The improved stability was attributed to a lower turnover frequency which was approximately 50% of that over nanoparticles 2 times larger. However, the reaction path remained unchanged over the more stable nanoparticles and no improvement to the selectivity of α-olefin products was observed.

The Pd/SiO_2 catalyst was further stabilized upon the addition of Sn. Catalyst containing chemically mixed Pd-Sn (both metal precursors added to the same support) and catalyst containing a physical mixture of Pd-Sn (Pd/SiO_2 + Sn/SiO_2 mixed until uniform) resulted in stable conversion of heptanoic acid over 10.75 h. The addition of Sn expanded the reaction path to include hydrogenation and decarboxylative ketonization products. The hydrogenation product, heptanal, was the major product over both the chemically and physically mixed catalysts. Tin was found to be mobile in the presence of the oxygenated species, resulting in the deposition of Sn species on or around Pd nanoparticles in the physical mixture. A two-stage reactor configuration containing Pd/SiO_2 and Sn/SiO_2 separated by quartz wool indicated that the improved stability of Pd/SiO_2 and the expansion of the reaction path to include hydrogenation required Pd and Sn to have intimate contact through a physical or chemical mixture. X-Ray absorption near edge structure (XANES) was used to probe the oxidation state of Sn under reaction conditions. Both Pd-Sn catalysts contained partially reduced SnO_x species under reaction conditions.

A brief summary of the possible sites responsible for the product distribution over $PdSn/SiO_2$ is shown in Figure 4.1.

1. The decarbonylation path occurs on the exposed Pd sites. Tin on its own could not produce olefin products.
2. Hydrogenation of carboxylic acids to aldehydes is possible on partially reduced metal oxides which were present on the bimetallic catalysts under reaction conditions.
3. A key factor in maintaining the hydrogenation activity on SnO_x sites is the availability of H_2. The %CO in the product stream was lower than expected over both Pd-Sn catalysts, which suggests that the water-gas shift is occurring and producing H_2. This likely occurs on exposed Pd sites.
4. Dehydrogenation of alkanes has been reported on Pd and Pd-Sn catalysts.[1] The dehydrogenation of olefins is therefore speculated to take place on Pd sites or Pd-Sn alloy sites that may exist at the interface of Pd and SnO_x surface species.
5. Decarboxylative ketonization of carboxylic acids to ketones can proceed on metal oxides without the presence of H_2. The sites responsible for producing the observed ketonization products may be SnO_x species that are relatively far from Pd sites and are unable to be reached by H_2 spillover. Alternatively, a reactive intermediate may form on SnO_x sites that can then react over Pd to form 7-tridecanone, similar to what is believed to occur when Pd and Sn are separated by quartz wool in the two stage reactor configuration.

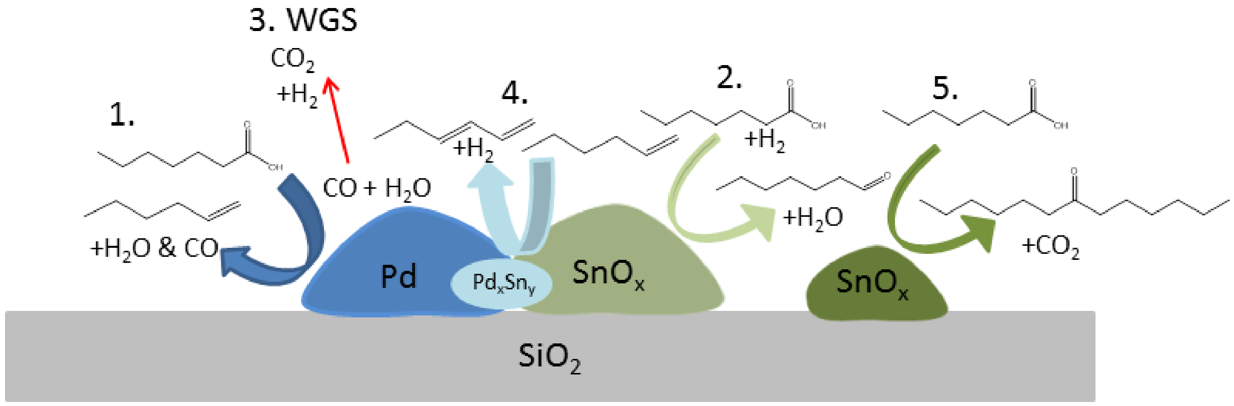

Figure 4.1: Illustration of heptanoic acid conversion over Pd-Sn/SiO_2.

In contrast to the heptanoic acid study, the high temperature reducing conditions in the absence of oxygenated species allowed for Pt-Sn alloys to form. Silica-supported Pt-Sn catalysts exhibited improved stability compared to Pt/SiO_2. The relative stability improved with increasing Sn content although a subsequent decrease in activity was observed. For example, 1Pt2.4Sn/SiO_2 was more stable than 1Pt1.2Sn/SiO_2 but was an order of magnitude less active at a 2% initial conversion (0.014 versus 0.13 $mol_{propane}\ g_{cat}^{-1}\ h^{-1}$, respectively). The improved stability over Pt-Sn alloys can be partially attributed to electronic effects arising from the donation of electronic charge from Sn to Pt. The barrier for dissociative adsorption of propane increases with incorporation of Sn into Pt and reduces the activity of the catalyst as this adsorption step is believed to be rate determining. These Pt-Sn alloys decrease the barrier for desorption of propene which reduces the surface coverage of this dehydrogenated species leading to a reduced rate of deep dehydrogenation and coke formation.

Alumina-supported Pt-Sn catalysts did not exhibit improved stability compared to unpromoted Pt at relatively low levels of Sn promotion (0.2 to 1.2 wt% Sn). Tin is known to have a strong interaction with alumina which stabilizes it in an oxidized state. The majority of Sn on Pt-Sn/Al_2O_3 catalysts likely resides at the interface between Pt and Al_2O_3 as SnO_x.

Oxidative regeneration of Pt-Sn catalysts was possible on Al_2O_3 but not on SiO_2. An irreversible loss of activity occurred when Pt-Sn/SiO_2 was treated in synthetic air to remove coke from the catalyst surface. The silica-supported Pt-Sn catalysts experienced de-alloying due to exposure to oxidizing conditions, similar to what was observed during the study of Pd-Sn catalysts for heptanoic acid conversion. Even preforming bimetallic Pt-Sn nanoparticles through a polyol synthesis method could not stabilize Pt-Sn/SiO_2 during oxidative treatments. The performance of Pt-Sn catalysts during propane dehydrogenation was ultimately correlated with the interaction of metals with the support material.

4.2 Future work

4.2.1. Low energy ion scattering

Significant gaps remain in our understanding of the surface composition of the silica- and alumina-supported Pt-Sn catalysts described in this dissertation. Low energy ion scattering (LEIS) is a characterization technique that probes the elemental composition of the outermost atomic layer of a material.[2] Characterization techniques capable of probing the outermost layers of nanoparticles may reveal greater insight into the observed differences of Pt-Sn/SiO_2 and Pt-Sn/Al_2O_3, particularly with regards to the chemisorption results. The LEIS technique can also elucidate the differences between the polyol- and IWI-synthesized 1Pt0.6Sn/SiO_2 that may give rise to the discrepancy in activity observed on the two catalysts.

4.2.2. Ceria-promoted Pt dehydrogenation catalysts

Oxidative regeneration of deactivated catalysts remains a key obstacle in commercializing Pt-Sn/SiO_2 which has been demonstrated to exhibit improved stability compared to analogous catalysts supported on alumina. A more mild oxidative regeneration may be possible by promoting Pt-Sn/SiO_2 with Ce which has been demonstrated to lower the temperature required for the catalytic oxidation of coke.[3] Ceria is also known to interact with PtO_x species, which can form during high temperature oxidative treatments, and can reduce the extent of Pt sintering.[4]

4.2.3 Synthesis of encapsulated nanoparticles

Our initial efforts to synthesize monodisperse Pt-Sn nanoparticles with well-defined composition utilized strong capping agents to maintain a narrow particle size distribution. Mild oxidative treatments were unable to adequately remove the capping agents and resulted in no catalytic activity. Oxidative treatments at higher temperatures were not explored due to the possible phase segregation of Pt and Sn. One possible way forward would be to encapsulate the pre-formed Pt-Sn nanoparticles with a porous layer of silica, known as the ship-in-a-bottle synthesis. Maligal-Ganesh et al. successfully applied this technique to a variety of Pt-Metal bimetallic catalysts, including Pt-Sn, Pt-Zn, and Pt-Pb (Figure 4.2).[5] By encapsulating the nanoparticles in mesoporous silica, high temperature oxidative treatment at 773 K was successfully utilized to remove capping agents and coke without a significant migration of Sn. The well-defined Pt-Sn alloy was reformed through a mild reductive treatment at 573 K. A full recovery of activity of Pt-Sn particles encapsulated by mesoporous silica was demonstrated following oxidative removal of coke deposited during furfural hydrogenation.[5]

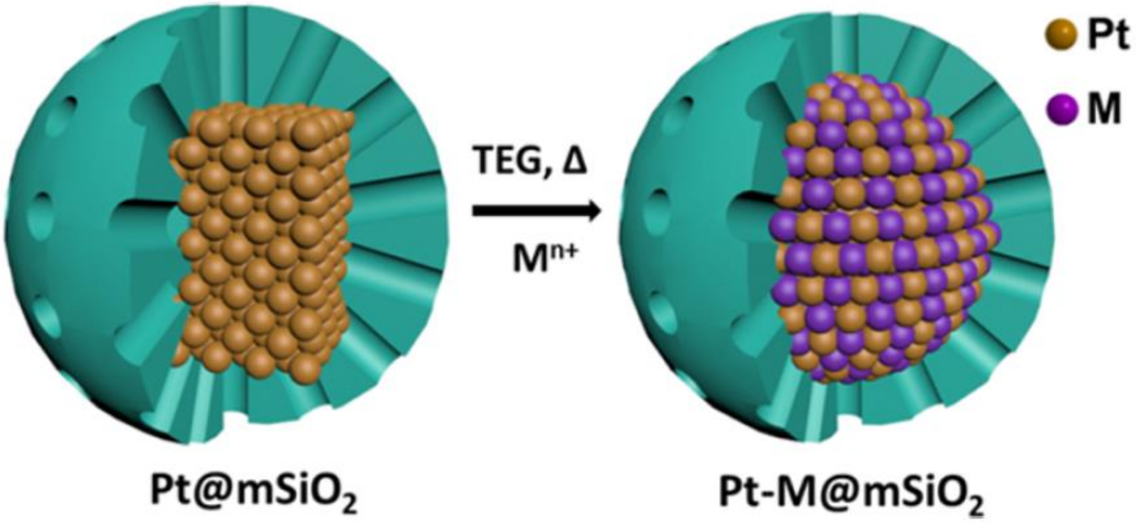

Figure 4.2: Schematic is shown for the ship-in-a-bottle synthesis of intermetallic NP using a mesoporous silica-shell enclosure in a solvent-reducing agent such as tetraethylene glycol. M^{n+} is the metal precursor, e.g., Sn^{2+} from $SnCl_2 \bullet 2H_2O$.[5] Maligal-Ganesh, R. V. *et al.* A Ship-in-a-Bottle Strategy to Synthesize Encapsulated Intermetallic Nanoparticle Catalysts: Exemplified for Furfural Hydrogenation. *ACS Catal.* **6,** 1754–1763 (2016). Copyright 2016, American Chemical Society.

The ship-in-a-bottle synthesis technique is not without its drawbacks. The silica-encapsulated Pt-Sn nanoparticles are in the range of 20-30 nm and thus require some form of support in order to be used successfully in a flow system. Quartz sand is one possible material that can be used to support the encapsulated nanoparticles for use in gas-phase flow reactors.

4.2.4 Shape control of nanoparticles

Colloidal synthesis methods can be used to produce well-defined nanoparticle shapes that allow for the exposure of specific lattice faces.[6–8] Figure 4.3 shows Pt nanoparticles with a cubic structure exposing only the Pt (100) lattice and an octahedral structure exposing only the Pt (111) lattice.[9] Yang et al. demonstrated through experiment and computational studies that Pt (111) lattices can improve the selectivity towards propene due to its weakened binding strength of propene and increased barrier for C-H bond cleavage in propene dehydrogenation compared to Pt (100) surfaces.[9] Such a level of control could be utilized in the optimization of bimetallic catalysts for a variety of applications, including the dehydrogenation of light alkanes over Pt-Sn catalysts.

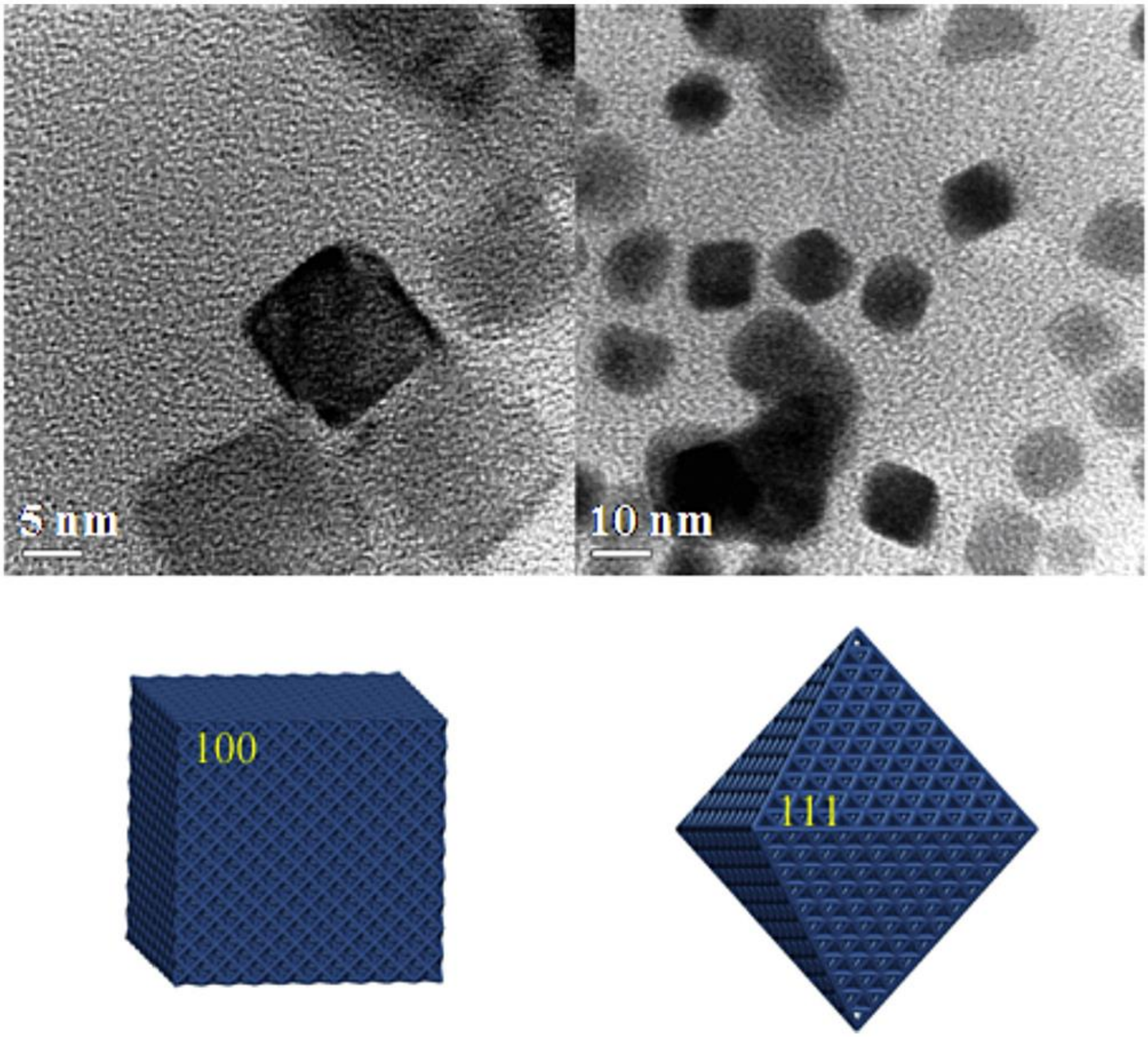

Figure 4.3: Pt nanoparticles of different shapes: cubic 11.5nm (upper left) and octahedral 12 nm (upper right). The bottom two geometries are ideal cubic and octahedral models.[9] Reprinted from Journal of Molecular Catalysis A: Chemical, 395, Ming-Lei Yang,Jun Zhu,Yi-An Zhu,Zhi-Jun Sui,Ying-Da Yu,Xing-Gui Zhou,De Chen, Tuning selectivity and stability in propane dehydrogenation by shaping Pt particles: A combined experimental and DFT study, Copyright 2014, with permission from Elsevier.

4.2.5 Alternatives to Pt group catalysts

Recently, Xie et al. demonstrated that Co-N-C catalysts were active for the dehydrogenation of propane to propene, exhibiting activity about one order of magnitude lower than Pt/SiO_2.[10] Deactivation of Co-N-C catalysts during propane conversion likely occurred due to coke formation, similar to Pt-based catalysts. Ion-exchanged Co/SiO_2 was also active for the dehydrogenation of propane. These Co/SiO_2

catalysts were two orders of magnitude lower in activity compared to Pt/SiO_2 but they offer a critical advantage over Co-N-C: silica-supported Co can be oxidatively regenerated without altering the structure of the catalyst or support material. Similar oxidative regeneration treatments cannot be used with carbon-supported catalysts. Silica-supported Co catalysts may be explored for further optimization of activity, perhaps through promotion with a second metal.

Both classes of Co catalysts offer interesting alternative catalytic materials for use in the reactions that traditionally utilize Pt group catalysts. It may be worth testing their behavior in the conversion of biomass-derived molecules, such as carboxylic acids, due to their Pt-like activity but at a significantly reduced cost. Additionally, atomically-dispersed Co/SiO_2 in particular contains fewer possible active sites compared to Pd-Sn/SiO_2. This may limit the possible reaction paths during the conversion of carboxylic acids.

4.3. References for Chapter 4

1. Masai, M., Honda, K., Kubota, A. & Ohnaka, S. Dehydrogenation and hydrogenation activity of palladium-tin-silica and nickel-tin-silica. *J. Catal.* **50,** 419–428 (1977).

2. Cushman, C. V. *et al.* Low energy ion scattering (LEIS). A practical introduction to its theory, instrumentation, and applications. *Anal. Methods* **8,** 3419–3439 (2016).

3. Yin, K. *et al.* Catalytic Oxidation of Solid Carbon and Carbon Monoxide over Cerium-Zirconium Mixed Oxides. *AIChE J.* **63,** 725–738 (2017).

4. Sattler, J. J. H. B., Ruiz-Martinez, J., Santillan-Jimenez, E. & Weckhuysen, B. M. Catalytic Dehydrogenation of Light Alkanes on Metals and Metal Oxides. *Chem. Rev.* **114,** 10613–10653 (2014).

5. Maligal-Ganesh, R. V. *et al.* A Ship-in-a-Bottle Strategy to Synthesize Encapsulated Intermetallic Nanoparticle Catalysts: Exemplified for Furfural Hydrogenation. *ACS Catal.* **6,** 1754–1763 (2016).

6. Herricks, T., Chen, J. & Xia, Y. Polyol Synthesis of Platinum Nanoparticles : Control of Morphology with Sodium Nitrate Polyol Synthesis of Platinum Nanoparticles : Control of Morphology with Sodium Nitrate. (2004). doi:10.1021/nl048570a

7. Tao, F. *et al.* Evolution of Structure and Chemistry of Bimetallic Nanoparticle Catalysts under Reaction Conditions. *J. Am. Chem. Soc.* 8697–8703 (2010).

8. Tao, F. (Feng). Synthesis , catalysis , surface chemistry and structure of bimetallic nanocatalysts. *Chem. Soc. Rev.* **41,** 7977–7979 (2012).

9. Yang, M.-L. *et al.* Tuning selectivity and stability in propane dehydrogenation by shaping Pt particles : A combined experimental and DFT study. *J. Mol. Catal. A Chem.* **395,** 329–336 (2014).

10. Xie, J. *et al.* Atomically Dispersed Co and Cu on N - Doped Carbon for Reactions Involving C – H Activation. *ACS Catal.* **8,** 3875–3884 (2018).

Appendix A:

Supplemental materials for Chapter 2

Vapor Phase Deoxygenation of Heptanoic Acid over Silica Supported Palladium and Palladium-Tin Catalysts

*This section is adapted from a manuscript that was published in Journal of Catalysis, Volume 344 of December 2016, on pages 202-212.

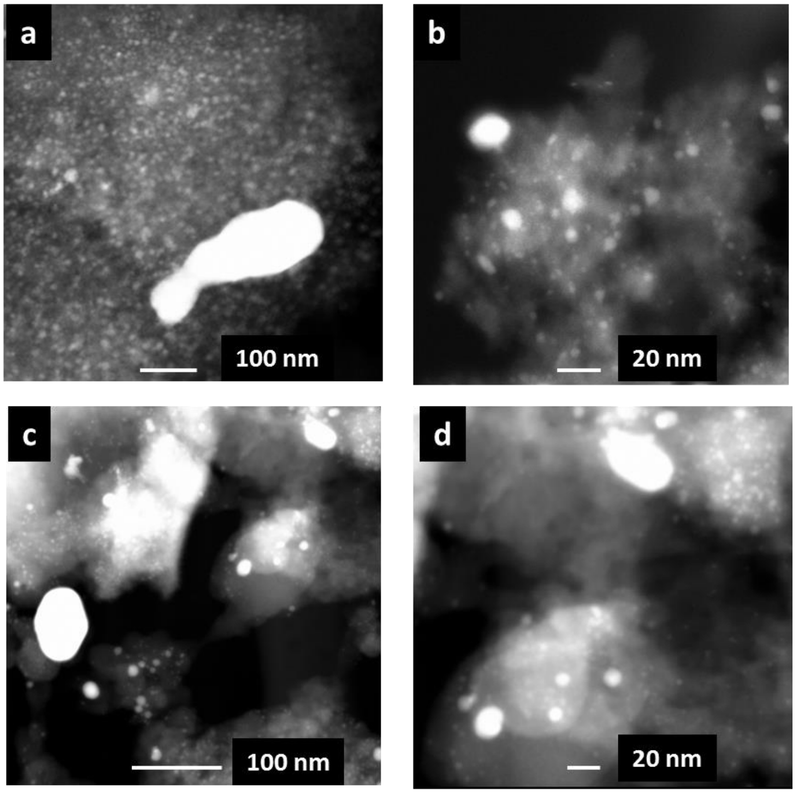

Figure A1: STEM image of fresh [(a) and (b)] and used [(c) and (d)] PdSn/SiO_2-C. Used catalyst was tested for heptanoic acid conversion at 573 K and 0.1 MPa for 10.75 h.

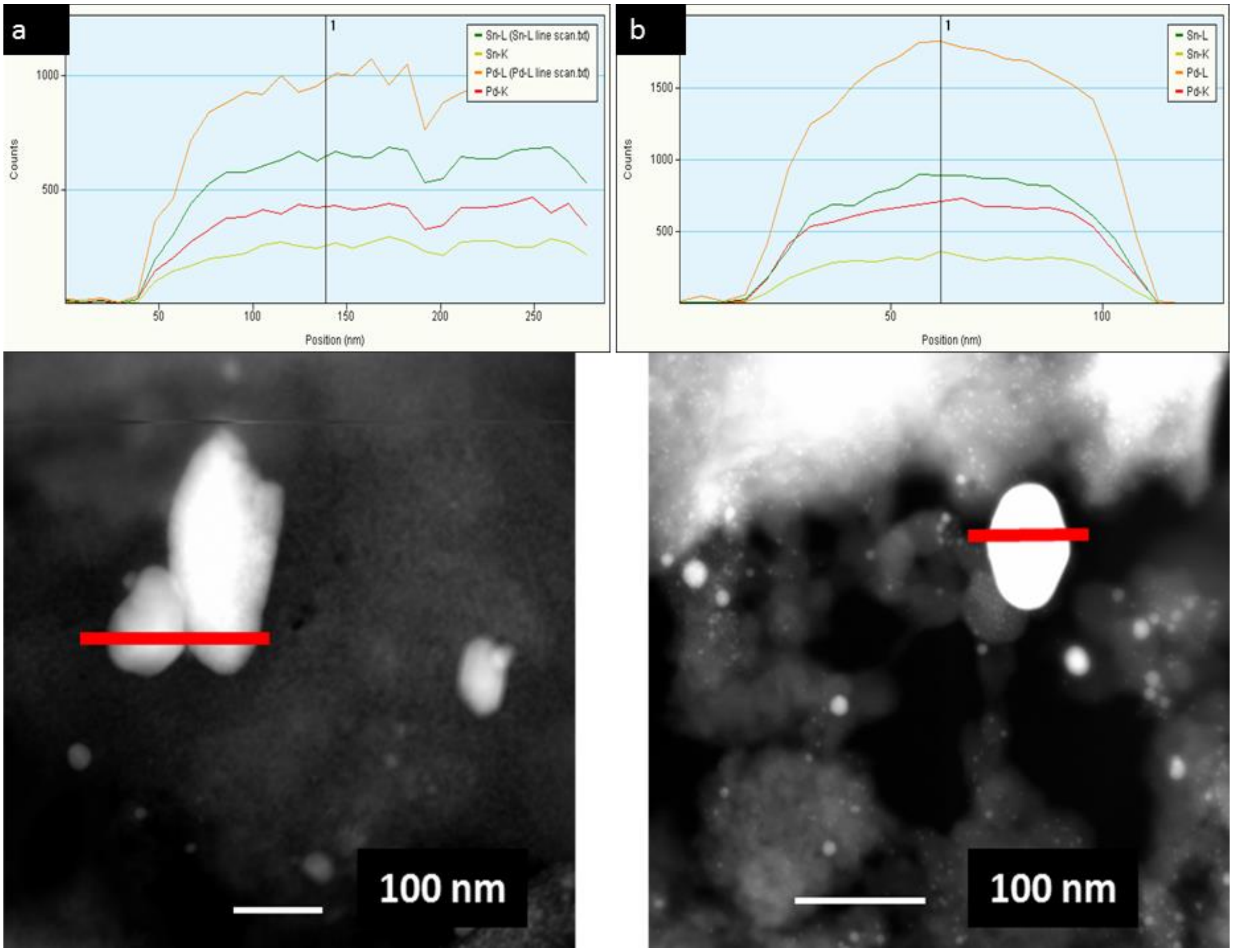

Figure A2: STEM-EDS line scan of large nanoparticles found on a) fresh and b) used PdSn/SiO_2-C. Used catalyst was tested for heptanoic acid conversion at 573 K and 0.1 MPa for 10.75 h.

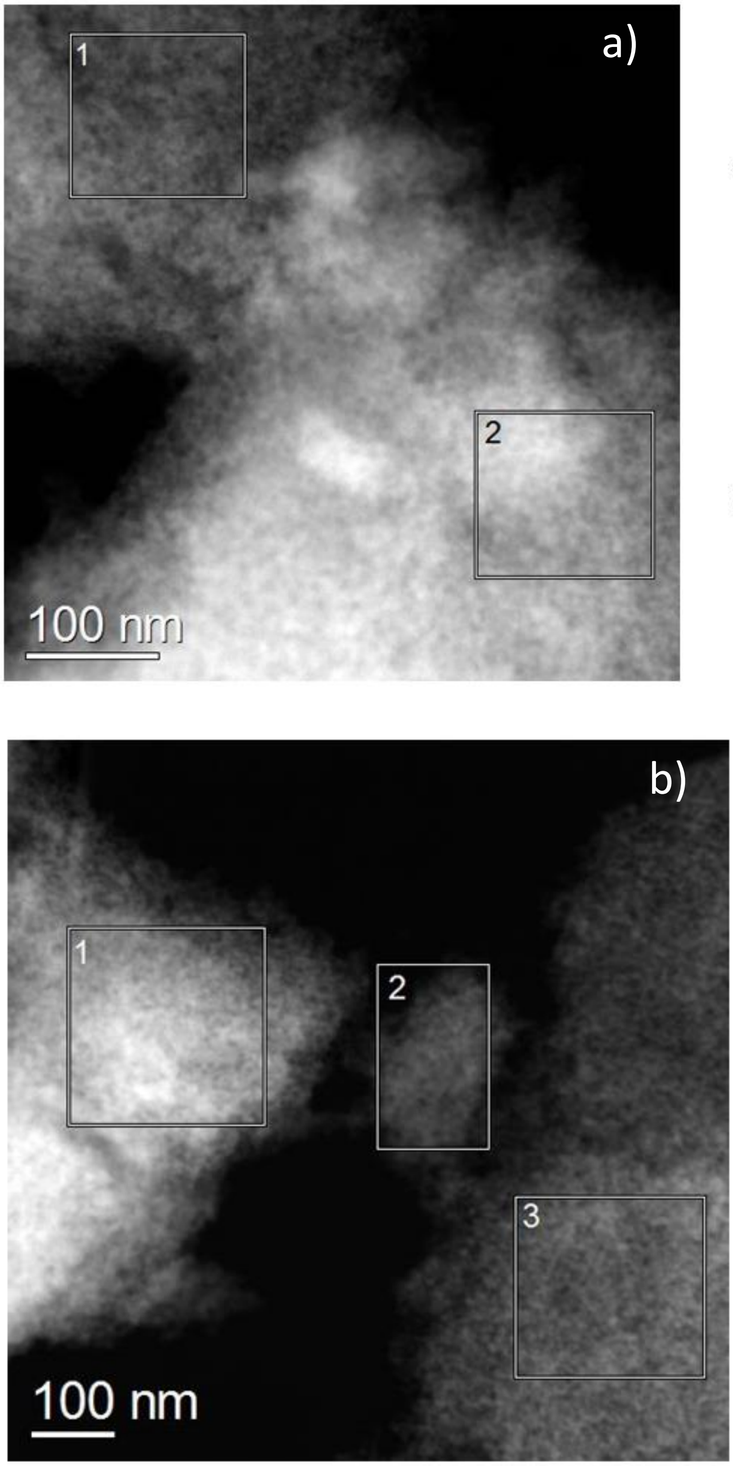

1

Element	Weight%	σ	Atomic%
O	61.4	1.5	75.5
Si	33.7	1.3	23.6
Pd	5.0	0.8	0.9

2

Element	Weight%	σ	Atomic%
O	59.0	1.1	73.1
Si	37.1	1.1	26.2
Pd	3.9	0.6	0.7

1

Element	Weight%	σ	Atomic%
O	67.5	0.5	78.8
Si	31.7	0.5	21.1
Sn	0.8	0.1	0.1

2

Element	Weight%	σ	Atomic%
O	68.8	1.2	80.1
Si	29.7	1.1	19.7
Sn	1.5	0.5	0.2

3

Element	Weight%	σ	Atomic%
O	67.5	0.9	79.3
Si	30.4	0.9	20.3
Sn	2.1	0.4	0.3

Figure A3: Elemental compositions of selected a) Pd-rich regions and b) Sn-rich regions in a fresh sample of PdSn/SiO_2-P.

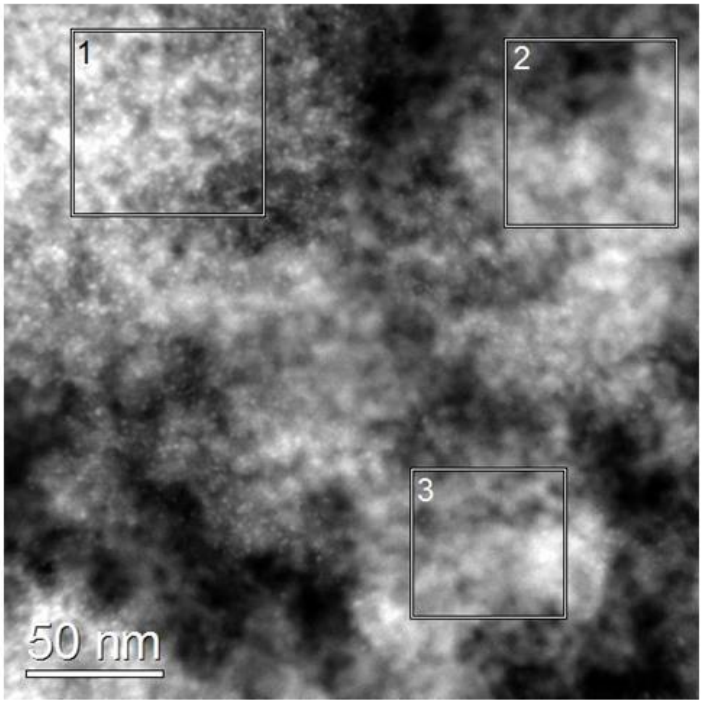

1

Element	Weight%	σ	Atomic%
O	40.0	1.1	56.1
Si	53.0	1.1	42.4
Sn	2.8	0.6	0.5
Pd	4.2	0.8	0.9

2

Element	Weight%	σ	Atomic%
O	43.8	1.4	59.2
Si	51.9	1.4	40.0
Sn	2.3	0.7	0.4
Pd	2.0	0.8	0.4

3

Element	Weight%	σ	Atomic%
O	40.5	1.3	56.6
Si	53.0	1.3	42.1
Sn	3.9	0.8	0.7
Pd	2.6	0.7	0.5

Figure A4: Elemental compositions of selected regions in used PdSn/SiO_2-P. Used catalyst was tested for heptanoic acid conversion at 573 K and 0.1 MPa for 10.75 h.

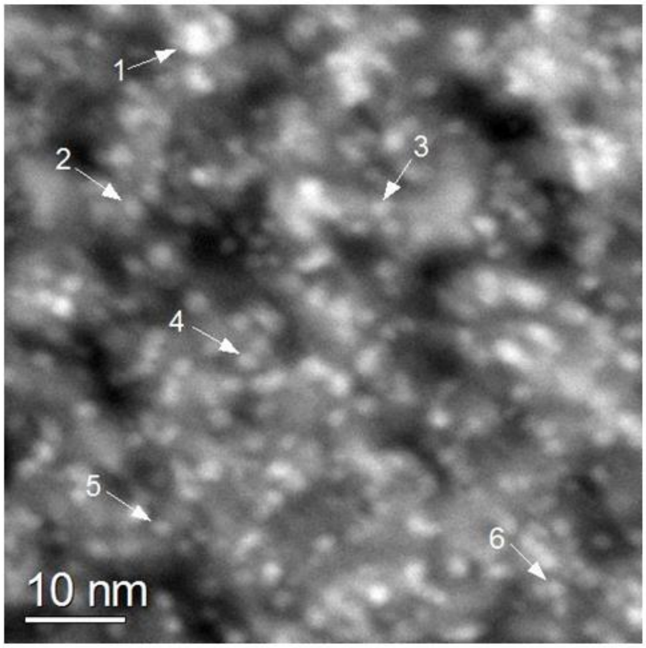

1

Element	Weight%	σ	Atomic%
O	26.1	2.1	46.1
Si	46.6	2.2	46.9
Sn	6.9	1.5	1.6
Pd	20.4	2.3	5.4

2

Element	Weight%	σ	Atomic%
O	18.5	1.8	41.2
Si	34.6	2.0	43.7
Sn	15.1	2.0	4.5
Pd	31.7	2.7	10.6

3

Element	Weight%	σ	Atomic%
O	26.7	1.9	46.8
Si	46.5	2.0	46.3
Sn	7.2	1.5	1.7
Pd	19.6	2.2	5.2

4

Element	Weight%	σ	Atomic%
O	22.7	1.8	44.7
Si	39.7	1.9	44.5
Sn	10.4	1.5	2.7
Pd	27.1	2.4	8.0

5

Element	Weight%	σ	Atomic%
O	25.6	1.6	44.7
Si	48.8	1.8	48.6
Sn	3.9	1.1	0.9
Pd	21.8	1.9	5.7

6

Element	Weight%	σ	Atomic%
O	25.7	2.4	49.1
Si	37.2	2.5	40.5
Sn	7.2	2.1	1.9
Pd	29.8	3.1	8.6

Figure A5: Elemental compositions of individual particles in a used sample of PdSn/SiO_2-P. Used catalyst was tested for heptanoic acid conversion at 573 K and 0.1 MPa for 10.75 h.

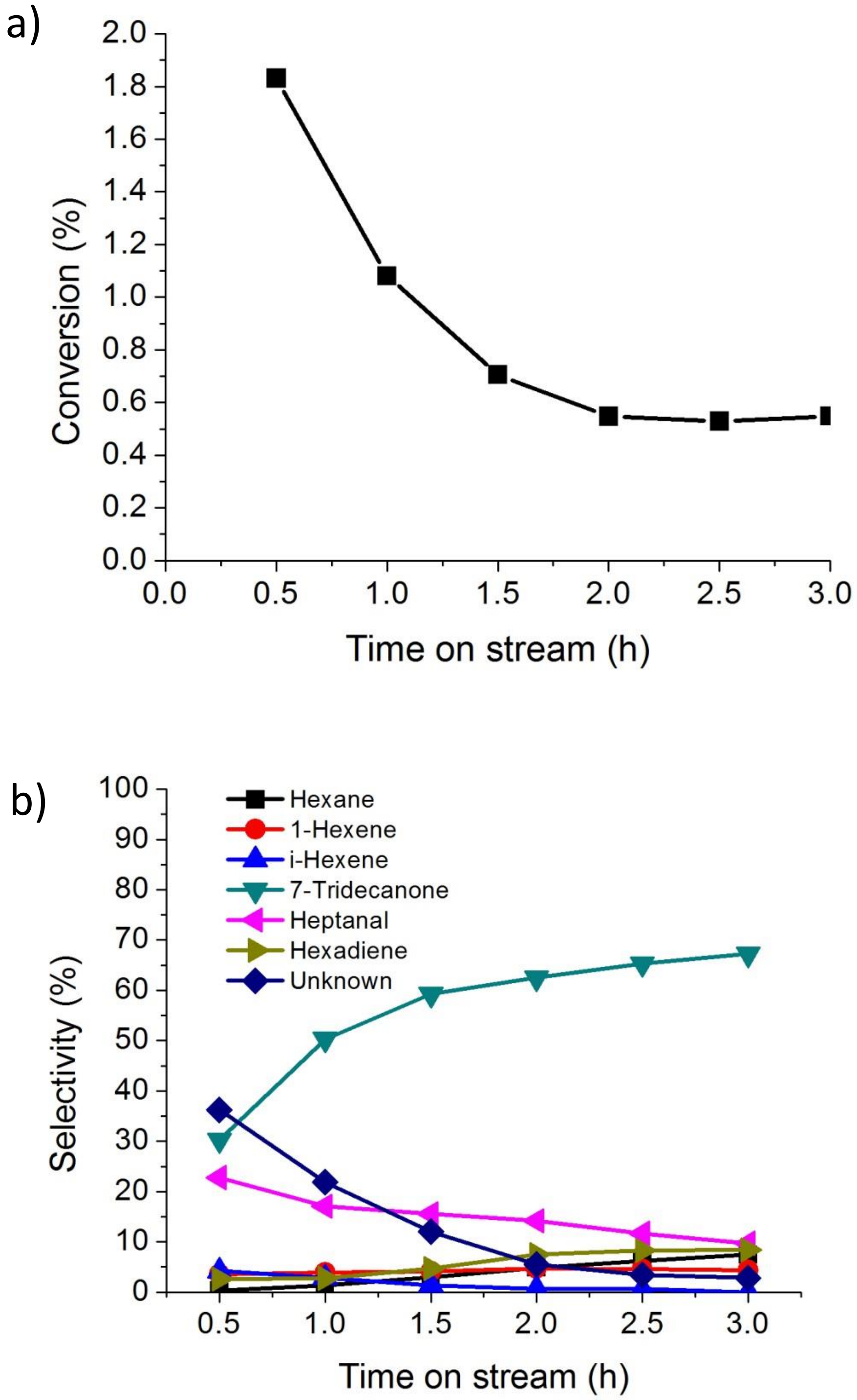

Figure A6: a) Conversion of heptanoic acid at 573 K and 0.1 MPa over Sn/SiO_2 and b) Selectivity to deoxygenation products over Sn/SiO_2.

Appendix B:

Supplemental materials for Chapter 3

Propane Dehydrogenation over Supported Pt-Sn Nanoparticles

*This section is adapted from a manuscript submitted to Journal of Catalysis in June 2018.

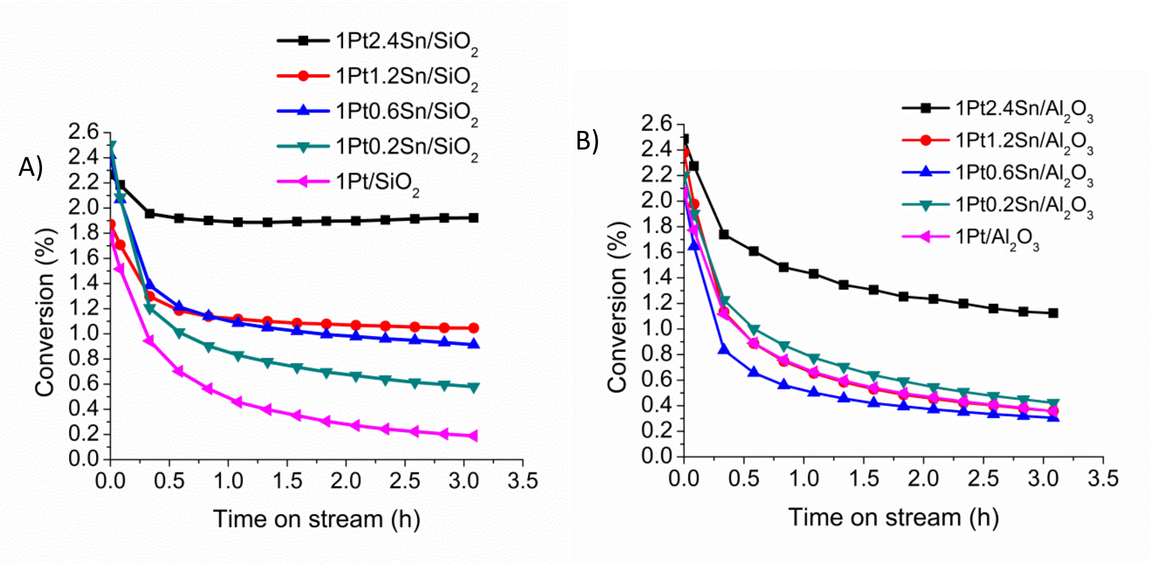

Figure B1: Conversion of propane at 773 K and 0.1 MPa total pressure (N_2:propane = 3:1) over A) SiO_2- and B) Al_2O_3-supported Pt and PtSn catalysts. Flow rates and catalyst loadings were varied to target a 2% initial conversion.

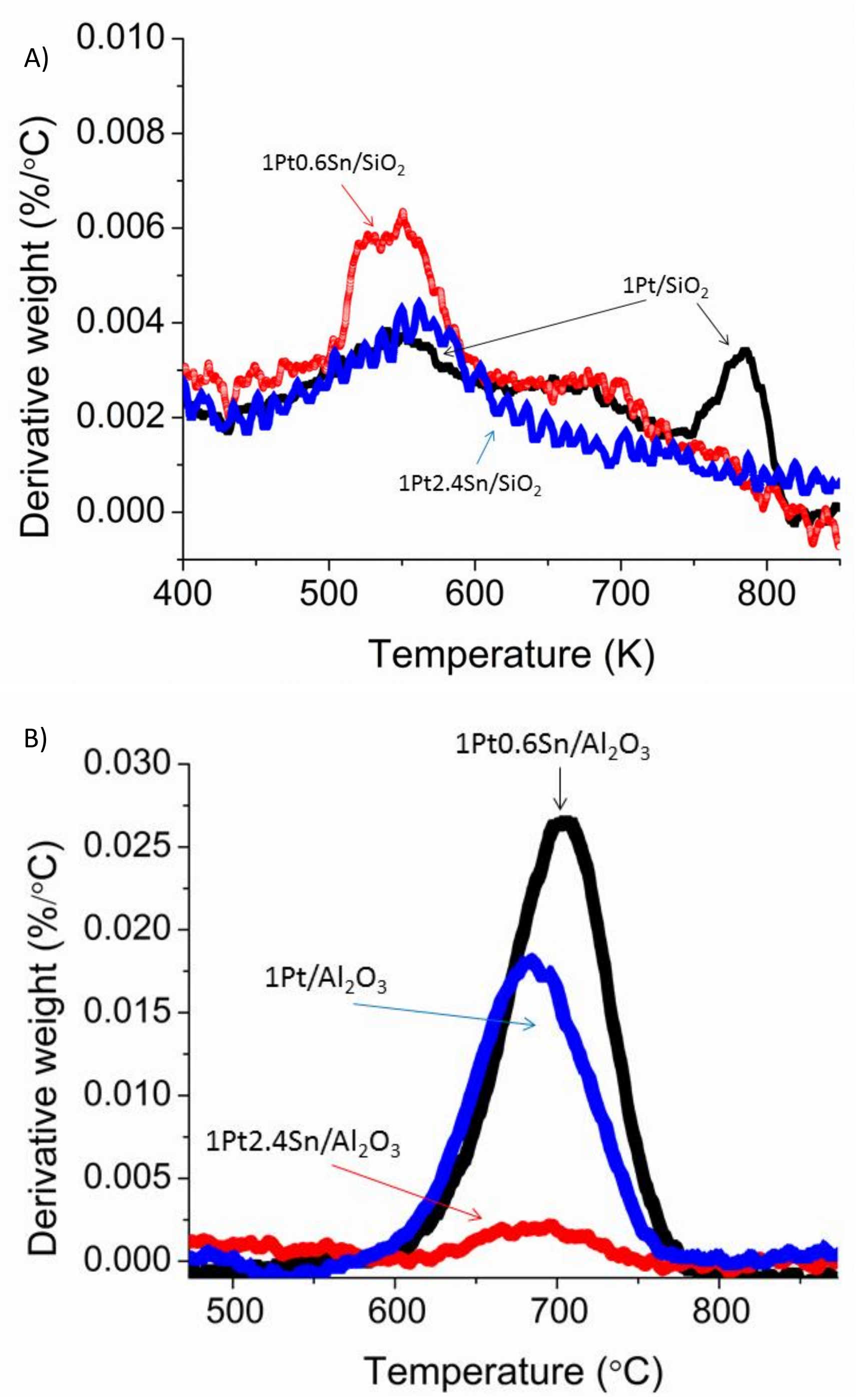

Figure B2: Temperature-programmed oxidation of coke on used A) SiO_2- and B) Al_2O_3-supported catalysts. The SiO_2-supported catalysts were treated at a ramp rate of 20 K min^{-1} and the Al_2O_3-supported catalysts were treated at a ramp rate of 10 K min^{-1}. The flow rate of 20.7% O_2/He was 100 cm^3 min^{-1}.

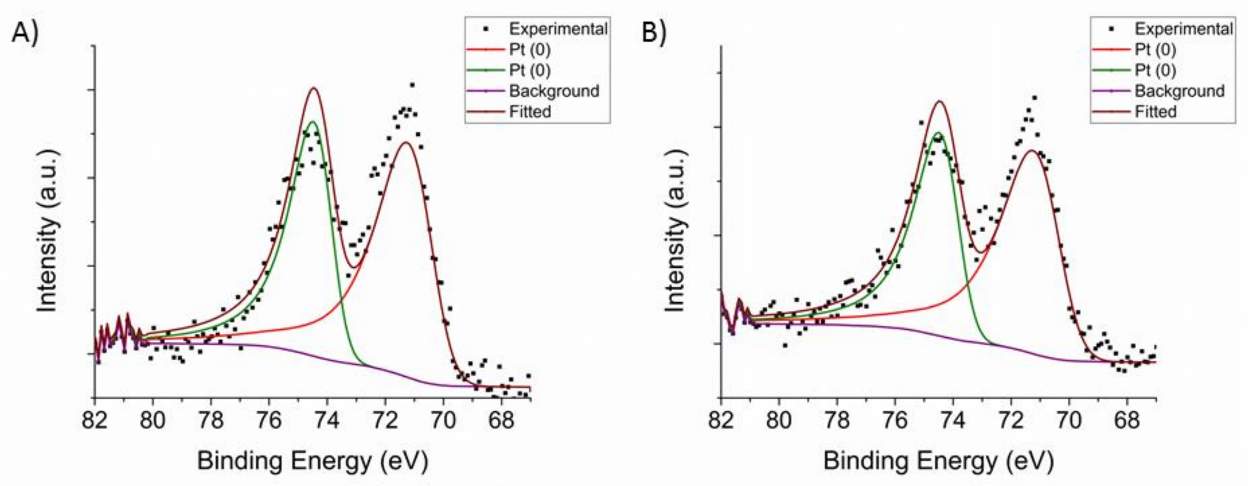

Figure B3: Pt $4f_{7/2}$ photoemission spectra of on A) fresh and B) regenerated and re-reduced 1Pt0.6Sn/SiO_2.

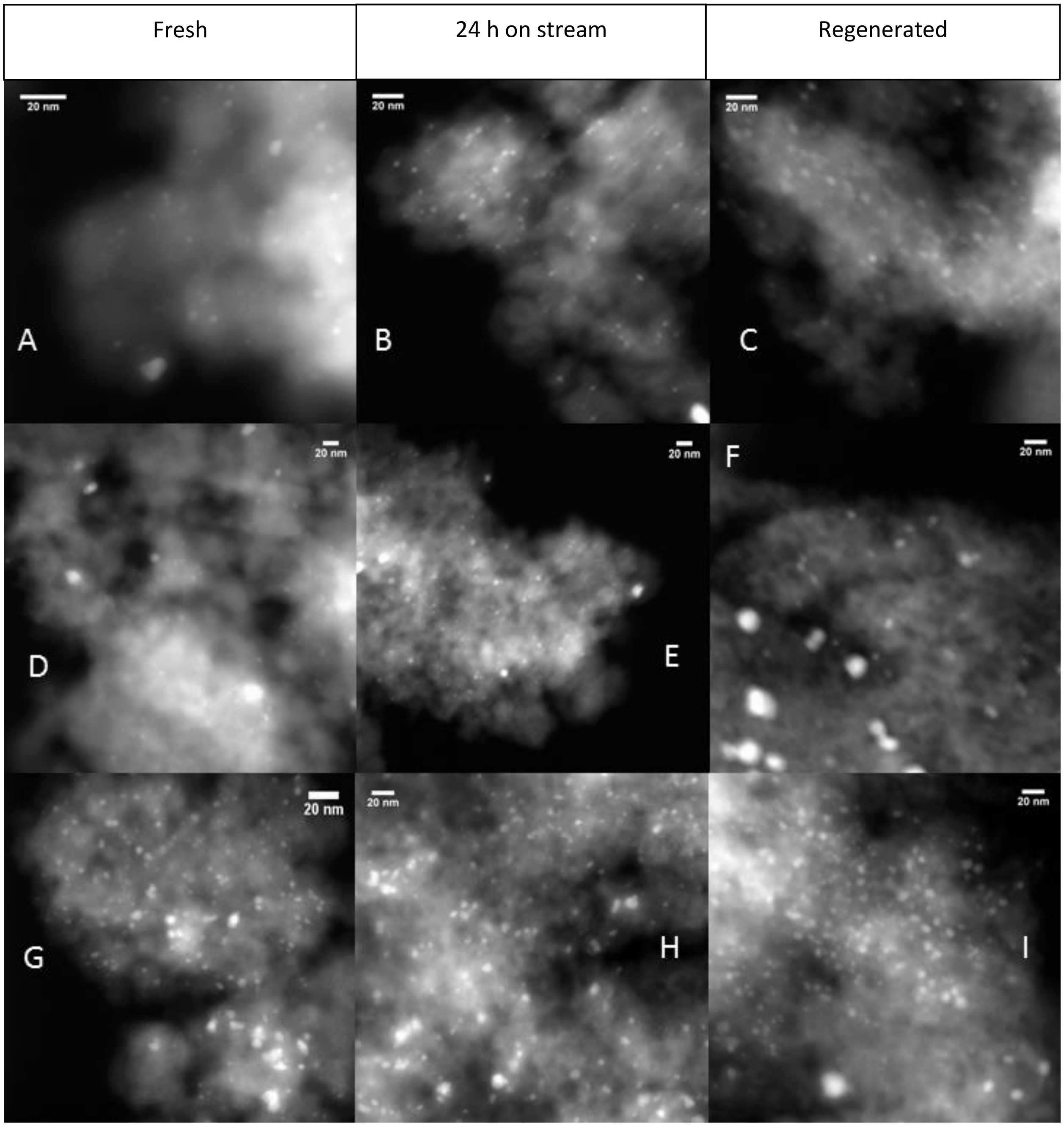

Fresh

24 h on stream

Regenerated

Figure B4: STEM images of fresh, used, and regenerated of A-C) $1Pt/SiO_2$, D-F) $1Pt0.6Sn/SiO_2$ and G-I) $1Pt2.4Sn/SiO_2$.

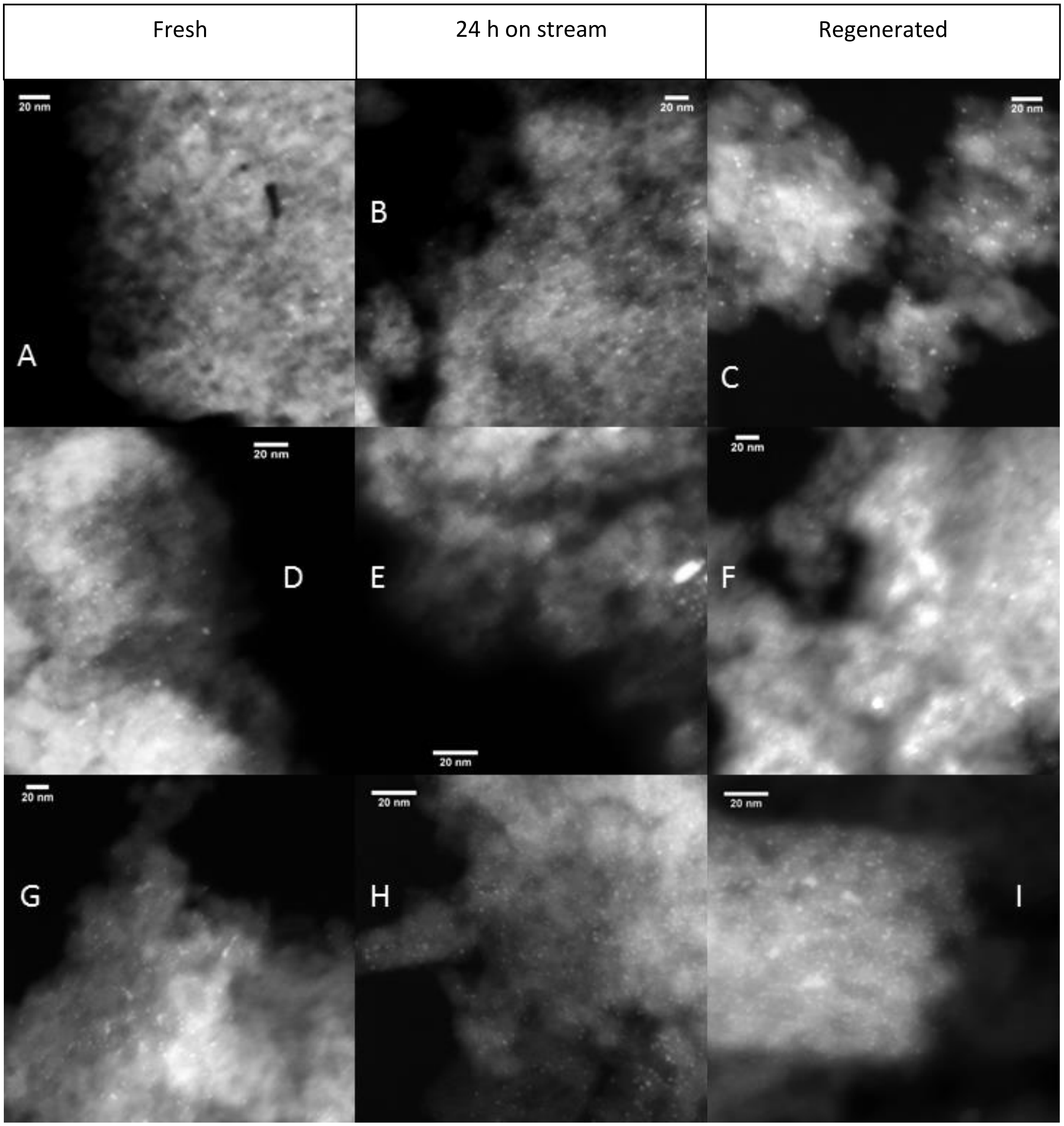

Figure B5: STEM images of fresh, used, and regenerated A-C) $1Pt/Al_2O_3$, D-F) $1Pt0.6Sn/Al_2O_3$ and G-I) $1Pt2.4Sn/Al_2O_3$.

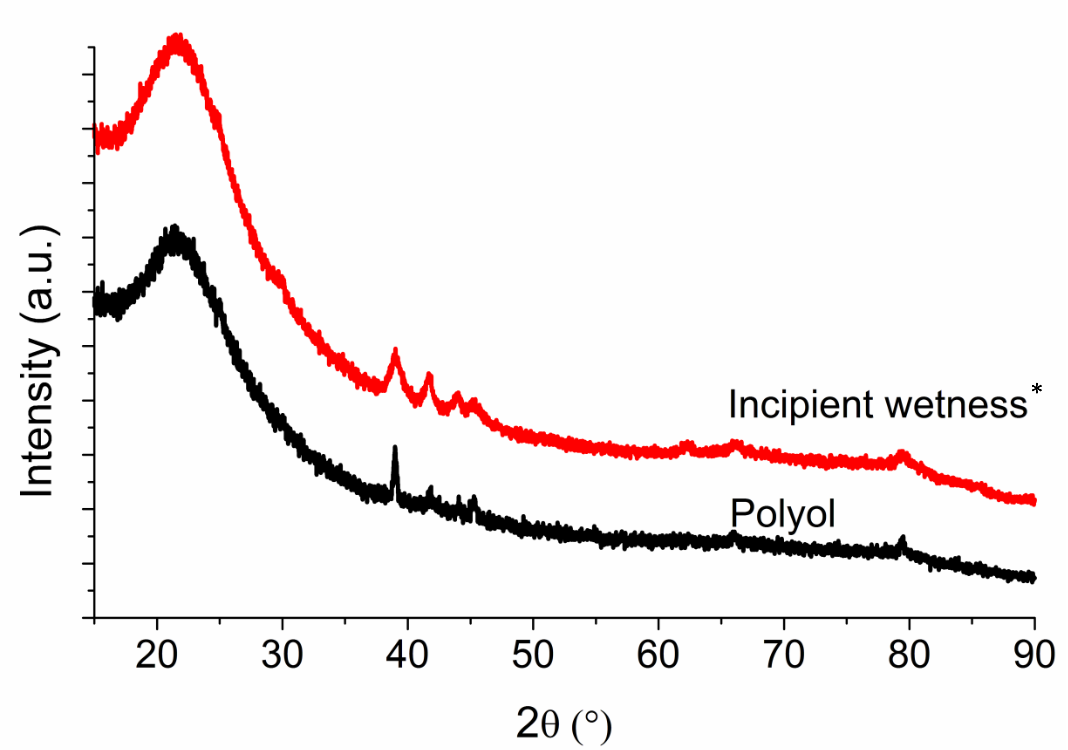

Figure B6: XRD pattern of 1Pt0.6Sn/SiO$_2$-P compared to that of the IWI-synthesized 1Pt0.6Sn/SiO$_2$ sample. Patterns are offset for clarity.

*Pattern was reduced by a factor of two.

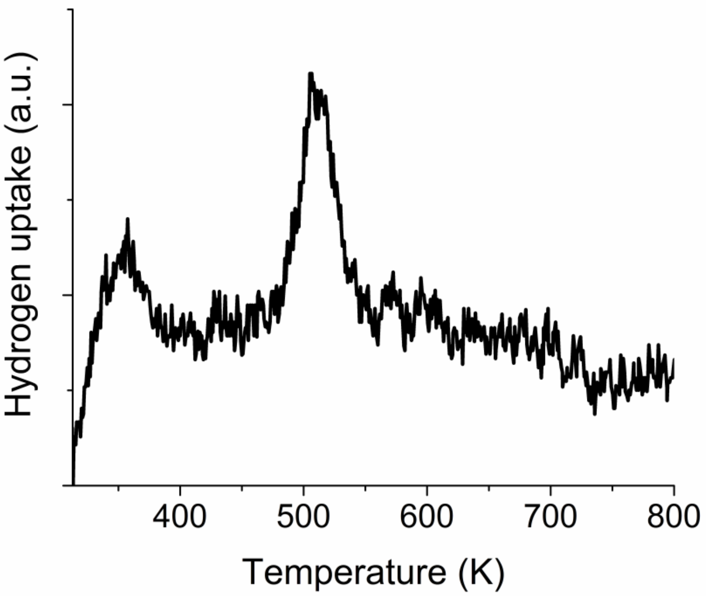

Figure B7: Temperature-programmed reduction of 1Pt0.6Sn/Al$_2$O$_3$-P with a 5 K min $^{-1}$ ramp rate.

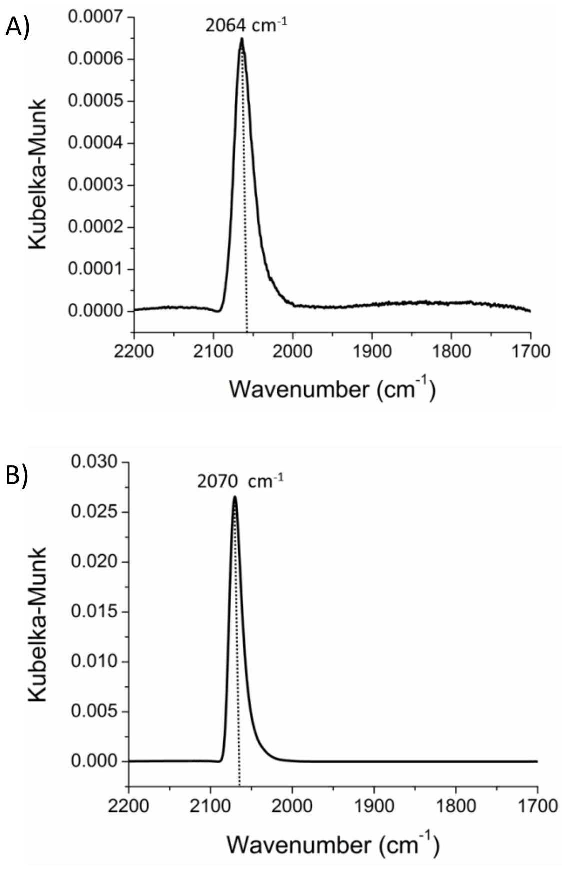

Figure B8: DRIFTS of adsorbed CO on A) 1Pt0.6Sn/SiO_2-P and B) 1Pt0.6Sn/Al_2O_3-P.

Weisz-Prater calculation:

Sample Weisz-Prater (ϕ_I) calculations for internal mass transfer limitations per gram of catalyst associated with $1Pt/SiO_2$ in the presence of H_2 are below. The rate of reaction was the highest over this sample and will represent the worst case scenario for the ϕ_I calculation.

Equation 1 defines the Weisz-Prater criterion for internal mass transfer limitations of the first order reaction of propane over $1Pt/SiO_2$ depicted in Figure 3.12:

$$\varphi_I = \frac{r_{obs} R_p^2 \rho_p}{D_E C_s} < 1 \qquad \text{Eq. 1}$$

where r_{obs} is the observed rate, R_p is the radius of the support particle, ρ_p is the density of the support particle, D_E is the effective diffusivity of propane, and C_s is the propane concentration at the catalyst surface.

r_{obs}= $1.78\text{x}10^{-1}$ mol h^{-1} g_{cat}^{-1}

The following parameters were used in the calculation.

Largest R_p= 0.025 cm

Smallest R_p= 0.0125 cm

ρ_p=0.83 g cm^{-3}

The surface concentration of propane was calculated from the ideal gas law:

C_s= n V^{-1} = P R^{-1} T^{-1}

C_s= $3.94\text{x}10^{-3}$ mol L^{-1}

The effective diffusivity, D_E, is derived from the molecular diffusivity of propane in N_2 (D_{AB}) (ignoring the small fraction of H_2 in the feed) and the Knudsen diffusivity (D_k) in the catalysts shown in equation 2:

$$D_E = \frac{\varepsilon}{\tau}\left(\frac{1}{D_{AB}} + \frac{1}{D_k}\right)^{-1} \qquad \text{Eq. 2}$$

where ε is the porosity and τ is the tortuosity of the silica. The values for ε and τ are assumed to be 0.5 and 3, respectively, according the Davis and Davis.[1]

An empirical relation from Cussler (5.1-9) was used to calculate the value for D_{AB} and is shown in equation 3:[2]

$$D_{AB} = \frac{10^{-3} T^{1.75}\left(\frac{1}{M_{propane}} + \frac{1}{M_{N_2}}\right)^{\frac{1}{2}}}{p\left[(\sum_i V_{i1})^{\frac{1}{3}} + (\sum_i V_{i2})^{\frac{1}{3}}\right]^2} \qquad \text{Eq. 3}$$

where T is the temperature in Kelvins, M is the molecular weight of a designated species, p is the system pressure in atmospheres, and V_{ij} is the atomic and structure diffusion volume increments provided in Cussler.[2]

Substituting the appropriate values, the diffusivity of propane in nitrogen at our reaction conditions is:

D_{AB}= 0.788 cm^2 s^{-1}

The Knudsen diffusivity is calculated from equation 4:[1]

$$D_k = 4850 D_p \left(\frac{T}{M_{propane}}\right)^{\frac{1}{2}} \qquad \text{Eq. 4}$$

where D_p is the diameter of the pore in cm ($6x10^{-7}$ cm for Davisil 636). Substituting in the appropriate values yields:

D_k= $1.22x10^{-2}$ cm^2 s^{-1}

Plugging in the values for D_{AB} and D_k into equation 2 gives an effective diffusivity of propane:

D_E= $1.99x10^{-3}$ cm^2 s^{-1}

Plugging in values into equation 1:

$$\varphi_I = \frac{\left(0.178\ \frac{mol}{h * g_{cat}}\right)(.025\ cm)^2\left(0.83\ \frac{g}{cm^3}\right)\left(\frac{1\ h}{3600\ s}\right)}{\left(0.00199\frac{cm^2}{s}\right)\left(0.00394\frac{mol}{L}\right)\frac{1\ L}{1000\ cm^3}}$$

For the largest particles with a radius of 0.025 cm:

ϕ_I=3.25 for the largest catalyst particles of R_p=0.025 cm

For the smallest silica particle size (R_p=0.0125 cm) the parameter can be recalculated:

$$\varphi_I = \frac{\left(0.178\ \frac{mol}{h * g_{cat}}\right)(.0125\ cm)^2\left(0.83\ \frac{g}{cm^3}\right)\left(\frac{1\ h}{3600\ s}\right)}{\left(0.00199\frac{cm^2}{s}\right)\left(0.00394\frac{mol}{L}\right)\frac{1\ L}{1000\ cm^3}}$$

ϕ_I=0.814

These calculations suggest that the most active catalyst (Pt/SiO_2) is operating on the edge of transport limitations for the rate. All of the promoted catalysts have lower specific rates (per gram) and are therefore free of artifacts from transport limitations.

The Weisz-Prater criterion was applied to 1Pt/Al_2O_3.

R_{obs}= 6.46x10^{-2} mol h^{-1} g_{cat}^{-1}

R_p= 0.005 cm

ρ_p= 2 g cm^{-3}

D_p = 6x10^{-7} cm

The effective diffusivity, D_E, will be the same as the Pt/SiO_2.

D_E=1.99x10^{-3} cm^2 s^{-1}

Plugging in values into equation 1:

$$\varphi_I = \frac{\left(0.0646\ \frac{mol}{h * g_{cat}}\right)(.005\ cm)^2\left(2\ \frac{g}{cm^3}\right)\left(\frac{1\ h}{3600\ s}\right)}{\left(0.00199\frac{cm^2}{s}\right)\left(0.00394\frac{mol}{L}\right)\frac{1\ L}{1000\ cm^3}}$$

ϕ_I=0.114

The 1Pt/Al_2O_3 catalyst was free of artifacts from transport limitations.

References

1. M. E. Davis and R. J. Davis, *Fundamentals of Chemical Reaction Engineering*, McGraw-Hill, Boston, 2003.
2. E. L. Cussler, *Diffusion: Mass Transfer in Fluid Systems*, Cambridge University Press, New York, Third., 2012.

Appendix C:
Calculation of propane equilibrium conversion

The equilibrium conversion of propane is derived from the equilibrium constant K_p which is defined in equation 1:

$$K_p = \frac{x(h+x)P}{(1-x)(1+i+h+x)} \tag{1}$$

where x is the equilibrium conversion, i is the initial molar ratio of inert to propane, h is the initial molar ratio of dihydrogen to propane, and P is the system pressure. The equilibrium constant K_p can be related to the Gibb's free energy, the entropy, the enthalpy, and the temperature of the system through equation 2.

$$-RT \ln K_p = \triangle G_r = \triangle H_r - T \triangle S_r$$

(2)

The enthalpy of the reaction, ΔH_r was calculated using equation 3:

$$\triangle H_r = \triangle H^\circ + \int_{298}^{T} C_p dt$$

(3)

where the reference state ΔH° was taken from Yaws Handbook of Thermodynamic and Physical Properties of Chemical Compounds[1] and the equation for C_p was derived from heat capacity data provided by National Institute of Science and Technology (NIST). The entropy of the reaction was calculated using equation 4:

$$\triangle S_r = \triangle S^\circ + \int_{298}^{T} \frac{C_p}{T} dt \tag{4}$$

where ΔS° was taken from Yaws Handbook[1] and the equation for C_p was derived from heat capacity data provided by NIST. Enthalpy and entropy values for dihydrogen were calculated from equations provided by NIST.

Figure 1 contains an example of the NIST data used to derive the equations for propane and propene C_p.

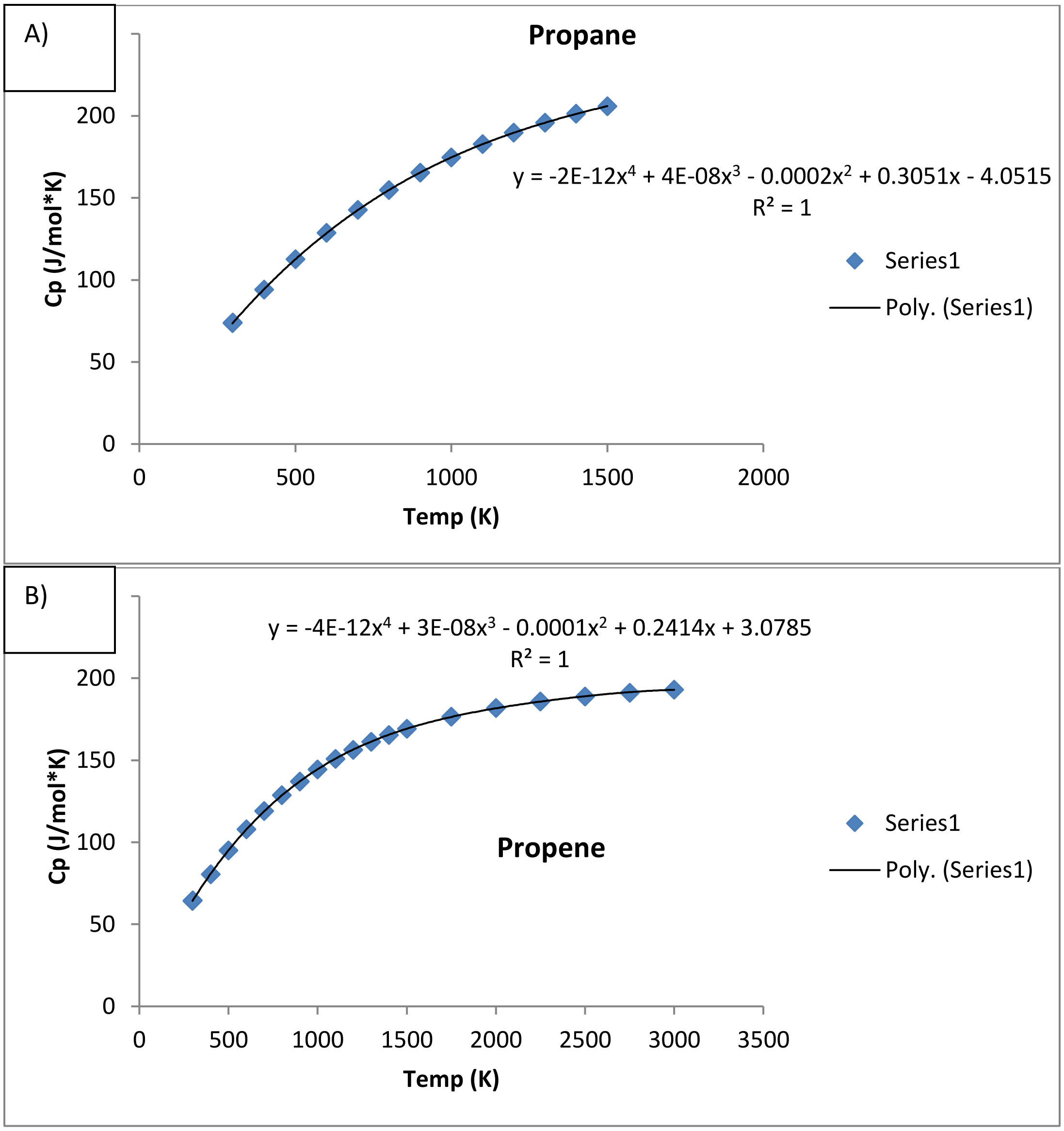

Figure C1: Heat capacity data for A) propane and B) propene. Values used to derive the C_p equations are taken from NIST.

References for Appendix C

1. Yaws, C. L. *Yaws Handbook of Thermodynamic Properties*. (Gulf Publishing Company, 2007).

Appendix D:

Sample chromatogram of propane conversion products over Pt/Al_2O_3 with co-fed H_2

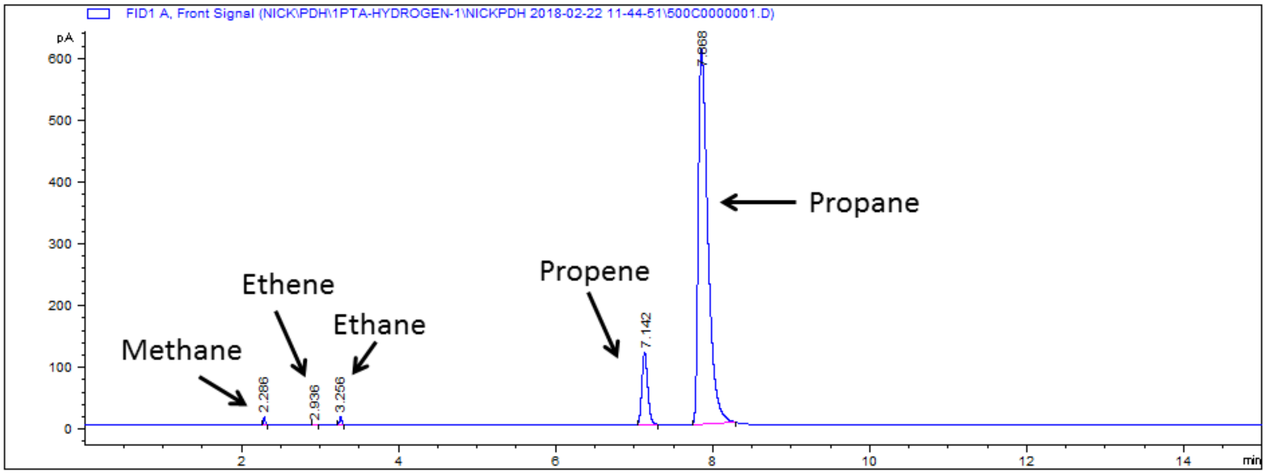

Figure D1: Sample chromatogram utilizing an Agilent 7890A gas chromatograph equipped with an FID detector and an HP-PLOT/Q column.

Appendix E:

Summary of other published works

Xie, J., Duan, P., Kaylor, N., Zheng, Yin, K., Huang, B., Schmidt-Rohr, K., Davis, R.J. Deactivation of Supported Pt Catalysts during Alcohol Oxidation Elucidated by Spectroscopic and Kinetic Analyses. ACS Catal. ***7,*** *6745–6756 (2017).*

The selective oxidation of 1,6-hexanediol with O_2 to product aldehydes and acids occurs readily in water over supported Pt nanoparticles. The initial turnover frequency of 0.54 s^{-1} (at 343 K and 1 MPa O_2) decreases significantly with reaction time because of product competitive adsorption and irreversible adsorption of unknown strongly bonded species. To identify the poisoning species, in situ surface-enhanced Raman spectroscopy (SERS) and solid-state ^{13}C nuclear magnetic resonance (NMR) spectroscopy were applied in this work. In situ SERS during 1,6-hexanediol oxidation revealed an accumulation of di-σ-bonded olefinic species with features at ∼1150 and ∼1460 cm^{-1} on the poisoned Pt surface. Consistent with SERS, ^{13}C NMR spectroscopy of a Pt catalyst deactivated by oxidation of ^{13}C-labeled 1,4-butanediol revealed a $C{=}C$ peak associated with ethylene. Molecules containing olefinic groups are 2 orders of magnitude more effective at competing for Pt surface sites in comparison to the aldehyde and acid products from alcohol oxidation. The poisoning olefinic species were generated by decarbonylation of product aldehyde (as revealed by head space analysis) and could be easily removed from the deactivated catalyst by mild treatment in H_2.

Xie, J., Kammert, J.D., Kaylor, N., Zheng, J.W., Choi, E., Pham, H.N., Sang, X., Stavitski, E., Ettenkofer, K., Unonic, R.R., Datye, A.K., Davis, R.J. Atomically Dispersed Co and Cu on N - Doped Carbon for Reactions Involving C − H Activation. ACS Catal. ***8,*** *3875–3884 (2018).*

Atomically dispersed Co(II) cations coordinated to nitrogen in a carbon matrix (Co-N-C) catalyze oxidative dehydrogenation of benzyl alcohol in water with a specific activity approaching that of supported Pt nanoparticles. Whereas Cu(II) cations in N-doped carbon also catalyze the reaction, they are about an order of magnitude less active compared with Co(II) cations. Results from X-ray absorption spectroscopy suggest that oxygen is also bound to N-coordinated Co(II) sites but that it can be partially removed by H_2 treatments at 523–750 K. The N-coordinated Co(II) sites remained cationic in H_2 up to 750 K, and these stable sites were demonstrated to be active for propane dehydrogenation. In situ characterization of Cu(II) in N-doped carbon revealed that reduction of the metal in H_2 started at about 473 K, indicating a much lower thermal stability of Cu(II) in H_2relative to Co(II). The demonstrated high catalytic activity and thermal stability of Co-N-C in reducing environments suggests that this material may have broad utility in a variety of catalytic transformations.